Università degli Studi Roma Tre

Dipartimento di Matematica e Fisica
Doctoral program in Physics – XXXIV cycle

A thesis presented for the degree of
Doctor of Philosophy in Physics

Testing Gravity with Laser Ranging: LARES-2 and MPAc space missions

Author:

Laura Rubino

Supervisors:

Dr. **Simone Dell'Agnello**

Prof. **Wolfango Plastino**

Doctoral Program Coordinator:

Prof. **Giuseppe Degrassi**

A.A. 2021/2022

Contents

List of Acronyms

AM0 Air Mass Zero

APOLLO Apache Point Observatory Lunar Laser-ranging Operation

BB BreadBoard

CCD Charge-Coupled Device

CCR Cube Corner Retroreflector

cFP compact Field Point

CLPS Commercial Lunar Payload Services

COTS Commercial Off-The-Shelf

DAO Dihedral Angle Offset

EM Engineering Model

EP Equivalence Principle

ESA European Space Agency

FFDP Far Field Diffraction Pattern

FM Flight Model

GLONASS Global Navigation Satellite Systems

GNSS Global Navigation Satellite Systems

GPS Global Positioning System

GR General Relativity

GRAIL Gravity Recovery and Interior Laboratory

HDRM Hold Down Release Mechanism

ILRS International Laser Ranging Service

IM Intuitive Machines

INFN National Institute of Nuclear Physics

InSight Interior Exploration using Seismic Investigations, Geodesy and Heat Transport

I/O Input/Output

IR InfraRed

ISL Inverse Square Law

ITRF International Terrestrial Reference Frame

LAGEOS LAser GEOdynamics Satellite

LaRA Laser Retroreflector Array

LARES Laser Relativity Satellite

LaRRI Laser Retroreflector for InSight

LLR Lunar Laser Ranging

LN2 Liquid Nitrogen

L-T Lense-Thirring

NASA National Aeronautics and Space Administration

ML100 MoonLIGHT 100

MLI Multi-Layer Insulation

MLRO Matera Laser Ranging Observatory

MLRS McDonald Laser Ranging Station

MoonLIGHT Moon Laser Instrumentation for General relativity High accuracy Test

MPAc MoonLIGHT Pointing Actuators

MRR Manufacturing Readiness Review

NI National Instruments

OCA Observatoire de la Cote d'Azur

OCS Optical Cross Section

OoT Out of Tolerance

PEP Planetary Ephemeris Program

PFM Proto Flight Model

PID Proportional-Integral-Derivative

PPN Parametrized Post-Newtonian

PV Peak to Valley

RMS Root Mean Square

SCF Satellite/Lunar/GNSS laser ranging altimetry Characterization Facilities

SEP Strong Equivalence Principle

SLR Satellite Laser Ranging

SS Solar Simulator

TID Total Ionizing Dose

TIR Total Internal Reflection

ToF Time of Flight

TVT Thermal vacuum test

UDP User Datagram Protocol

UHV Ultra High Vacuum

VA Velocity Aberration

WEP Weak Equivalence Principle

WFI Wavefront Fizeau Interferometer

List of Figures

List of Tables

Abstract

Laser Ranging is a technique used to perform accurate precision distance measurements between a laser ground station and an optical target, a Cube Corner Retroreflector (CCR). Since 1969 it is possible to realize Lunar Laser Ranging (LLR) measurements thanks to Apollo and Luna missions that placed some arrays of CCRs on the lunar surface. Moreover, the launch of several satellites covered by small CCRs started a new technique, known as Satellite Laser Ranging (SLR).

Laser Ranging technique is fundamental to investigate different scientific aspects, as test of General Relativity (GR), geodesy, study of the Earth-Moon system and lunar geophysics. In particular, thanks to the measurements of LLR, some GR predictions have been tested, such as: the Weak and Strong Equivalence Principle (EP), the Parametrized Post-Newtonian parameters (γ and β), the constancy of the gravitational constant G, the geodetic precession and the Yukawa contribution to the gravitational potential. On the other hand, the SLR data are fundamental for the frame-dragging measurements.

To improve Laser Ranging measurements, it is necessary to build new payloads, like Laser Relativity Satellite (LARES)-2 and MoonLIGHT Pointing Actuators (MPAc). In particular, the SLR needs new targets to improve measurements: LARES-2 was designed to reduce the uncertainties and to make an accurate measurement of frame-dragging, or also known as Lense-Thirring (L-T) effect. LARES-2 is a new satellite, ready to be launched in spring 2022. While the manufacturing of the satellite has been performed in the INFN of Padova, the optical analysis of each CCR and the integration of them have been performed in the SCF_Lab, at INFN of Frascati. The particularity of this new satellite is the use of CCR Commercial Off-The-Shelf (COTS).

The analysis of 640 CCRs is divided into different steps: incoming inspection, Far Field Diffraction Pattern (FFDP) and interferograms analysis, the results of which confirm the expected lower optical quality of the hardware, SCF-Test on BreadBoard, during which the average intensity of the CCRs at the LARES-2 Velocity Aberration (VA) remains constant in all conditions as expected and the relaxation constant is about $30 minutes$, indicating the quick response of CCRs to the changes of the thermal conditions.

Despite laser ground stations have significantly improved during the years, the current limitation of the lunar optical target is due to lunar librations. In order to achieve more precise LLR measurements, Moon Laser Instrumentation for General relativity High accuracy Test (MoonLIGHT) project is designed by SCF_Lab in collaboration with the University of Maryland: the idea is to create a next-generation of retroreflectors.

The field of view of each CCR is limited: the retroreflector needs to be pointed precisely to the ground station. The Apollo CCR arrays were manually arranged by the astronauts; in 2018 INFN proposed to European Space Agency (ESA) the MoonLIGHT Pointing Actuators (MPAc) project, able to perform unmanned pointing operation of MoonLIGHT. In 2019 ESA chose MPAc among 135 eligible scientific project proposals. In 2021 ESA agreed with National Aeronautics and Space Administration (NASA) to launch MPAc to the Reiner Gamma region of the Moon; the lander on which MPAc will be integrated is designed by Intuitive Machines (IM). The launch expected date is in April 2024.

The work described about this project is the development of the design of the MPAc. In order to test the efficiency of the motors, gears and structure, three prototypes are built and each one of these has different features. The first one is in plastic, included gears, with a gear ratio of 4:1. The second prototype is in plastic, but with metallic gears, with a gear ratio of 50:1. The third one is entirely made of aluminum. At the same time, to test electronics and software, a commercial board and an Electronic BreadBoard are used.

Why this work and what my contribution was

The aim of this thesis is to describe test of General Relativity related to LLR and SLR experiments and to give a detailed description of the two projects on which I worked, and in particular the mechanical and optical analysis of the new satellite LARES-2 and the first phases of the design of the new lunar retroreflector MPAc.

My PhD thesis activities can be divided into two parts, of which the second (MPAc) is the most important one:

- LARES-2: I participated in laboratory activities for incoming inspection, optical analysis and mechanical measurements of 640 CCRs and integration of them onto the new satellite. Moreover I worked on the SCF-Test of the BreadBoard to test optical response of four CCRs under simulated space conditions.

- MPAc: the first phase of this project starts at the end of the first year of my PhD, when ESA selected MPAc. After the selection, the main work consisted on the design of the entire structure, able to perform two continuous rotations in Azimuth and Elevation. At the same time, it was also necessary to design an electronics board through which to control the two motors. I worked on three prototypes, two of which made of plastic and one made of aluminum. The purpose of these was to test electronics, mechanics and software. But most of all, during most of my thesis time, I gave an original contribution to the overall conception, to the full integrated opto-electro-mechanical design and to the operating software, which is essential for the control of the electronics of the flight payload, through a commercial space qualified electronics board. I worked on the frontline of the definition, choice and finalization of all these mission-critical components and functionalities, both for software and hardware (cables and connectors included, which in the harsh lunar enviroment are not trivial technical issues). This is a full-blown space flight apparatus designed and realized entirely at INFN-Frascati, composed of active electronic and mechanical positioning subsystems supporting our flagship fundamental physics instrument, the passive laser retroreflector MoonLIGHT.

CHAPTER 1

Laser Ranging

Lunar Laser Ranging (LLR) and Satellite Laser Ranging (SLR) use short-pulse lasers to measure the two-way time of flight (and hence distance) from ground stations to a particular optical target, reflecting laser pulses back to the ground stations (called retroreflectors, see Section 1.2), placed on the Moon and on Earth orbiting satellites. Scientific products derived using LLR and SLR data include precise geocentric positions and motions of ground stations, satellite orbits, components of Earth's gravity field and their temporal variations, precise lunar ephemerides and information about the internal structure of the Moon. Thus, satellite and lunar laser ranging data and their derived data products are very useful for research in various fields such as:

- **Test of fundamental physics**: The lunar orbit offers a pristine laboratory for testing gravity. All types of tests on general relativity will be analyzed with more details in Chapter 2.

- **Dynamic of the Earth-Moon system**: LLR data allows to analyze in details the three-dimensional rotation of the Moon (physical librations). The latter can be classified as forced librations, with period and amplitude known, and free librations, with period computable but amplitude not known a priori [61].

- **Geodesy**: LLR contributes to the determination of Earth orbital parameters, as well as precession (including relativistic geodetic precession), nutation, polar motion, and long-term variation of these effects [48].

- **Planetary and lunar ephemerides**: LLR has allowed to build a high-precision geocentric ephemeris of the Moon. Continued LLR data are fundamental to the maintenance of planetary and lunar ephemerides; they can be used for navigation and orbit determination in future lunar missions [50].

- **Lunar geophysics**: the success of the Gravity Recovery and Interior Laboratory (GRAIL) mission provides new features not previously resolved, including new craters, volcanic land-forms, tectonic structures, basin rings [66]. Combining data from GRAIL and LLR it has been possible to obtain new estimates of the lunar interior properties, among them, the three principal moments of inertia and evidences for a distinct lunar core. In particular, LLR analyses indicate that the core is fluid [63]. Important contributions from LLR also include the measurements of the lunar rotational dissipation, due to the solid-body tides raised by Earth (and Sun) and a distinct rotation by the fluid core [62], and tidal dissipation [34].

1.1 Basic Principles

Laser ranging technique is based on the measurement of the Time of Flight (ToF) of the laser pulses. The two-way ToF is measured on the ground station using highly accurate timing systems. In order to measure the optical target to station distance d, the basic equation is [42]:

$$d = c\frac{\tau}{2} \tag{1.1}$$

where c is the speed of light in vacuum and τ is the time of flight of the laser pulse. It is necessary to divide by two since the round-trip of the laser.

Laser ranging can be performed to Earth-orbiting targets (Satellite Laser Ranging) or to targets on the lunar surface (Lunar Laser Ranging).

The mean distance between Earth and Moon centers is 385000.6 km, corresponding to 2.56 s of round-trip light travel time. The Earth-Moon distance ranges between 356500 km and 406700 km, chiefly due to the elliptical lunar orbit ($e = 0.055$) and solar perturbations. The distance range

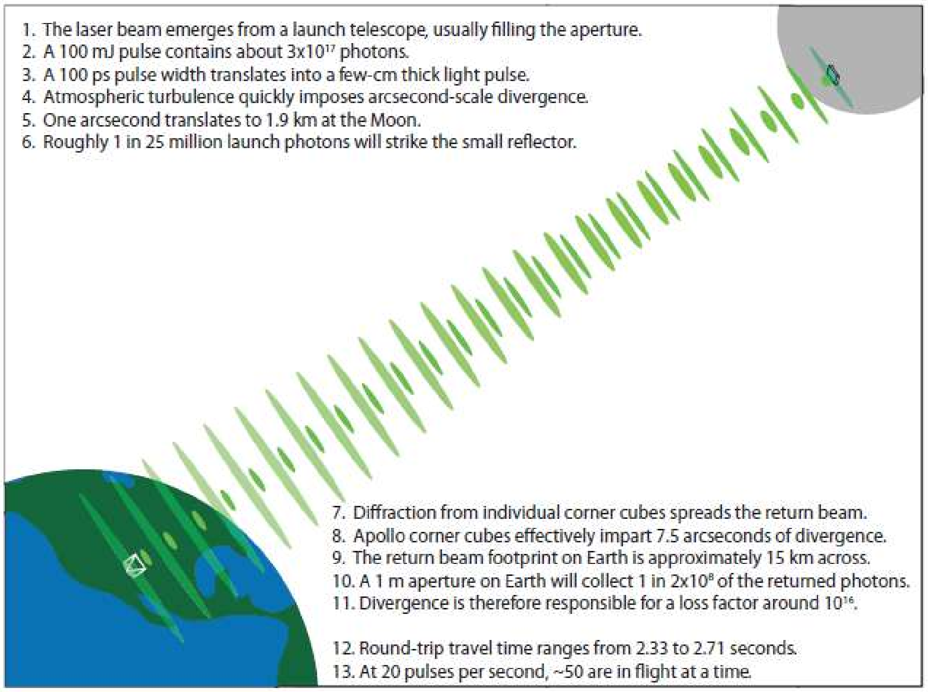

Figure 1.1: LLR scheme [43]: the laser beam increases its size due to the atmospheric turbulence; diffraction from optical targets spreads the return beam.

translates into a range of the travel time photons: from 2.34 s to 2.71 s [43]. The performances of the observations depend on the quality of the time measurements. In order to have a precision of 1 cm, it is necessary to have an accuracy of the order of $10^{-10}s$ in the measurement of the light travel duration. Thus, a very sophisticated timing system is used. Nevertheless, there are several factors that affect the accuracy of the measurements, as the atmosphere. The latter produces a time delay, estimated as $5 \cdot 10^{-11}s$ and $10 \cdot 10^{-11}s$ based on the temperature, pressure and humidity. Moreover, the libration of the Moon produces a scatter of about $2 \cdot 10^{-10}s$ in time of flight and of a few centimeters in distance [16].

Atmosphere turbulence causes also a spread of the laser pulses of $1arcsec$, translating in a circular area of $1.9km$ of diameter on the lunar surface (Figure 1.1). This effect has to be taken into account to sufficiently illuminate the lunar optical targets and, thus, to get a detectable laser return to the ground stations.

The travel of return photons is more difficult, because of the diffractive spread of the retroreflector on the lunar surface in addition to the velocity aberration. Practically, considering a $1m$ circular area on Earth, the ground station can receive one photon out of every $250 \cdot 10^6$ reflected from the Apollo array. But, the relative motion of the Earth with respect to the Moon produces a further reduction of the reflector signal by a factor of $0.6 - 0.8$ [43].

1.2 Cube Corner retroreflectors

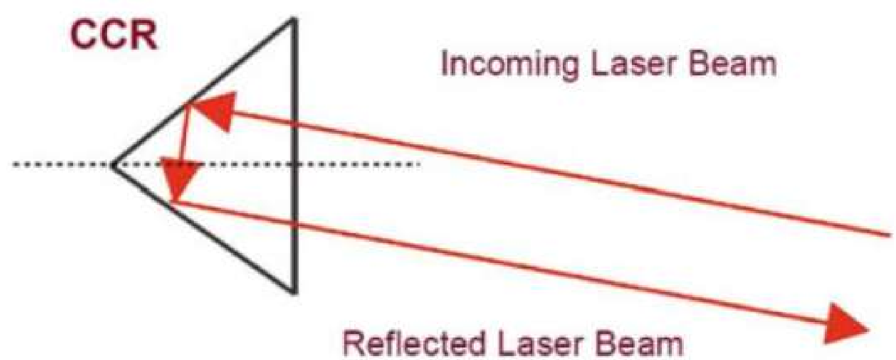

Figure 1.2: CCR concept [19]: the beam of light reflects exactly in the same direction of incidence.

The optical target, previously named generically retroreflectors, used in Laser Ranging technique is called Cube Corner Retroreflector (CCR). The particularity of a CCR is the property to reflect back a beam of light, incident on its front surface, exactly in the same direction of incidence. The CCR shape consists of three mutually perpendicular, intersecting flat surfaces. A ray of light reaching the reflector, undergoes three reflections on the three surfaces and it is reflected back in the same direction it came from. A fundamental feature of CCRs is Dihedral Angle Offset (DAO), defined as a deviation of the angle between the reflecting faces.

The principle of CCR is reported in 2D in the Figure 1.2. In the 3D view, there will be a third reflection on the back face of the CCR.

There are two main class of CCRs (Figure 1.3): solid and hollow. Solid CCRs are prisms made of fused silica; this material has unique optical, mechanical and thermal properties. Moreover the fused silica, like the old

Suprasil T19 (now called Suprasil 1) and the modern Suprasil 311, has high radiation resistance, indispensable for the space environmental [28]. Hollow cubes have only the reflecting faces, made by support stuff covered with a high reflectivity metal layer.

Figure 1.3: CCR types: uncoated CCR (left), coated CCR (center), hollow CCR (right).

Furthermore, solid cubes can be divided into two categories: the back faces of the CCR can be coated or uncoated. Uncoated CCRs are just the solid prism of fused silica, while coated CCRs are back-coated with aluminum prisms, whose reflective faces have a high reflective coating.

Retroreflection obtained by uncoated CCR is a total internal reflection. Total Internal Reflection (TIR) derives from Snell's law of refraction (Figure 1.4). A ray travels across an object with high density to one with lower density; in our case, the medium with high density is fused silica prism and the one with lower density is either the air or the vacuum of the space. When the angle between the incident ray and the normal vector of the interface between the two media increases, the intensity of the refracted ray decreases, The angle reaches a critical value beyond which the ray is totally reflected at the interface. In this particular situation, the interface between the two media will act as a perfect reflector; the particular geometry of the CCR allows that the ray hits three times the faces of the cube an then comes back.

Coated and hollow CCRs act as normal retroreflectors: the light ray on the reflecting faces works with a classical reflection.

One difference between the uncoated and coated CCRs derives from the acceptance angle for the laser beam reflection: in fact, for the uncoated this angle is much less than the coated, because of the TIR. The method of total

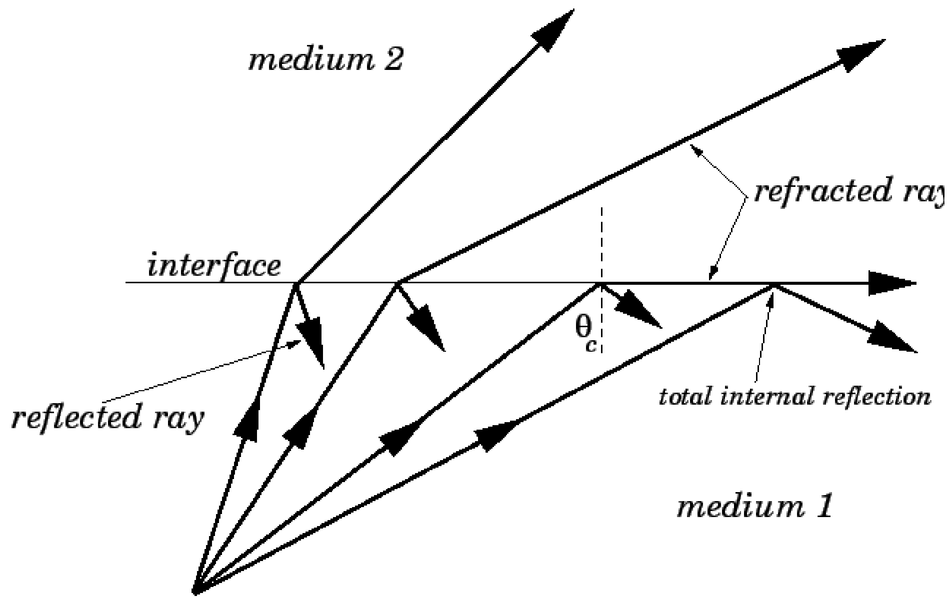

Figure 1.4: Snell's law for total internal reflection.

internal reflection limits the acceptance angle [41].

Another difference between coated and uncoated CCRs comes from qualitative and quantitative characteristics of their Far Field Diffraction Pattern (FFDP): in fact coated CCRs do not change the polarization of the laser beam [5] after the reflection; while in the uncoated ones the polarization changes at every reflection [28].

Further difference consists in the thermal degradation. The CCRs are always subjected to strong thermal gradients that can change the intensity of the light return in the transition from sunlight exposition to shadow. Coated CCR showed a light return degradation of about 87% while uncoated CCR showed a degradation of about 20% [11].

While the hollow CCRs do not have a space heritage, the coated ones have been used for low-altitude satellites, like Global Navigation Satellite Systems (GLONASS), Global Positioning System (GPS), Global Navigation Satellite Systems (GNSS) [28], or for martian retroreflectors, like Laser Retroreflector for InSight (LaRRI) on board of the Interior Exploration using Seismic Investigations, Geodesy and Heat Transport (InSight) lander, landed on Mars in November 2018 [51] and Laser Retroreflector Array (LaRA) on board of Perseverance rover, landed on Mars in February 2021. Uncoated

CCRs have been used on satellites like LAGEOS [7] and LARES [20] (section 1.5), and on the lunar arrays (section 1.3).

The reasons that led to these choices are related to a compromise between the optical degradation and the acceptance angle. Indeed, the low-altitude satellites need a larger acceptance angle in order to have more SLR data, at the expense of better optical performance. The martian retroreflectors also need a larger acceptance angle, because the future orbiter, equipped with a laser, will orbit at a not too great distance. Regarding the lunar array, the reason of the uncoated CCRs is related to the deformation of the CCR as a consequence of the coating heating [19].

1.3 Lunar Arrays

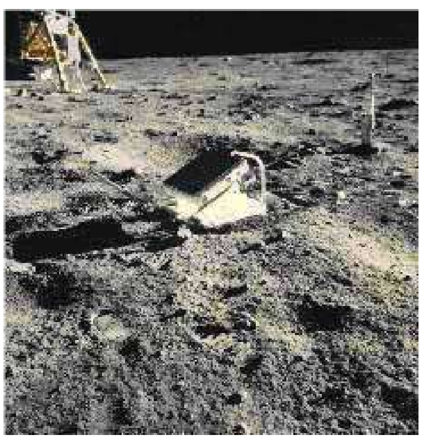

(a) Apollo11

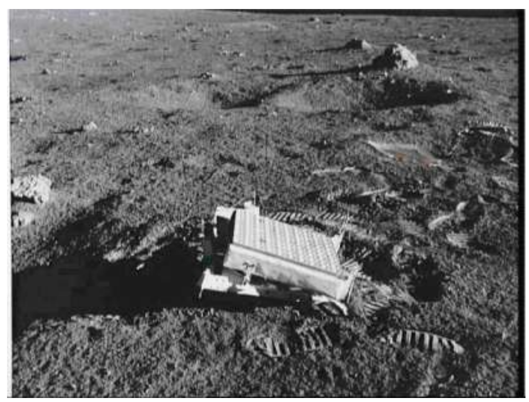

(b) Apollo14

Figure 1.5: The CCR array of the Apollo mission: 100 CCRs in a 46 cm^2 aluminum panel [59].

The initiation of the LLR was in 1969, thanks to the Apollo 11 astronauts who landed on the Moon in July and deployed a CCR array. Shortly thereafter, several ground stations, ranged to the array. In November, 1970, the Russians landed the Lunokhod 1 robotic rover on the Moon, through the Luna 17 mission, equipped by a French-built CCR array. The Lunokhod 1 array was followed by the Apollo 14 and Apollo 15 arrays, and Lunokhod 2 reflectors, (through the Luna 21 mission), arriving in that order [47].

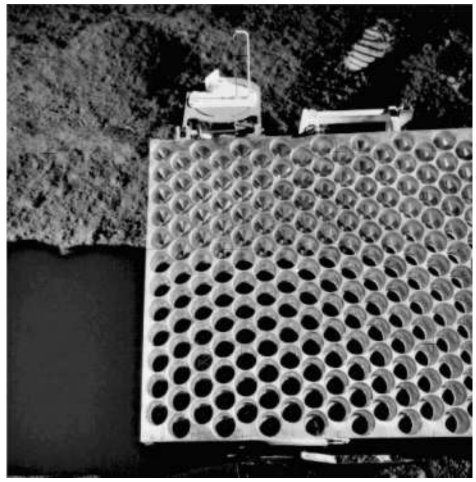

Figure 1.6: The CCR array of the Apollo 15 mission: 300 CCRs in a hexagonal arrangement [59].

The design of the currently used CCR arrays are summarized here:

- *Apollo 11 and Apollo 14*: composed of 100 fused silica CCRs, mounted in a $46cm^2$ aluminum panel (Figure 1.5). Each CCR is circular and $3.8cm$ in diameter, arranged in 10 columns and 10 rows [59].

- *Apollo 15*: composed of 300 CCRs, mounted in two panels, in a hexagonal arrangement. The first panel has 204 retroreflectors; the second 96 [59]. The total array dimension are $1.05m$ x $0.64m$ (Figure 1.6). Each CCR is similar to those of Apollo 11 and Apollo 14, with a diameter of $3.8cm$.

- *Lunokhod 1 and Lunokhod 2*: equipped by CCR array composed of 14 glass CCR (Figure 1.7), each having an edge of $11cm$ and a silvered coating [43].

Figure 1.8 shows all CCR arrays currently located on the Moon.

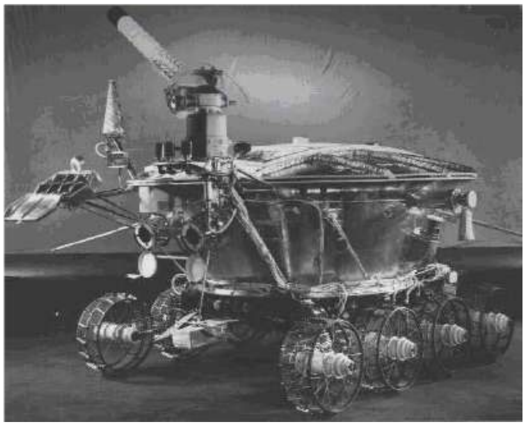

(a) Lunokhod rover

(b) Lunokhod retroreflectors

Figure 1.7: The russian rover Lunokhod 1, and a zoom of the retroreflectors mounted on the rover [59].

1.4 Ground stations for LLR

The LLR stations are constrained by weather conditions and Moon's visibility. The first accurate LLR observations were performed on the 3.0 m telescope at Lick Observatory (California). However, the operation at Lick Observatory was designed only for demonstration of preliminary data acquisition.

Despite several observatories ranged successfully the Moon, most of the scientific results derived by long observing campaigns.

The first relevant observation came from the McDonald Observatory (Texas), which used a ruby laser with a 4 ns pulse, firing at a repetition rate of about 0.3 Hz [44]. McDonald laser operations maintained routine activities for more than 15 years. The data can be divided into three spans, based on their accuracy [29] (Figure 1.9).

The accuracy of the early 1970 data is at 25-cm levels. Improvements in the time system reduced the accuracy at the level of 15-cm in the mid 1970s. Then, in the mid 80s, the McDonald Observatory was replaced by the McDonald Laser Ranging Station (MLRS), able to range even the artificial satellites. With new, improved timing system, better computing and laser technology, in spite of the reduced aperture size (0.76 m), it produced lunar data and also satellite data with an improved accuracy (2-cm to 3-cm level).

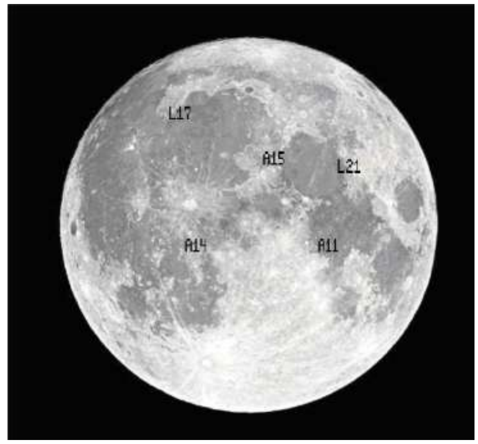

Figure 1.8: The CCR array sites on the Moon [59].

Despite the accuracy, the early data still plays an important role in separating effects with long characteristic timescales, notably precession, nutation, relativistic geodetic precession and so on.

From 1978 to 1980 a set of observations came from Orroral Observatory in Australia [65].

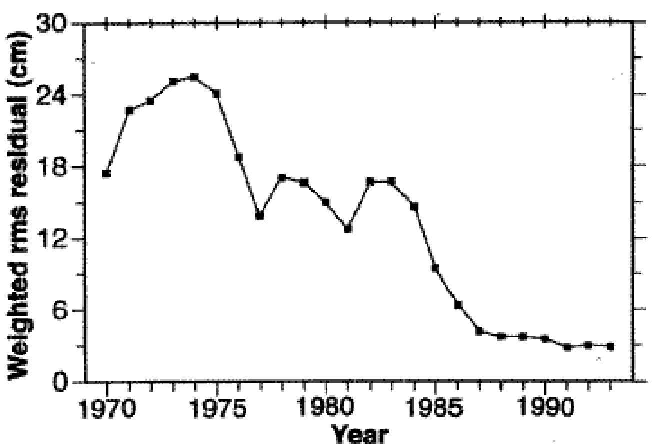

Figure 1.9: Histogram of the weighted root-mean-square (rms) post-fit residual (observed minus model) as a function of time [29].

Another station is at the Observatoire de la Cote d'Azur (OCA) in Grasse, France which began accurate observations in 1984, with a 1.5 m telescope, a

70 ps Nd:YAG (neodymium-doped yttrium aluminum garnet) laser firing at 10 Hz [44]. Its precision changed from the 15-cm level at the beginning to the centimeter level in 1987 [53]. Continuous observations were made from 1984 to 2005. Then, the OCA demonstrated the advantage of LLR operations at a near-infrared wavelength [25].

Modern station for the LLR measurements is the Wettzell Observatory, in Germany, with high accuracy also obtained at the near-infrared wavelength. Moreover, new contributions for LLR observations of centimeter-level accuracies came from the upgraded system of Matera Laser Ranging Observatory (MLRO), in Italy [60].

Since 2007, the Apache Point Observatory Lunar Laser-ranging Operation (APOLLO) in New Mexico has obtained high-quality LLR observations. In particular, APOLLO employs a laser at 532 nm, generating 100 ps pulses at a 20 Hz repetition rate [44]. The major limitation of the past LLR measurements derived from the poor detection rates. APOLLO instead has overcome this limitation thanks to a large collecting area of 3.5 m diameter telescope. In this way, and together also with the increase in data analysis technique and statistics collected, data can reach high-quality at the millimeter level (Figure 1.10) [40].

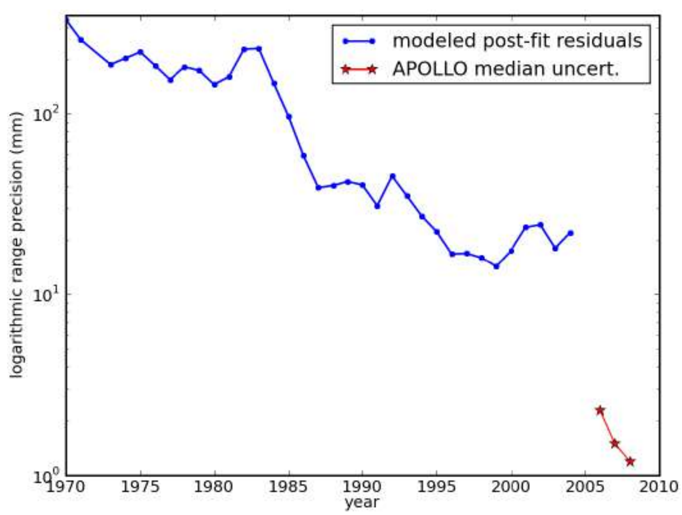

Figure 1.10: Improvements in the ground station technology over the past 40 years have increased the range precision by 2 orders of magnitude [40].

1.5 Satellites

Several satellites are equipped with CCRs to return the incoming laser pulse back to the transmitting site. SLR gives the most precise positioning in space respect to the International Terrestrial Reference Frame (ITRF): a Cartesian coordinate system co-rotating in space with the Earth, with origin on its center of mass. ITRF is fundamental to understand and reference the constantly motion of Earth's crust and SLR is the best space geodetic technique to measure the geocenter, i.e. the origin of ITRF. The long-term aim is to determine and maintain an updated reference frame, with a high accuracy.

The satellites below described are passive satellites with no power, communications, or moving parts. Their operations consist of simply the generation of the orbit predictions necessary for the stations to acquire and track the satellite.

Figure 1.11: LAGEOS-I Satellite.

- The LAser GEOdynamics Satellite (LAGEOS) was designed by NASA and launched on May 4, 1976. It was the first spacecraft dedicated exclusively to high-precision laser ranging and provided the first opportunity to acquire laser-ranging data that were not degraded by errors originating in the satellite orbit or satellite array. It is a spherical satellite, with a diameter of 60 cm, covered with 426 CCRs, and a mass of 406.965 kg. LAGEOS travels in a stable circular orbit, at an altitude of 5860 km from Earth with an inclination of 52.64° [22] (Fig. 1.11).

- LAGEOS-2, based on the original LAGEOS design, was built by the Italian Space Agency (ASI) and launched on October 22, 1992. It is a spherical satellite, with a diameter of 60 cm, covered with 426 CCRs, and a mass of 405.38 kg. LAGEOS-2 travels in a stable circular orbit, at an altitude of 5620 km from Earth with an inclination of 109.84° [22] (Fig. 1.12(a)).

- Laser Relativity Satellite (LARES) was launched from the Europe's Spaceport in Kourou, French Guyana, on February 13th, 2012, on the occasion of the first flight of the VEGA launcher. It is a spherical satellite, with a diameter of 36.4 cm, covered with 92 CCRs, and a mass of 386.8 kg. LARES travels in a circular orbit, at an altitude of 1450 km from Earth with an inclination of 69.5° [22] (Fig. 1.12(b)).

(a) LAGEOS-II Satellite.

(b) LARES Satellite.

Figure 1.12: LAGEOS-II and LARES satellites.

1.6 Ground stations of ILRS

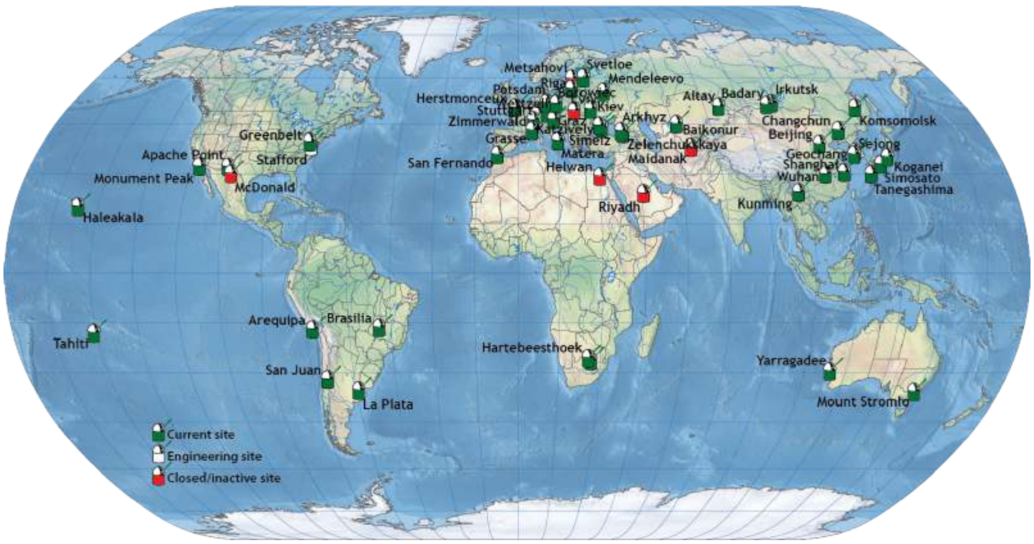

Figure 1.13: Current ILRS configuration.

Laser ranging to a near-Earth satellite was first carried out by NASA in 1964 with the launch of the Beacon-B satellite. Since that time, ranging precision has improved by a factor of a thousand from a few metres to a few millimetres.

Laser ranging activities are organized under the International Laser Ranging Service (ILRS) which provides global satellite and lunar laser ranging data and their derived data products. The ILRS was formed in 1998, in which there was approved 46 ILRS tracking stations, 4 ILRS Operations Centers, 3 ILRS Analysis Centers, 4 Lunar Analysis Centers, 18 Associate Analysis Centers, 2 Global Data Centers and 1 Regional Data Center.

The current configuration of ILRS is shown in the Figure 1.13.

The ILRS is composed by more than 40 ground stations, which routinely track satellites equipped with retroreflectors. Every ILRS station has these key components for SLR tracking: a high energy pulsed laser, an accurate timer, a precise photon detector and a well mounted and agile telescope.

CHAPTER 2

Tests of General Relativity

The investigation of the gravity nature is fundamental to understand the Universe and its evolution. The first efforts to test General Relativity (GR) started from Einstein himself; indeed he proposed three classical tests of GR.

2.1 Classical tests of General Relativity

GR theory was developed by Albert Einstein between 1907 and 1915. In order to establish observational evidence for this theory, Einstein proposed three tests, and in particular:

- the anomalous perihelion precession of Mercury's orbit;
- the deflection of light;
- the gravitational redshift of light.

2.1.1 Mercury perihelion precession

The first GR test deals with the orbital motion of the first planet of the solar system.

The Kepler's law describes the orbit of a planet around the Sun as an ellipse. Considering only the solar gravitational force, it is possible to obtain the law of Kepler using the Newtonian theory. However, also other planets carry out a gravitational force. The effect of these attractions results in a perihelion advance. Actually this "anomaly" is negligible for all planets with the exception of Mercury. Indeed it is the planet closest to the Sun, and thus, it is affected by the solar gravitational field more than other planets. For this reason, all but about 7% of Mercury motion is described by the Newtonian theory; the small anomaly, i.e. the precession of perihelion, corresponds to $43arcsec$ [38]. This discrepancy is too large to ignore.

The solution to this problem came when Einstein applied his GR theory to calculate Mercury's orbit. The missing $43arcsec$ are in perfect agreement with GR which can reproduce the observed precession exactly. For this reason, the precession of Mercury's orbit became an important observational verification of General Relativity.

2.1.2 Deflection of light

One prediction derived from the GR is the deflection of light. In particular, a ray of light travelling near a gravity source, i.e. a massive object, should be deflected. The natural tendency of light is that it can travel in straight lines, but it can be deflected by the presence of lens, mirror or also gravitational fields.

The only opportunity of observing this phenomenon was a light of a star passing near the Sun. An observer on the Earth can detect this light only during a total eclipse of the Sun (Fig. 2.1), when stars with apparent position near the Sun become visible. In other words, the star radiation becomes visible from the Earth, thanks to reduction of the solar luminosity due to the eclipse.

The first solar eclipse after the publishing of Einstein's works occurred on 29 May of 1919 over northern Brazil, the Principe islands and then across Africa. The first observation of the deflection of light was performed during this eclipse: two expeditions were organized, one in Brazil with Davidson and collaborators, and one in the small island of Principe with Eddington and collaborators [37].

Despite the observations were not as successful as had been hoped, important results were obtained by both two expeditions. Indeed the consistency with Einstein's prediction was impressive.

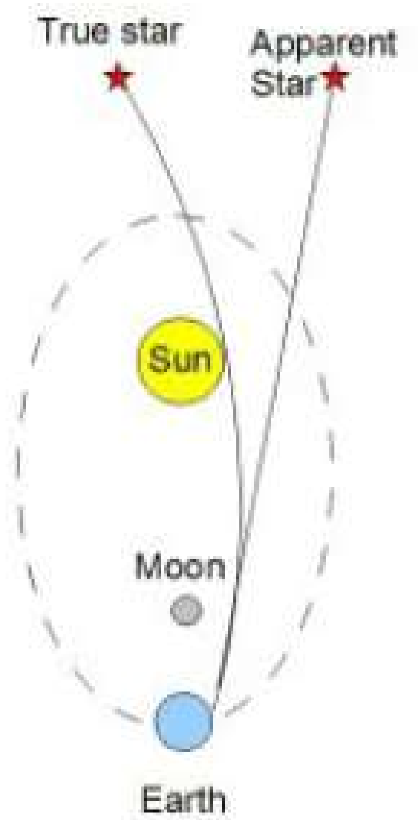

Figure 2.1: The scheme of the experiment aimed at the light deflection measurements.

2.1.3 Gravitational redshift

The third classical test of GR consists in an effect called gravitational redshift.

The electromagnetic radiation has a wavelenght: photons expend energy travelling in the Universe, and at the same time, they travel at a fixed speed, i.e. the speed of light; thus, the loss of energy corresponds to a change in frequency. If the energy of the photon decreases, the frequency decreases and the wavelenght increases: the latter corresponds to a shift to the red end of the electromagnetic spectrum, or in other words, to the gravitational redshift.

This measurement is very difficult to perform astrophysically. However, an innovative experiment was performed in 1959 using two sources situated on the top and bottom of the tower of Harvard's University. The result of this measurement was in agreement with GR [36].

2.2 Test of the Equivalence Principle

The high accuracy of LLR data allows precision tests of fundamental physics and constraints on gravity theories. These high-precision studies of the Earth-Moon-Sun system provide the most sensitive tests of several key properties of weak-field gravity, including Einstein's Strong Equivalence Principle (SEP), the variability of the gravitational constant, the best measurement of the De Sitter precession rate and the deviation from the gravitational potential.

The Equivalence Principle (EP) is the central assumption of the GR and is the exact correspondence of gravitational and inertial masses. Newton's law states that the force F is the result of the multiplication of an acceleration a and the inertial mass m_i as $F = m_i \cdot a$. In a gravitational field, and in particular, in Earth's gravitational field, this law is $F = m_g \cdot g$. For this reason, the inertial mass and the gravitational mass are equivalent. In other words, the accelerations of objects made of different materials are identical in the same gravitational field.

Its Weak form (Weak Equivalence Principle (WEP)) states that the motion of one body with others caused by gravitational interaction is independent of the structure, mass and composition of the particle. Therefore, each celestial bodies, as galaxies, stars or planets, move following the curves due to the geometry of spacetime, called geodesic. Also the motion of artificial satellites is determined only by the curve in spacetime, independent of properties like mass, composition and structure, but depending on its initial condition, i.e. position and velocity. WEP can be tested in laboratory or with astronomical bodies, since it underlies the geometrical structure of GR; it has been tested in very accurate experiments, like the classical Eötvös torsion balance.

The strong form of EP (SEP) extends the WEP including gravitational self-energy of a body; in other words, it is an assumption about the non-linear property of gravitation. In principle, General Relativity assumes that the SEP is exact; while alternative metric theories of gravity (scalar fields or extensions of gravity theories) predict a violation of the EP at some level. Therefore, probing the validity of the EP is one of the most powerful ways to test GR and search for new physics beyond the standard model [27].

EP tests generally deal with the universality of free-fall acceleration of test-bodies in a uniform gravitational field. Classical Eötvös type experiments are made by comparing the free fall accelerations of different test bodies (a_1 and a_2), using the torsion balance. Thus, considering gravitational and inertial masses of each body as M_G and M_I, the Equivalence Principle is given by:

$$\frac{\Delta a}{a} = \frac{2(a_1 - a_2)}{a_1 + a_2} = \Big(\frac{M_G}{M_I}\Big)_1 - \Big(\frac{M_G}{M_I}\Big)_2 \tag{2.1}$$

when the self-gravity of the test bodies is negligible and for a uniform external gravity field. Since laboratory masses lack measurable gravitational self-energy, it is possible to probe only the WEP with this technique.

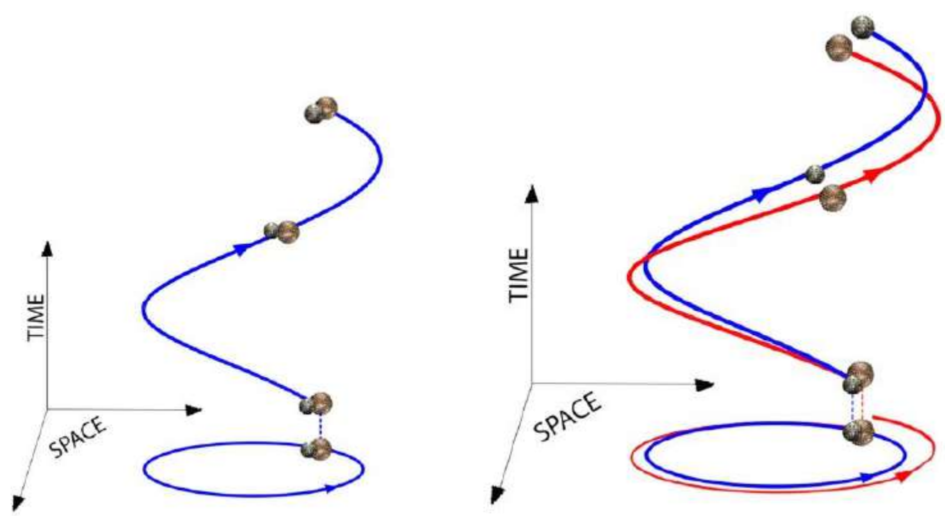

(a) (b)

Figure 2.2: The Equivalence Principle: (a) two bodies with the same initial conditions follow the same geodesic, projecting onto spatial plane an ellipse in this specific case. (b) Starting from the same conditions, two bodies do not follow the same spacetime curves if there is EP violation; the projection onto spatial plane will be two ellipses in this specific case [18].

However, it is possible to test the WEP and the SEP together, with the Lunar Laser Ranging (LLR) experiments: the Earth-Moon-Sun system is the best arena to test them. Regarding WEP, LLR compares the free fall acceleration of the Earth (E) and the Moon (M) toward the Sun:

$$\frac{\Delta a}{a} = \frac{2(a_E - a_M)}{a_E + a_M} = \Big[\Big(\frac{M_G}{M_I}\Big)_E - \Big(\frac{M_G}{M_I}\Big)_M\Big]_{WEP} \tag{2.2}$$

Any EP violation would cause the lunar orbit displacement along the Earth-Sun line, and it means a different falling of Earth and Moon towards the Sun (Fig. 2.2).

As already said, the SEP is the extension of the WEP covering the gravitational self-energy. In order to provide a pure SEP test, it is necessary to combine the general LLR measurements and the WEP results, given by the laboratory tests. Current LLR results give $2.4{\cdot}10^{-14}$ [30], that in combination with the laboratory tests yields to [13]:

$$\Big[\Big(\frac{M_G}{M_I}\Big)_E - \Big(\frac{M_G}{M_I}\Big)_M\Big]_{SEP} = -3.0 \pm 5.0 \cdot 10^{-14} \tag{2.3}$$

The development of the Parametrized Post-Newtonian (PPN) formalism is useful to test the viability of any gravity theory. It is characterized by ten parameters related to several features of each theory. In particular, in the SEP case, the ratio of gravitational to inertial mass is given by:

$$\Big[\frac{M_G}{M_I}\Big]_{SEP} = 1 + \eta\Big(\frac{U}{Mc^2}\Big) \tag{2.4}$$

where η is the PPN parameter, U is the body's gravitational self-energy ($U < 0$) and Mc^2 is the total mass-energy. For a test body the gravitational self-energy is given by:

$$U = \frac{G}{2} \int \frac{\rho(r)\rho(r')}{|r - r'|} d^3\mathbf{r} d^3\mathbf{r'} \tag{2.5}$$

Considering the test body as a uniform sphere of radius R, $U = -3GM^2/5R$, therefore $U/Mc^2 = -3GM/5Rc^2 \propto M$: SEP test bodies must have astronomical sizes. Anyway, due to the complexity of Earth and Moon interior structure, the U_E and U_M is calculated numerically [40].

$$\Big(\frac{U}{Mc^2}\Big)_{Earth} = -4.64 \cdot 10^{-10}; \Big(\frac{U}{Mc^2}\Big)_{Moon} = -1.90 \cdot 10^{-11}; \tag{2.6}$$

It is possible to rewrite the Eq. 2.4:

$$\Big[\Big(\frac{M_G}{M_I}\Big)_E - \Big(\frac{M_G}{M_I}\Big)_M\Big]_{SEP} = \Big(\Big(\frac{U}{Mc^2}\Big)_E - \Big(\frac{U}{Mc^2}\Big)_M\Big)\eta = -4.45 \cdot 10^{-10}\eta \quad (2.7)$$

From the latter and the Eq. 2.3, it is easy to calculate the SEP violation parameter η [40]:

$$\eta = (-4.4 \pm 4.5) \cdot 10^{-4} \quad (2.8)$$

In General Relativity $\eta = 0$; a value different from zero means a lunar orbit displacement about the Earth [64].

2.3 PPN parameters

In order to test and verify the GR or any alternative theories, the use of PPN formalism provides a series of parameters, which describe each feature of the theory. These parameters can be constrained with experimental and observational data.

The SEP violation parameter η is a linear function of PPN parameters β and γ.

$$\eta = 4\beta - \gamma - 3 \quad (2.9)$$

where β represents the degree of non-linearity and γ the size of space-curvature. In General Relativity both values are equal to 1; in this way $\eta = 0$.

The constrain of the γ parameter is given by Cassini spacecraft [12]. This measurement is possible considering a cornerstone of the GR: the deflection of the light due to the curvature of the space-time. The measurement of bending and delay is proportional to γ. The latter was computed thanks to the shift of photons from and to the spacecraft near the Sun. This is a very high accuracy result:

$$\gamma - 1 = (2.1 \pm 2.3) \cdot 10^{-5} \quad (2.10)$$

The γ measurement of Cassini and η measurement of SEP derived from LLR lead to a constrain on β parameter [13]:

$$\beta - 1 = (6.2 \pm 7.2) \cdot 10^{-5} \quad (2.11)$$

Each of three parameters result to a no significant deviation from the GR predicted values.

2.4 Temporal variation of the gravitational constant

The possibility of a temporal variation of the gravitational constant is a consequence of alternative gravitational theory. Indeed the General Relativity considers the G constant as a temporally and spatially invariable quantity.

Possible variations cause an anomalous evolution of the orbital periods of the astronomical bodies. Considering the third law of Kepler:

$$P^2 = \frac{4\pi^2 r^3}{Gm} \tag{2.12}$$

where P is the period, r is the semi-major axis of the body orbit. The time derivative of the latter:

$$\frac{\dot{G}}{G} = 3\frac{\dot{r}}{r} - 2\frac{\dot{P}}{P} - 2\frac{\dot{m}}{m} \tag{2.13}$$

It is possible to ignore the mass term for all solar system bodies (except for the Sun, due to a small rate of mass loss). A variation of the gravitational constant affects the monthly lunar orbit or also the annual Earth-Moon orbit around the Sun. Thus, in order to test these, the LLR sets a limit on $\dot{G}/G$; and in particular [13]:

$$\frac{\dot{G}}{G} = (0.2 \pm 1.3) \cdot 10^{-14} yr^{-1} \tag{2.14}$$

It means to a less than a 1% variation of the gravitational constant over 13.7 billion year age of the Universe. This result is improvable being the uncertainty of measurement proportional to the square of data; therefore, increasing LLR measurement and its precision, also this constrain can be improved.

2.5 De Sitter precession

Another of the several aspects related to the General Relativity is the geodetic precession or De Sitter precession, name derived by William De Sitter, who predicted this phenomenon. The precession consists in an effect due to the curvature of the spacetime on a moving and spinning body. Thus, it is clear that the Earth-Moon system is part of this scenario.

The geodetic precession is a three body effect, Sun-Earth-Moon. The moving body considered as a gyroscope is Moon around Earth; both are immersed in the gravitational field of the Sun (Fig. 2.3).

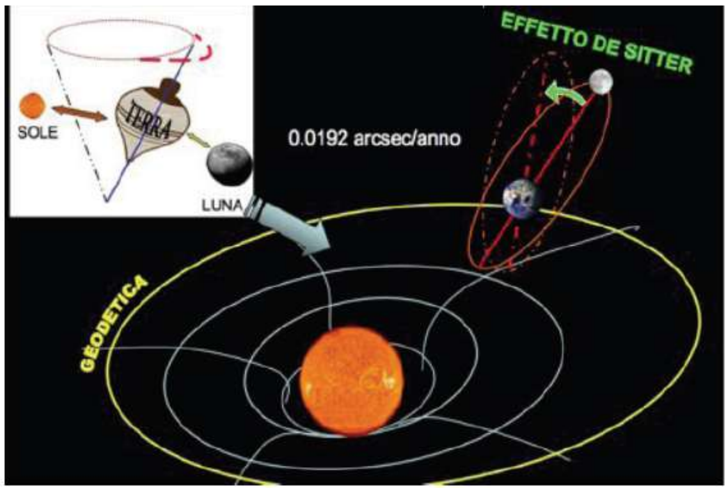

Figure 2.3: Sketch of De Sitter effect: the Moon precession orbiting the Earth in the Sun field.

The deviation of the geodetic precession from the GR is given by the parameter K_{GP}. LLR measurements are able to quantify this effect. The current limit is [64]:

$$K_{GP} = (1.9 \pm 6.4) \cdot 10^{-3} \tag{2.15}$$

2.6 Inverse Square Law Test

The Inverse Square Law (ISL) Test consists of a base of gravitational potential but with an additional contribution, often given by the Yukawa contribution. Thus, with this test type, a deviation from the $1/r^2$ is studied. While in the case of electromagnetism the particle considered are massless, other massive particles exchange gravitational force.

The Newtonian gravity is expressed by:

$$F = G\frac{m_1 m_2}{r^2} \tag{2.16}$$

The Yukawa potential is:

$$V_{Yuk} = -\alpha\frac{GM}{r}e^{\frac{r}{\lambda}} \tag{2.17}$$

where α is the dimensionless strength and λ is the length scale. The union of the two potentials gives [2]:

$$V(r) = -G\frac{m_1 m_2}{r}\left(1 + \alpha e^{-\frac{r}{\lambda}}\right) \tag{2.18}$$

The current results are given by addition of the perturbation, due to the Yukawa potential, to the equations of motion. With a $\lambda = 4 \cdot 10^5 km$ [49]:

$$\alpha = (3 \pm 2) \cdot 10^{-11} \tag{2.19}$$

While intriguing, this possible non-null result has yet to be thoroughly investigated.

2.7 Lense-Thirring Effect

One of the most peculiar prediction of GR is the frame dragging, also called Lense-Thirring (L-T) effect, which name derives from the physicists that firstly calculated this effect using Einstein's theory.

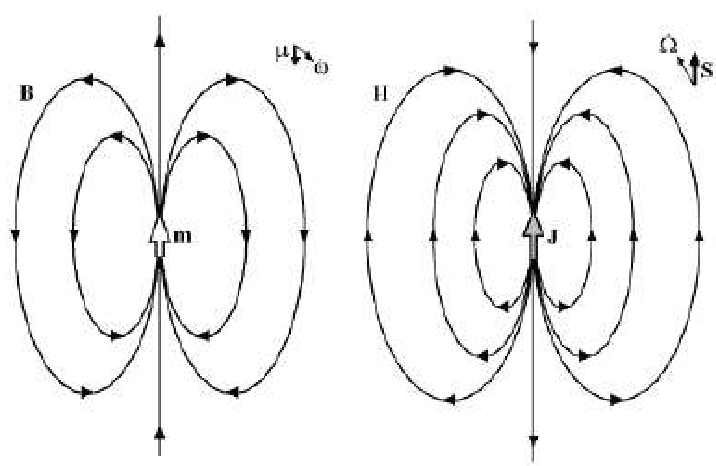

Figure 2.4: Magnetism and gravitomagnetism: in the left figure, the magnetic field B, generated by a electric current distribution with magnetic moment m and its effect on magnetic dipole μ; in the right figure, the gravitomagnetic field H, generated by the angular momentum J and its effect on a test gyroscope with spin S.

The L-T effect is a consequence of the gravitomagnetic field. This field is analogous to the electromagnetic field: indeed, while in the latter the electric currents generate the magnetic field, in the gravitomagnetic field the mass currents generate it. Therefore, a satellite orbit is dragged by the gravitomagnetic field produced by the angular momentum of the central body. L-T effect is formally similar to the behaviour of a magnetic dipole in a magnetic field generated by the electric current (Fig. 2.4).

The resulting L-T effect can be thought as a dragging of inertial frames, as also suggested by the "frame-dragging" name. In GR, the axes of local inertial frames are determined by gyroscopes. However, gyroscopes are not fixed with respect to "fixed stars", as in classical mechanics, but they are dragged by the mass currents.

A test mass motion in free fall is different in the presence or not of a large massive spinning sphere. For example, near the Earth, the inertial motion of one test mass is not the same as that in far space (away from gravitational sources); indeed, near the Earth the motion is different due to L-T effect. In particular, this effect is very tiny around Earth, but very huge around massive objects like rotating black holes.

CHAPTER 3

SCF Laboratory

The SCF_Lab (Satellite/Lunar/GNSS laser ranging altimetry Characterization Facilities Laboratory) is a clean room inside National Laboratory of Frascati of National Institute of Nuclear Physics (INFN).

Figure 3.1: SCF_Lab Clean Room in INFN-LNF.

The laboratory consists of $85m^2$ class 10,000 Clean Room (ISO 7), in which adequate condition to test optics are guaranteed avoiding any dust particle, that could decrease the test integrity.

The clean room has two separate entry areas for personnel and equipment; the rest of the laboratory is divided in two other areas, one for the SCF (white cryostat is shown in Figure 3.1) and one for the SCF-G (where -G stands for Galileo optimized, not visible in the Figure); the latter is the facility used for all tests described in this thesis.

Both facilities are designed to characterize the thermal and optical properties of the CCRs for LLR and SLR in a simulated and realistic space environment (in terms of pressure and temperature); they can reach a pressure less than $10^{-6} mbar$ and a temperature around $77K$ in the operative phase. In order to do these tests, for each facility there are a Solar Simulator (SS), a InfraRed (IR) camera and an optical table outside the cryostat.

3.1 SCF-G and cryogenic system

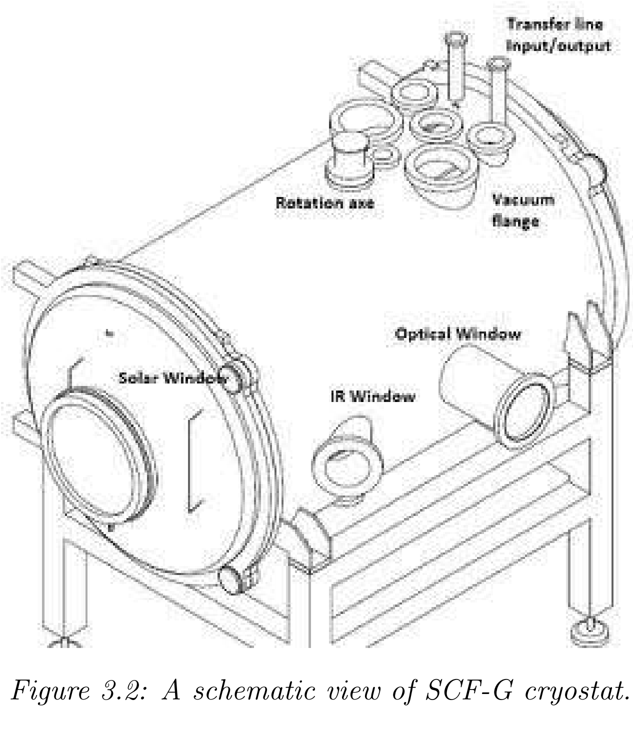

Figure 3.2: A schematic view of SCF-G cryostat.

The SCF-G is a steel cryostat, with a length of 2 m and a diameter of about 0.9 m. The copper shroud inside the cryostat, painted black with

Aeroglaze Z306 (0.9 emissivity and low-out gassing) which brings the temperatures down to $\sim$ 77K, has a copper coil, welded onto the external surface of the shield. In order to arrive to this low temperature, the copper coil is fluxed with liquid nitrogen. The copper shroud is then covered with Multi-Layer Insulation (MLI) to enhance thermal insulation and reduce the nitrogen consumption; this is accomplished however, not only with thermal insulation, but also with a flowmeter positioned at the very end of the circuit, which regulates nitrogen flow rate.

On the top of the cryostat there are two distinct positioning systems: one for spherical rotations and one for roto-translation of the payload. In this way, the payload can rotate in front of the SS window, aligned to the longitudinal axis of the cryostat, IR camera window, at 45° with respect to the longitudinal axis, and laser beam window, normal to the same axis (Fig. 3.2). A further schematic view of the cryostat is shown in Figure 3.3 to understand better the movements system of the payload.

The vacuum is achieved using a two stage pumps system: first of all a rotatory pump is used for low vacuum, while second step is the use of a turbo-molecular pump in order to obtain the high vacuum.

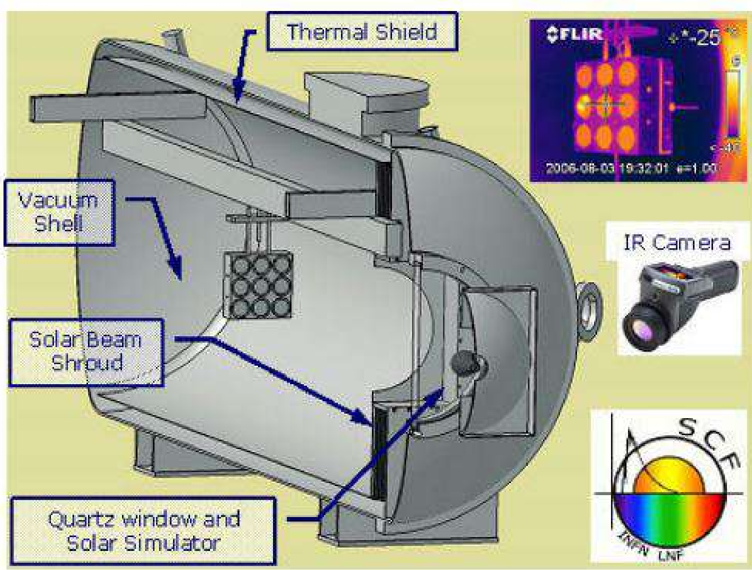

Figure 3.3: SCF-G cryostat section drawing.

The rotary pump is located outside the clean room (Fig. 3.4(a)); it is

(a) Rotary pump. (b) Turbo-molecular pump.

Figure 3.4: The two pumps of the SCF-G cryostat.

used as well as for the pre-vacuum phase also in backing pumping mode for the turbo-molecular pump. This pump has two different valves: "rough" and "fine". The first is used to connect directly the SCF-G to the pump, in order to reach the pre-vacuum condition with a pressure around $10^{-1} mbar$. The second valve is fundamental to put the rotary pump in backing pump with the turbo-molecular one.

The turbo-molecular pump is located inside the clean room (Fig. 3.4(b)), below the SCF-G. It is connected to the cryostat through the "Gate" valve. After the reaching of the pre-vacuum condition, the "rough" valve is closed and thus the "fine" and the "gate" valves are opened. In this way, it is possible to reach the operative conditions, that is high vacuum with a pressure at least $10^{-6} mbar$.

The Liquid Nitrogen (LN2) cryogenic system is designed to cool down the system after reaching the pressure operative conditions. The LN2 tank is placed outside the clean room; it flows through a first transfer line and goes inside the cryostat. Once cooling down the shroud, the nitrogen flux proceeds towards the second transfer line, located outside the cryostat; through a heating pipe the LN2 heats up, and through the flowmeter and an exchanger the nitrogen turns into gas and can go safely outside the laboratory.

3.2 Solar Simulator

The Solar Simulator (SS) of SCF-G is manufactured by TS Space Systems LTD. The SS is capable to provide a $40cm$ diameter beam with a radiation

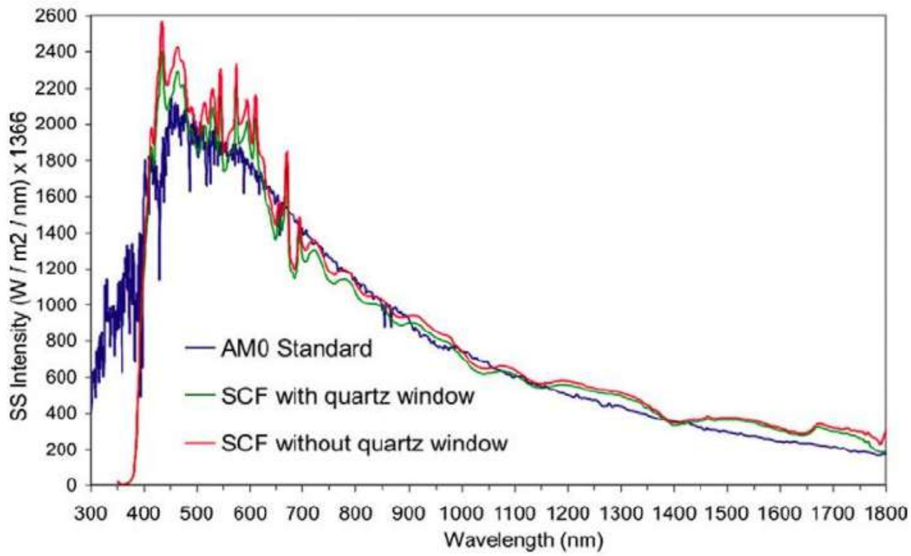

Figure 3.5: SS spectra of the SCF with and without quartz window in comparison with AM0 [28].

emitted almost equal to $1366.1 W/m^2$ i.e. the Air Mass Zero (AM0) of 1 solar constant in space. The spectrum shape is formed thanks to a metal halide arc lamp, UV-V range, and a quartz halogen, tungsten filament lamp, Red-IR range.

On the SCF-G there is the solar quarz window, through which the SS can illuminate the payload inside the cryostat.

Figure 3.5 shows the solar spectrum, with respect to a realistic AM0, outside the Earth atmosphere in the interval $400 - 1800nm$.

3.3 IR camera

The InfraRed camera is used to know the temperature of the payload with a non-invasive thermometry. The camera is a digital camera with a Charge-Coupled Device (CCD) designed to operate in the infrared radiation spectrum, i.e. range $7.5 - 10\mu m$. It takes IR pictures, with a resolution of 640x480 pixels, and is able to do an electronic automatic zoom, with an accuracy of $\pm 2K$ for single spot.

Knowing the environment humidity and temperature, reflected apparent temperature and distance between spot on the object and camera, it is possible to measure the temperature of a specific with known emissivity. However the humidity in vacuum could be considered equal to 0, the distance could be useless because of no absorption/emissivity in IR range, thus the reflected apparent temperature is needed to calibrate the camera. The total radiation acquired by the camera is equal to:

$$W_{tot} = W_{obj} + W_{ref} \tag{3.1}$$

where W_{obj} is the interested signal, i.e. the radiation emitted by the object, and W_{ref} is the environment radiation reflected, in other words the noise background signal. Assuming that in vacuum the only thermal exchange possible is radiative:

$$W_{tot} = A_{obj} \cdot \sigma \cdot \epsilon_{obj} \cdot (T_{obj}^4 - T_{env}^4) + A_{obj} \cdot \sigma \cdot (1 - \epsilon_{obj}) \cdot (T_{ref}^4 - T_{env}^4) \tag{3.2}$$

where:

- W_{tot} is the total IR radiation collected by the IR camera;
- A_{obj} is the object surface;
- σ is the Stefan-Boltzmann constant $(5.67 \cdot 10^{-8} W/m^2K^4)$;
- ϵ_{obj} is the emissivity of the object;
- T_{obj} is the temperature of the object;
- T_{env} is the temperature of the environment;
- T_{ref} is related to the blackbody approximation of the radiation emitted by the environment and reflected by the object to the camera.

In order to obtain the object temperature:

$$T_{obj} = \sqrt[4]{\frac{1}{\epsilon_{obj}} \cdot \left[\frac{W_{tot}}{A_{obj} \cdot \sigma} - (1 - \epsilon_{obj}) \cdot (T_{ref}^4 - T_{env}^4) \right] + T_{env}^4} \tag{3.3}$$

Actually all steps are carried out by the IR camera Software, after setting the reflected temperature, found through a certain calibration procedure.

3.4 Optical bench

The optical bench is one of the fundamental part of the SCF_Lab, because it is used to simulate the laser ranging process. The bench is a specific table on which the optical instrumentation is installed; it has an anti-vibration pneumatic suspension, in order to resist to movements due to laboratory personnel.

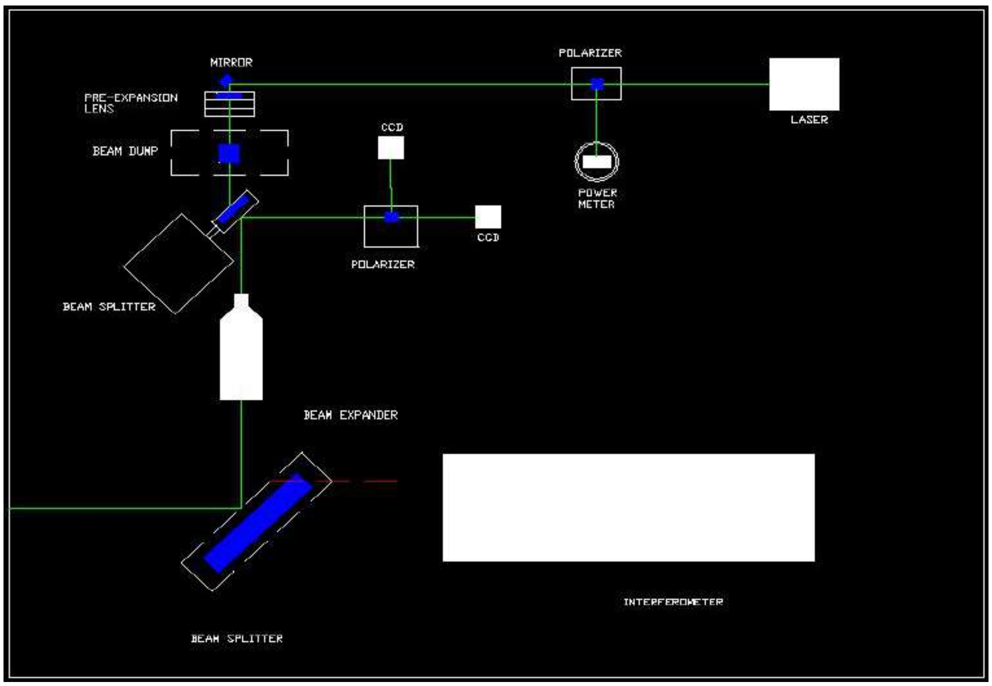

Figure 3.6: Optical circuit for the FFDP.

The laser generates an intense beam of coherent monochromatic light at 532 nm.

Following the path of the laser (Fig. 3.6), it encounters:

- **Polarizer**: an optical filter, that allows the passage of only the horizontal component of the laser beam.
- **Power meter**: tool used for the monitoring of the laser intensity.
- **Mirror**: circular mirror with $2cm$ of diameter to bend the trajectory of the laser beam.

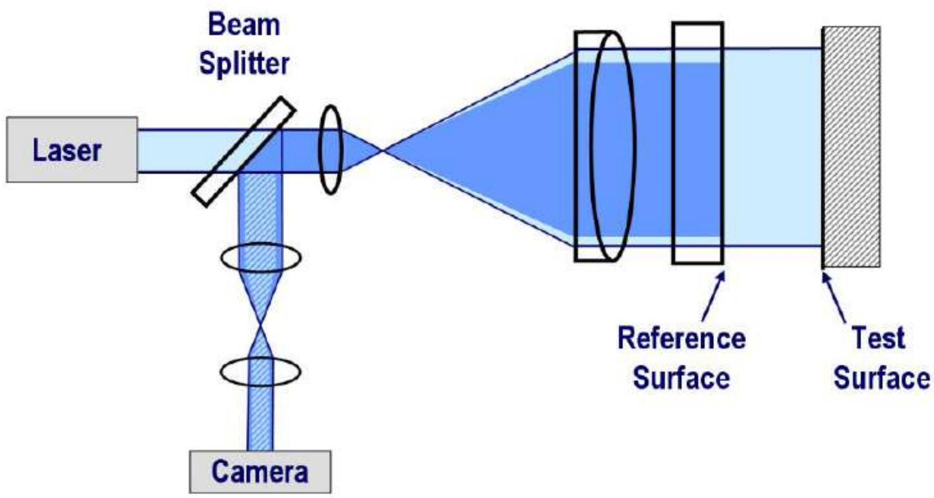

Figure 3.7: Fizeau Interferometer scheme.

- **Pre-expansion lens**: used to expand the laser beam.
- **Beam dump**: safety device that absorbs the incident laser beam, used to block the beam when it is necessary.
- **Beam expander/reducer**: device that increases or decreases the diameter of an input beam.
- **Beam splitter**: device that splits an incident light beam into two or more beams. In the optical bench it is used to bend and split the beam entering the cryostat through the optical window and afterwards, to bend the beam during the returning phase of the laser retroreflected by the retroreflector inside the cryostat.
- **Beam-splitting polarizer**: device that splits the beam into two beams with opposite polarization states; the latter reaches respectively the horizontal CCD and vertical CCD. The horizontal and vertical polarization components of each FFDP are recorded separately. This operating way is fundamental for uncoated CCR, whose FFDP have a strong dependency on the orientation of the input linear polarization; while there is no dependency expected for coated CCR, as already described in Section 1.2.

- **CCD laser beam profilers**: Charge-Coupled Device (CCD) is an integrated circuit on which incident photons generate charge, read by electronics and turned into digital copy of the light patterns incident on the device.

- **Interferometer**: tool that uses a source of light to create an interference pattern. This device enables the test of the surface optical quality of CCRs, as Dihedral Angle Offset (DAO). The Wavefront Fizeau Interferometer (WFI) (Fig. 3.7) consists of a beam splitter which divides the beam from a laser source. The test beam is directed to the retroreflector to test, which returns back until to the Camera.

3.5 Control and acquisition electronics

All control and acquisition software are developed with LabVIEW of National Instruments (NI) by SCF_Lab team. The aim of these software is monitoring and controlling the related instrumentation during the test phases. In particular, during a standard test, the control and acquisition system must provide the control of payload movement and heating system, and the acquiring of the chamber vacuum pressure within the temperature probes (shroud plus payload probes).

3.5.1 Temperature data acquisition system

Two different PT100 probes circuits are installed on the Shroud, each one with 24 probes, in addition other probes are installed on the payload in test phases. All of these probes, the flowmeter temperature reading probe and solar window probe are connected to the PC with a NI compact Field Point (cFP) 2220.

The vacuum pressure reader is connected to cFP with a serial connection. Finally the cFP 2220 is connected to the PC with an ethernet connection and a dedicated LabVIEW software (Fig. 3.8) acquires and controls all of these elements in "real time". With the acquisition program all the temperature and pressure data are automatically saved in the cFP internal memory.

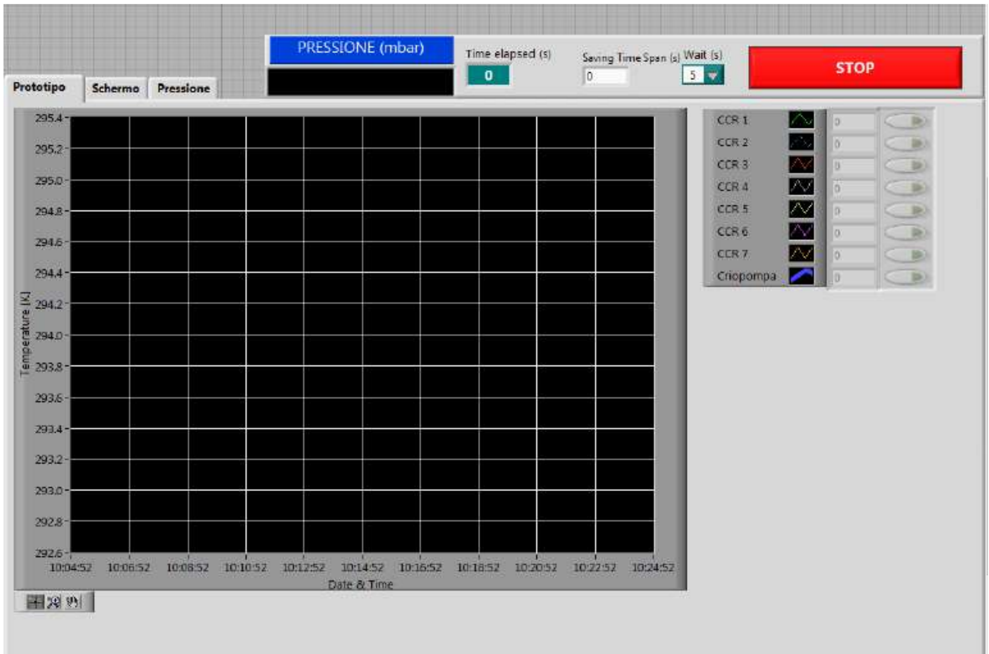

Figure 3.8: Screen of LabVIEW data acquisition software.

3.5.2 Movement and rotation

The movement system allows the payload to rotate on its axis of more than 280°, starting from the cool shield (−90° with respect to the solar window) until to the optical window (90° with respect to the solar window).

The movement is provided by stepper motors, which working is allowed by a controller. The latter is connected to the PC with a serial-ethernet connection. In addition a potentiometer is installed on the external rotation axis: thus, it is possible to read the absolute position of the rotation axis.

The system is also able to rotate the payload. Both for the movement and for the rotation, a dedicated software is used (Fig. 3.9). The user can rotate the payload manually, choosing between a relative movement from the last position or an absolute rotation from the default position.

A set of indicators report the status of the movement system (if it is moving or not), the actual position acquired by the controller along with the position acquired by the potentiometer, and eventually the limit status that define the "zero" value for the absolute movement.

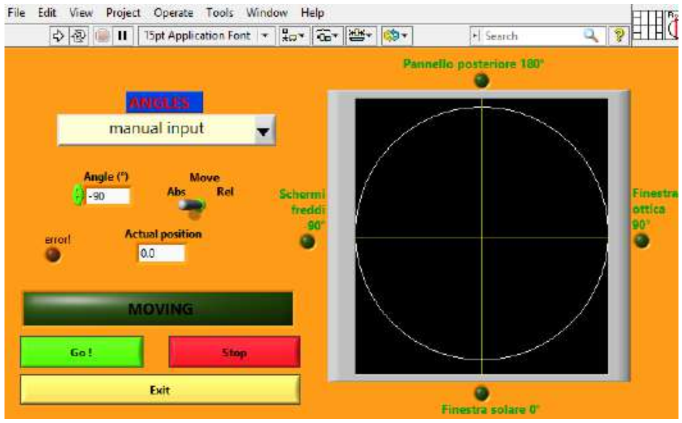

(a) Movement

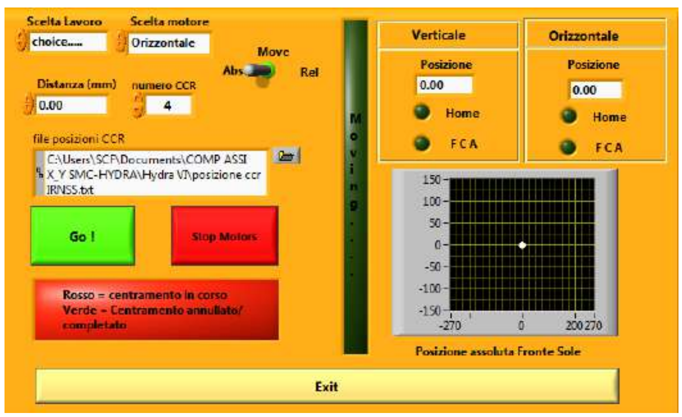

(b) Rotation

Figure 3.9: Screen of movement and rotation software.

3.5.3 Flowmeter control

In order to control the nitrogen flux, a custom board for the flowmeter analog control is connected to cFP with a Digital Analog Input/Output module.

As the acquisition system, also the flowmeter has a software (Fig. 3.10) in which it is possible to control the flux in real time.

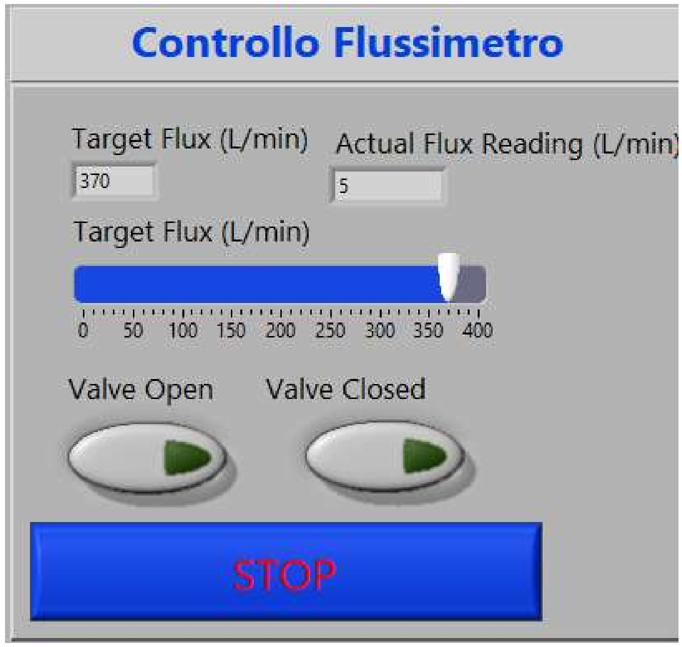

Figure 3.10: Screen of LabVIEW flowmeter software.

3.5.4 Heaters

On the shroud a series of Kapton Heaters tape are installed in order to rapidly increase the shroud temperature from 90K to 300K and return in "air" conditions.

Moreover, in order to ensure a thermal control of the payload, other heaters tapes can be installed on it. Each heaters is connected to a power supply, which is connected to cFP with a Digital Analog Input/Output module and its operations are controlled by a dedicated software (Fig. 3.11). It is possible to choose the working mode: the automatic and manual mode. In the manual mode, the user manually sets the desired current for the specific heater tape. The automatic one allows to set the setpoint temperature and the software automatically controls the power supply to reach the desired temperature. In order to keep the setpoint temperature almost fixed, the software uses the Proportional-Integral-Derivative (PID) control.

The objective of a PID controller is to maintain the output in such a way that the error between the process variable and the set-point or the desired output is zero. The behavior is divided into 3 configurations: proportional,

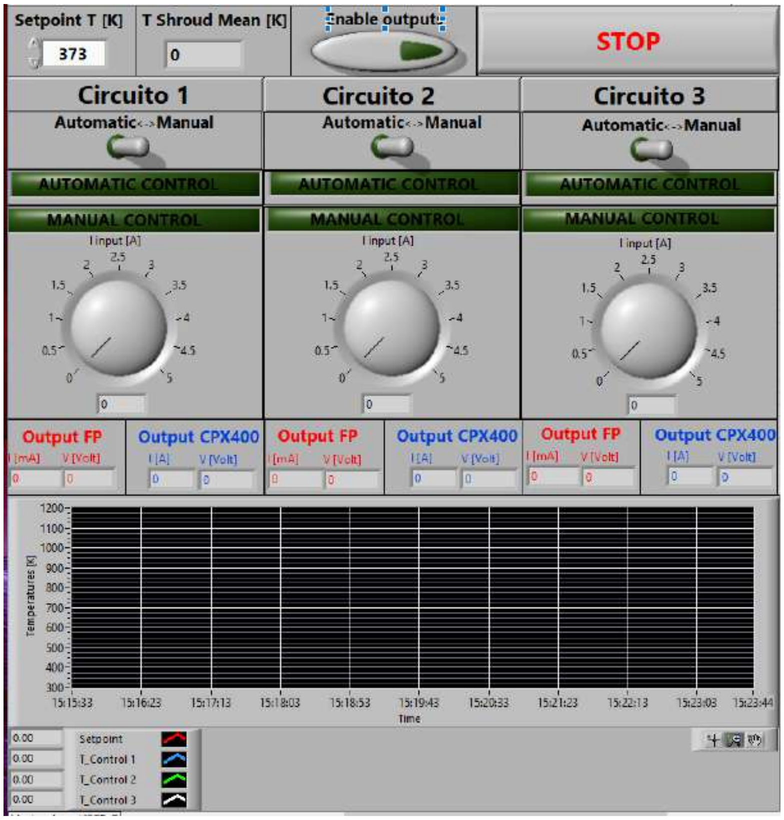

Figure 3.11: Screen of heaters software.

integrative and derivative.

The proportional controller provides an output proportional to the error, which compares the desired value with the current value. The integrative controller provides the necessary action to eliminate the steady-state error related to the only proportional controller. Indeed it integrates the error for some time until the error value reaches zero. Integrative control decreases its effectiveness when a negative error occurs. The derivative controller predicts the behavior of the system and therefore improves the sedimentation time and the stability of the system.

In general, typical steps for designing a PID control are the following:

- P: to decrease the rise time;
- I: to eliminate the steady-state error;

- D: to reduce the overshoot to settling time.

3.5.5 TVT

Thermal vacuum test (TVT) is a way of mitigating risk and preparing for the extreme temperatures encountered in space environment. During the life cycle of units used in satellites or spacecraft, their performances should be considered by simulating the operating environment under high vacuum conditions with different thermal cycles. TVT simulates high vacuum orbit conditions, extreme temperatures, and solar radiation.

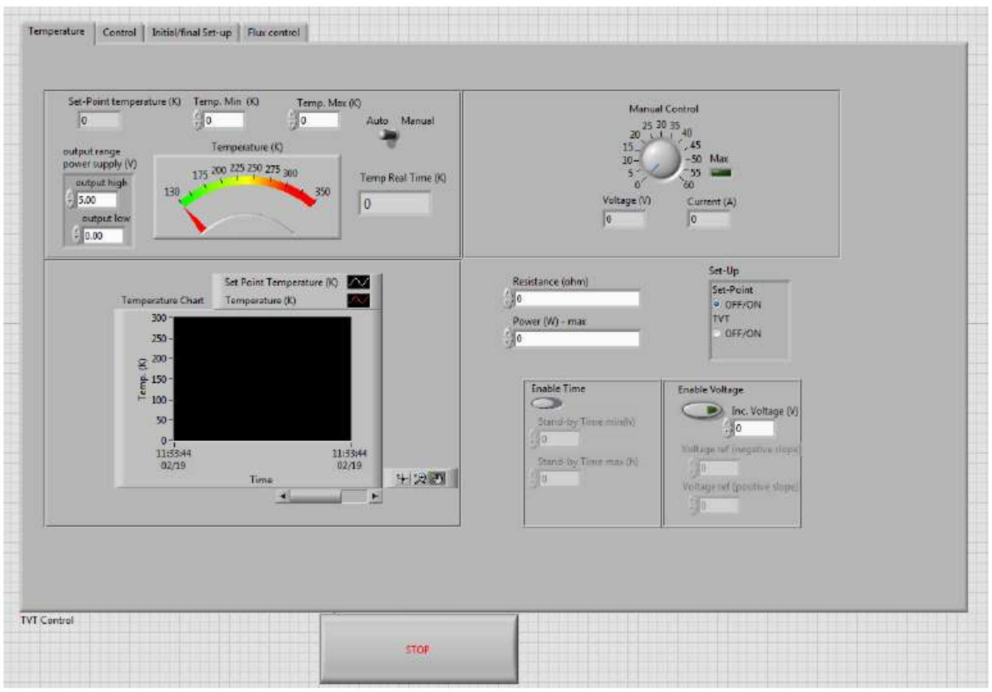

Figure 3.12: "Temperature" TAB of TVT software.

The thermal vacuum test subjects the unit to thermal cycles in a vacuum environment. Without convection heat transfer, the unit generally travels at a lower temperature than the heat cycle test, generating less thermal stress. The vacuum environment, however, provides a realistic flight condition for the unit to be used in space flight, which then results in thermal gradients that are more in keeping with the flight environment. Conductive and radiative heat transfer in the test will be like flight expectations. This is achieved through functional tests performed in the plateau at the hot and cold temperature on each cycle for a certain number of hours, with constant variations in the transition between the two temperatures.

As already described, the high vacuum is implemented using different pumping systems, while high and low temperatures are generated with the help of heating resistances and thermal walls using nitrogen as a heat transfer medium. A feedback control PID algorithm manages the various test operations automatically, respecting the standard aerospace test requirements.

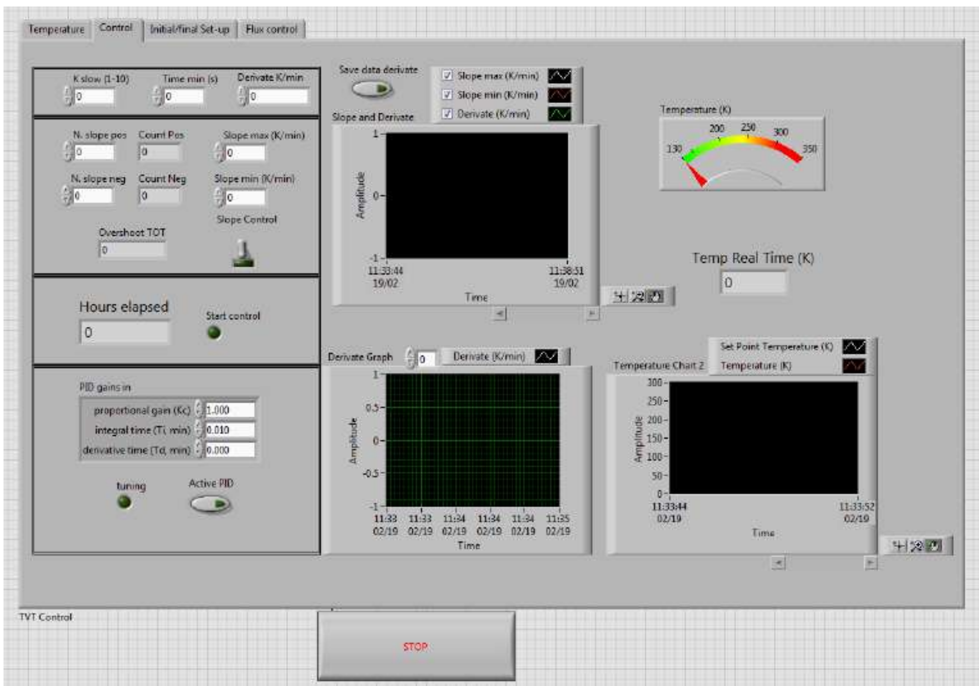

Figure 3.13: "Control" TAB of TVT software.

The software starts with the initialization of various variables and with the real-time temperature reading. The latter is carried out every 300 milliseconds. The real-time value is saved in an array of temperature. In order to avoid overloading the CPU, this array is reset every ten seconds. The derivative of temperature is calculated with a different time range based on the value of the derivative itself according to slope parameters.

The behavior can happen in two ways: with the slope control plus PID, or just with the PID. In the first case, the Slope control modifies the voltage (increasing or decreasing the value) if the derivative is out of the predetermined interval, given by Slope min and Slope max chosen by the user (Fig. 3.13). Once the temperature reaches the set-point temperature, PID starts to keep fixed the temperature. In the second case, PID starts directly to reach the setpoint with the control given by PID parameters. After reaching the set-point, the temperature remains constant for a set time by enabling the button "Enable Time" and by setting the standby time (Fig. 3.12). After this time, the setpoint temperature changes from minimum to the maximum value or vice versa, and a new slope can start. The minimum and maximum temperature values are set by the user in "Temp Min" and "Temp Max" related to the Figure 3.12.

3.5.6 Environment control

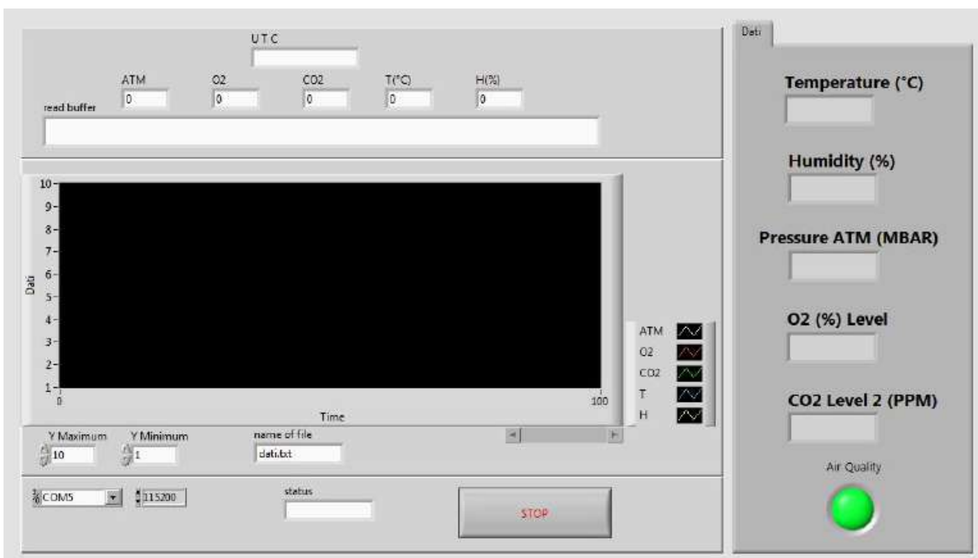

Figure 3.14: Screen of environment control software.

In order to monitor the environmental parameters in laboratory, a sensors system is built. Through a LabVIEW interface (Fig. 3.14) it is possible to supervise each parameter related to the clean room environment.

The System consists of a leading control platform, Arduino due, a series of sensors and the GPS with User Datagram Protocol (UDP) connection for time synchronization. Sensors used are:

- BMP280: the sensor for pressure measurement;
- SHT31: the sensor for temperature and humidity measurements;
- Sensirion CO_2: the sensor for CO_2 level measurement;
- Gas Sensor O_2 winsen: the sensor for O_2 level measurement;
- GPS with UDP connection.

Each of these parameters are saved in a document, with the related date and hour. Moreover, they are plotted in the interface screen.

The temperature must be $(20 \pm 2)°C$. The humidity must be between 40% and 60%. The pressure must be around $1atm$ or $1013mbar$, but it is acceptable in a range of $\pm 30mbar$. The optimal oxygen level is 20.9%, but it is acceptable in a range between $19\% - 23\%$, while the carbon dioxide must be under $1000ppm$. If one of these parameters is out of these ranges, the air quality button becomes red.

CHAPTER 4

SLR/LLR Results and Improvements

In order to improve SLR and LLR data, it is necessary to build new payloads, as described below.

4.1 LARES-2

Satellite Laser Ranging is used in several research fields, such as geodesy, geodynamics and Earth-science; however, the aim of this section is to understand the state-of-the-art in fundamental physics and how to improve it.

The geometrical structure of GR is based on the Equivalence Principle (EP). It is possible to test the Weak form of the EP through the SLR technique: the satellites currently in orbit is considered as free falling particle. LAGEOS, LAGEOS-2 and LARES are composed of materials never previously tested, i.e. aluminum and tungsten. By comparing the residual radial accelerations of these three satellites, it is possible to obtain a test validating the weak equivalence principle and in this way the General Relativity. Indeed alternative theories of gravitation predict deviations from the uniqueness of free fall; the latter was confirmed over ranges $7820km$ and $12270km$ with an accuracy of $\sim 10^{-9}$ [18]. Even if LAGEOS and LAGEOS-2 are very similar, they differ in composition and orbital radius from LARES: for this reason it is possible to constrain also $\dot{G}/G$ to one part in 10^{-9} [18], over the same altitude range. Moreover, from the WEP derives the gravitational to inertial mass ratio m_g/m_i: if there is a violation of the WEP, m_g/m_i may be different between the aluminum/brass of the LAGEOS satellites and the tungsten alloy of the LARES satellite.

With the first satellite, LAGEOS, SLR data aimed to measure another general relativity effect, the frame-dragging that induces a tiny drift of the satellite node, called Lense-Thirring (L-T) effect. The rotation of a mass generates additional space-time curvature; this phenomenon is very similar with magnetism in electrodynamics and it could be called gravitomagnetism [24]. Frame-dragging has a huge effects in a very strong gravitational fields, as around rotating black holes; but it is very tiny around the rotating Earth. The consequence of this effect of a rotating planet is a precession of the angular momentum of its satellite, with the same sense of rotation of the central body (Fig. 4.1). In other words, the L-T drag is a change of orientation of the intersection of satellite orbital plane with the equatorial planet plane, also called nodal line.

However, there is another effect on the node of satellites derived by the non-sphericity of the terrestrial gravity field; it is a shift induced by Newtonian effects. This non-relativistic effect is several orders of magnitude larger than the relativistic one. The uncertainties in gravitational and non-gravitational perturbations, on one single satellite, are bigger than the L-T effect. Using a combination of satellites, LAGEOS, LAGEOS-2 and LARES satellites, it is possible to reduce the uncertainties and to make an accurate measurement of frame-dragging with an almost high accuracy (from 2% to 5% [23]). Adding a new satellite in a supplementary[1] orbit with respect to LAGEOS will reduce the uncertainties [21] and will improve by about an order of magnitude (0.2% error of frame-dragging) the present state-of-the-art of this phenomenon [23]. The non-relativistic effect is equal and opposite for two satellites with supplementary inclinations whereas the L-T effect is in the same sense of rotation of the Earth, independently of their inclination.

Moreover, SLR data of this new constellation will be able to put stronger limits on some alternative fundamental physics theories. Finally, the inclusion of new targets for the ILRS will provide new contribution to Earth science, geodesy and geodynamics.

One of these new targets is the geodetic satellite LARES-2. LARES-2

[1]Supplementary inclinations: $i_1 + i_2 = 180°$.

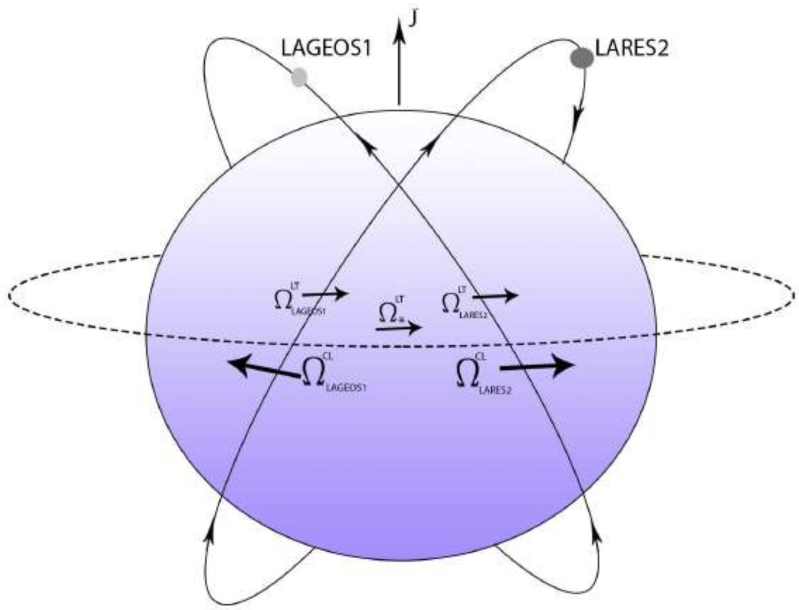

Figure 4.1: The idea of LARES-2 experiment: the frame-dragging or Lense-Thirring (L-T) effect and the non-relativistic effects, compared to those of the LAGEOS satellites, are shown [23].

is a passive spherical satellite with a diameter of about $42cm$ and a mass of $395kg$, obtained from a single, high-density block of nickel alloy. The satellite is designed to reduce the surface/mass ratio. Its operational orbit is expected to be circular (in order to minimize the non-gravitational perturbations) with a nearly $6000km$ altitude (the same semimajor axis of LAGEOS) and a $70°$ inclination, supplementary to that of LAGEOS.

LARES-2 is covered by 303 CCRs, each one with a diameter of 1 inch ($2.54cm$). The innovation of this experiment consists of the choice of retroreflectors Commercial Off-The-Shelf (COTS). The use of CCRs COTS eliminates costs as an obstacle to using smaller cubes, but they can be different from ideal CCRs. Indeed this type of retroreflectors could be smaller or bigger than the nominal value and could have a Dihedral Angle Offset (DAO) different from zero (ideal case). The compromise consists of a precise geometrical and optical analysis and an accurate choice of CCRs in compliance with experiment requirements. Details in chapter 5.

4.2 MoonLIGHT

The current lunar payloads, i.e. Apollo 11, Apollo 14, Apollo 15, Lunokhod 1 and Lunokhod 2, are arrays composed by small CCRs with a diameter of $3.8cm$. Their design produces strong limitations in Lunar Laser Ranging measurements due to a lunar phenomenon, called lunar librations. The librations derive from the eccentricity of the Moon's orbit around the Earth: during the 28 days lunar phase, the Moon's rotation alternatively leads and lags its orbital position, of about 8 degrees. Therefore, the arrays are moved and one corner of the array is more distant than the opposite by several centimeters. For this reason, the dimension of the pulse coming back to the Earth is greater proportionally to the array physical dimensions and to the Moon-Earth distance increase (in the position in which the libration phenomena are at the peak).

The laser pulse enlargement [39]:

- for Apollo 15 array: about $30cm$, with a $\pm 0.5ns$ increase of flight time;
- for Apollo 11 and Apollo 14 arrays: about $15cm$, with a $\pm 0.25ns$ increase of flight time.

It is important to underline that the Apollo 15 array is the largest array on the Moon; therefore the laser pulse enlargement is greater.

In order to reduce the uncertainty of the LLR measurements, the ground stations like APOLLO use the photon number: it is possible to reach the millimeter level reducing the uncertainty of $\sqrt{N}$, i.e. through a greater photon rate [45]. Therefore without hardware upgrades of lunar retroreflectors, the only available improvement is on the timing of an extremely large number of photoelectron returns to reduce the errors by the root mean square of the single photoelectron measurement.

The SCF team, in collaboration with the University of Maryland, proposed the 2^{nd} generation of lunar CCR, with a new design unaffected by lunar librations [26]. The key idea is to use, instead of an array of multiple small CCRs (for example $3.8cm$ of front face diameter for Apollo), a series of single big retroreflectors, each one with $10cm$ of front face diameter, called Moon Laser Instrumentation for General relativity High accuracy Test (MoonLIGHT), deployed separately on the lunar surface (Fig. 4.2). This new design creates single short reflected pulses with a final precision expected to be better than a few millimeters. Once this new kind of CCR will

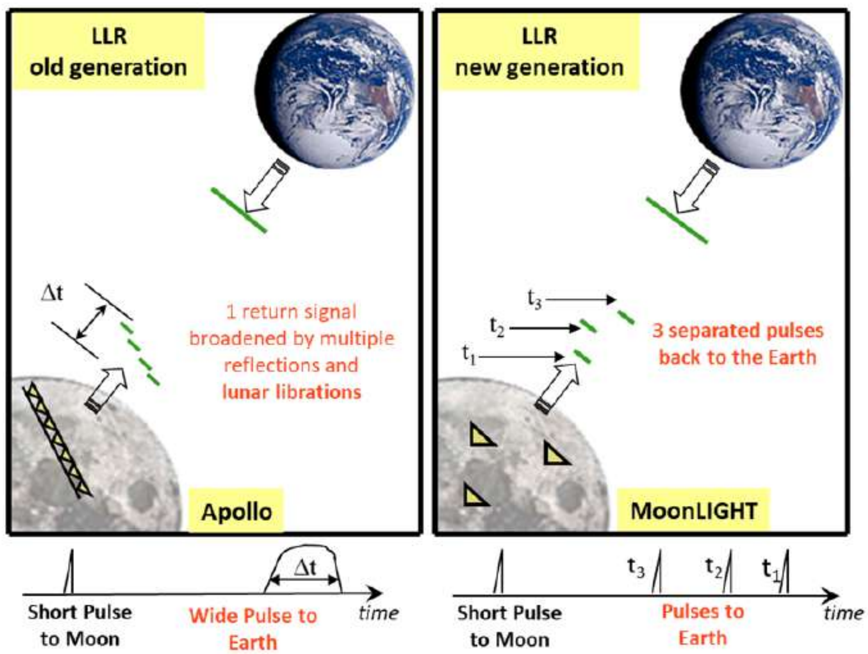

Figure 4.2: Comparison between first and second generation of CCR [39].

be deployed on the Moon, further improvements in the laser ground stations capabilities with shorter laser pulses will be more effective.

Thus, it is possible to compare the evolution of the LLR in terms of measurements uncertainty: in the past the laser pulse was wide, bigger than the array dimensions; for this reason, the uncertainty is dominated by the laser. Now the laser pulse is improved, but there are still large arrays; therefore the uncertainty is dominated by the arrays. In the future, with MoonLIGHT, there will be a single large CCR minimizing the effect of librations. The uncertainty will be dominated by the laser pulse again; but the modern technology can do shorter laser pulses (Fig. 4.3).

4.2.1 Planetary Ephemeris Program

The simulated or real LLR data can be analyzed with several software. The SCF_Lab team uses the Planetary Ephemeris Program (PEP) software [15], developed at Center for Astrophysics starting from the 1960's. In addition to generate ephemerides of planets and Moon, PEP was designed to

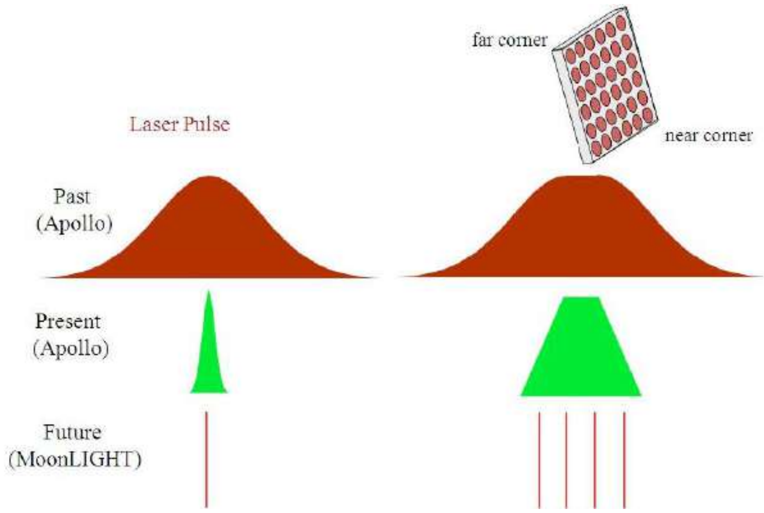

Figure 4.3: Comparison between the measurement uncertainty between laser pulse size fired and retroreflected: on the top it is shown the past situation, in the middle the current one and on the bottom the future.

compare models with observations. In this way, PEP can be used to establish constraints on standard physics parameters, as PPN parameters β and γ, geodetic precession and the variation of the gravitational constant $\dot{G}/G$ [10] [54].

PEP is an open source software package, written in Fortran [15]. This software includes detailed mathematical model of the solar system, through several parameters, and some of these describe fundamental physics. It is possible to restrict the range of physics parameters, estimating the latter based on the available data. To do this, the software is able to calculate the residuals of the distances between observed and computed LLR data, that also derive from GR expectations.

The state-of-the-art of the LLR measurements are summarised in the Table 4.1. Tests of General Relativity performed with Apollo and Lunokhod arrays has reached the accuracy of few centimeters.

PEP software is able to simulate LLR artificial observations, supposing new CCRs on the lunar surface. In this way, it is possible to verify the improvement of the accuracy of each GR parameter.

In Table 4.2 the simulated improvements achievable with the new generation retroreflector are listed. The estimated accuracy is 1 millimeter order of magnitude, but it may reach 0.1 mm after several years of measurements.

Test of General Relativity	Apollo/Lunokhod few cm accuracy
Parametrized Post-Newtonian (PPN)	$\lvert\beta - 1\rvert < 7.2 \cdot 10^{-5}$
Weak Equivalence Principle (WEP)	$\lvert\Delta a/a\rvert < 2.4 \cdot 10^{-14}$
Strong Equivalence Principle (SEP)	$\lvert\eta\rvert < 3.4 \cdot 10^{-4}$
Time Variation Gravitational Constant	$\lvert\dot{G}/G\rvert < 9.5 \cdot 10^{-15} yr^{-1}$
Inverse-Square Law	$\alpha < 3 \cdot 10^{-11}$
Geodetic Precession	$\lvert K_{GP}\rvert < 6.4 \cdot 10^{-3}$

Table 4.1: Current limits on precision tests of General Relativity [30].

Both Tables 4.1 and 4.2 are products of the PEP software by SCF_Lab.

Test of General Relativity	mm accuracy	0.1 mm accuracy
Parametrized Post-Newtonian (PPN)	10^{-5}	10^{-6}
Weak Equivalence Principle (WEP)	10^{-14}	10^{-15}
Strong Equivalence Principle (SEP)	$3 \cdot 10^{-5}$	$3 \cdot 10^{-6}$
Time Variation Gravitational Constant	$5 \cdot 10^{-15}$	$1 \cdot 10^{-15}$
Inverse-Square Law	10^{-12}	10^{-13}
Geodetic Precession	$6 \cdot 10^{-4}$	$6 \cdot 10^{-5}$

Table 4.2: Future improvements achievable of GR tests with MoonLIGHT [30].

It is easy to notice that through the data derived from MoonLIGHT, the parameters of fundamental physics shall improve by one order of magnitude, and after several years of measurements, till to two orders of magnitude.

CHAPTER 5

LARES-2

LARES-2 is a passive spherical satellite with a diameter of about $42cm$ and a mass of $395kg$, obtained from a single, high-density block of nickel alloy (Inconel 718). LARES-2 is covered by 303 CCRs uncoated, each one with a diameter of 1 inch ($2.54cm$).

The innovation of this new satellite is the use of retroreflectors Commercial Off-The-Shelf (COTS).

COTS products have the advantages of being ready-made and available; moreover, they have a lower cost with a shorter procurement time. Being commercial products, some features can not be accurate and precise, as Dihedral Angle Offset (DAO). The SCF_Lab is a facility specialized in the characterization of the optical performances of any retroreflector and, by performing a detailed statistical analysis over a large sample of CCRs, is able to choose the best products and, at the same time, reducing costs.

All steps and tests done for the construction of the satellite are described in the following sections.

5.1 Incoming Inspection

After the delivery of the CCRs, the first step was the incoming inspection performed in the SCF_Lab. The CCRs to analyze was 640; for each one of these, an arbitrary and progressively increasing serial number was assigned

(Fig. 5.1(a)). The serial number is the following:

- **L2**: indicates LARES-2 Project;
- **FM**: indicates the Flight Model quality of the optics;
- **CCR**;
- **001** up to **640** is the CCR specific serial number.

After the unpacking of each CCR, a visual inspection was performed, which confirmed the physical integrity of the retroreflector (Fig. 5.1(b)).

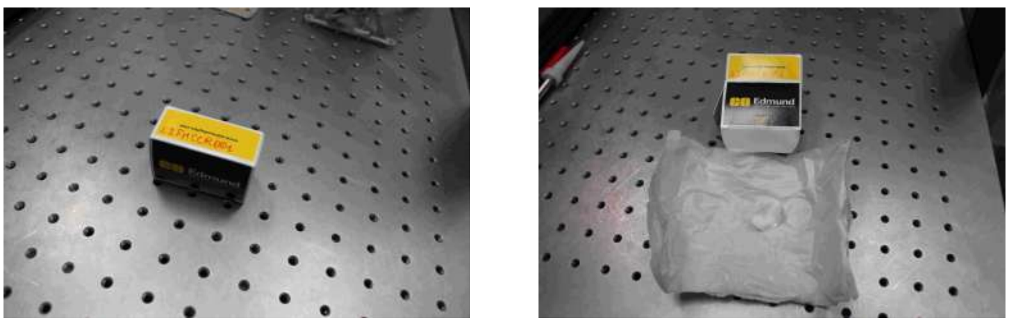

(a) CCR inside vendor case. (b) Naked CCR.

Figure 5.1: An example of visual inspection of CCR number 001.

After that, the laser return intensity distribution was measured at $532nm$ for all CCRs, as it would be measured on the ground by laser ranging devices aiming at an actual target. The measurements were performed for all the three 'edge up' configurations, since the patterns of the three edges of each CCR often have different intensities.

The optical bench of SCF_Lab is designed to separate the horizontal and vertical components of polarization of each FFDP. As already described in section 1.2, for uncoated CCR a strong dependency of the orientation of the input linear polarization is expected, while for coated CCR there is no dependency.

Moreover, the optical bench of the SCF_Lab is equipped with the Wavefront Fizeau Interferometer (WFI). Also the interferograms are acquired during the incoming inspection.

Figure 5.2: Calibration of the indicator with the Johansson gauges; the indicator is fixed to zero with 18mm.

Since the COTS retroreflectors could not be precise in several features, also in the heights of the CCRs, it is necessary to measure it. In order to do this measurement, an indicator is used. The nominal height of one CCR of 1 inch (2.54cm of front face diameter) is 19.05mm: for each of the 640 retroreflectors, a tip-to-face measurement is performed, to identify possible Out of Tolerance (OoT) case. To understand the deviation from its nominal height, the indicator was calibrated to zero with a height of 18mm (Fig. 5.2), given by the use of Johansson gauges, for producing precision lengths.

After the indicator calibration, each CCR tip-to-face was measured. In the Figures 5.3 it is possible to appreciate better the deviation of the calibrated height of the CCRs.

(a) CCR n. 230: its height is 18.96mm.

(b) CCR n. 237: its height is 19.10mm.

Figure 5.3: An example of two tip-to-face measurements with CCRs number 230 and 237.

5.2 Far Field Diffraction Pattern

In order to proceed with the FFDP analysis, it is necessary to explain some base concepts. First of all, in optics, the far field diffraction pattern is a form of wave diffraction, visible when field waves are passed through a slit or an aperture. For CCR FFDP, the aperture could be approximated to a circular one. The pattern of diffraction of a circle, as the case of flat mirror, is the Airy pattern, with rings of decreasing brightness (Fig. 5.4).

However, the FFDP of a CCR is different from the flat mirror one, due to its geometrical features. An idea of the shape of this pattern is shown in Figures 5.5.

The pattern shows a central peak, in which is concentrated most of the reflected energy, with smaller spots of less intensity.

For each 640 CCRs, it has been acquired the diffraction pattern (for

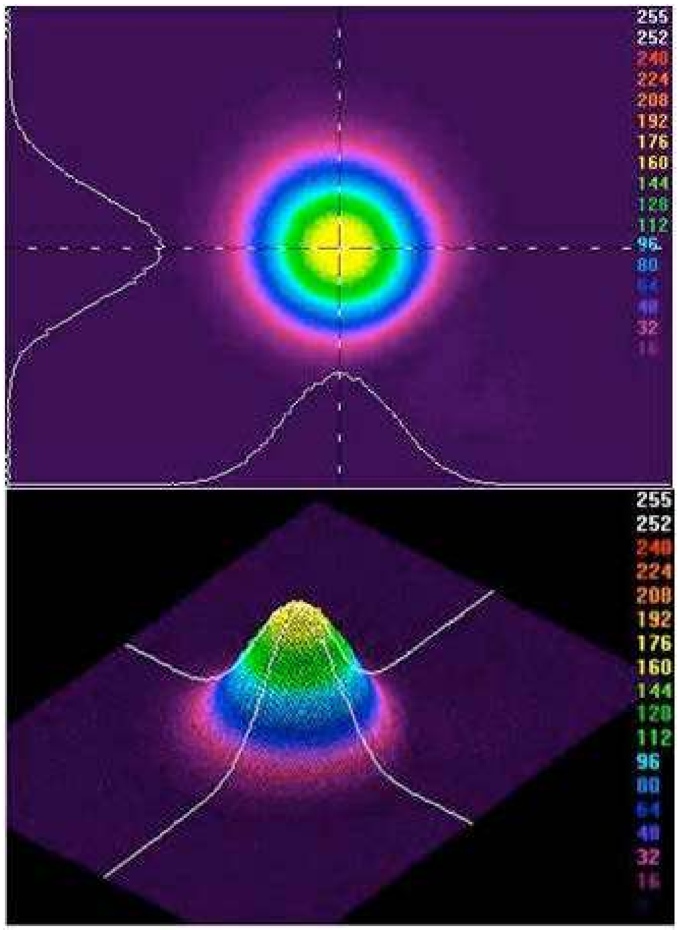

Figure 5.4: The Airy pattern: typical diffraction pattern of a flat mirror.

each CCR, three edge up configurations are acquired); and in particular, the vertical and horizontal component separately (Fig. 5.5(b) and Fig. 5.5(c)), due to the uncoated feature of retroreflector. Indeed, in the uncoated CCR case, polarization affects the shape of the pattern.

What happens in the laboratory is actually an ideal case: it is a perfect return laser of one CCR. In the reality, there is a problem to take into account. Laser ranging between retroreflector and ground station simulated in laboratory could be perfectly compatible with the real case only if the satellite and Earth positions were completely fixed. What actually happens is very different from what happens in our laboratory, because the Earth and

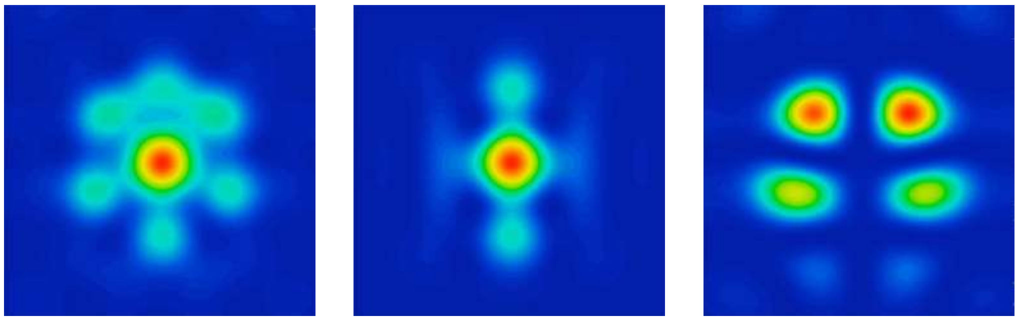

(a) Total pattern (b) Horizontal component (c) Vertical component

Figure 5.5: An example of diffraction pattern of an uncoated CCR.

satellites move. To take this phenomenon into account, a new concept is introduced, called Velocity Aberration (VA).

The VA is referred to the relative motion of the CCRs on the satellite (Moon or artificial) respect to the Earth. Considering a beam of light directed to the retroreflector, it will be returned along the same line because of the CCR property. However, this mechanism is true only if both satellite and Earth are in stationary position; there is a difference in velocity between the position of the starting laser and the retroreflector, and it is possible to lost the return laser, as explained in the Figure 5.6.

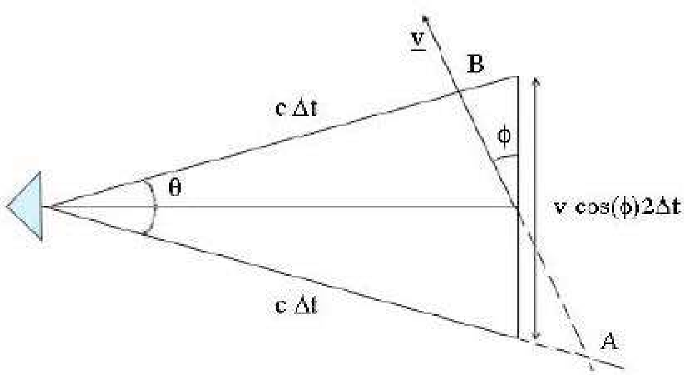

Figure 5.6: Velocity Aberration (VA) scheme: emitted pulse of light starts from point A returns to the same point after $2\Delta t$, when the transmitter is in the point B.

The emitted pulse of light starts at point A and travels to a CCR at velocity c in time Δt. After $2\Delta t$ the laser returns to point A, but at this time the transmitter will be in point B, due its velocity v, with an angle ϕ respect to the line normal to the line of sight (Fig. 5.6).

Assuming $\theta \ll 1$:

$$c \cdot \Delta t \cdot \theta \cong v \cdot \cos(\phi) \cdot 2\Delta t \tag{5.1}$$

$$\rightarrow \theta = 2\frac{v}{c}\cos(\phi) \tag{5.2}$$

in which:

- v is the relative velocity between retroreflector and Earth;
- θ is the velocity aberration.

The velocity aberration θ must be at least equal to value expressed in Eq. 5.2, to be able to receive the reflected light in point B. The value of VA is fundamental to understand if and in which place the reflected laser will reach the ground station.

The VA for LARES-2 satellite is $(35 \pm 2)\mu rad$ (while for the Moon is around $4\mu rad$).

After the diffraction pattern acquisitions, it is possible to process data through a MatLab script. This software extracts the total FFDP, the average intensity in function of the VA and the CCR intensity at a determined VA. An example of these plots are shown in Figure 5.7, Figure 5.8 and Figure 5.9.

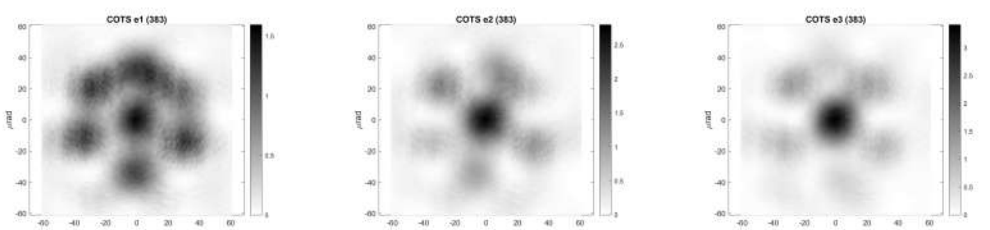

(a) Edge 1 of CCR n.383. (b) Edge 2 of CCR n.383. (c) Edge 3 of CCR n.383.

Figure 5.7: FFDP of the CCR n.383 for each edge-up configuration.

In Figure 5.7, there are three different FFDPs reported for the three edge up configurations.

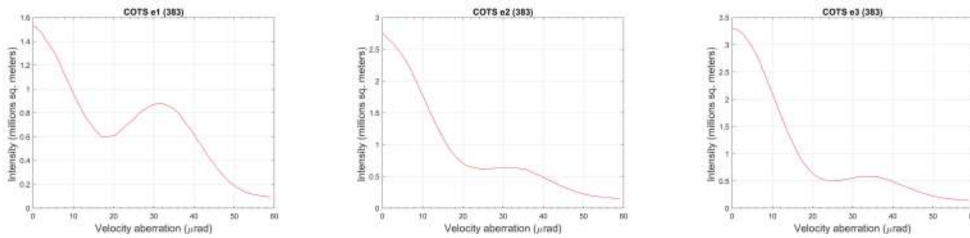

(a) Edge 1 of CCR n.383. (b) Edge 2 of CCR n.383. (c) Edge 3 of CCR n.383.

Figure 5.8: Intensity of the CCR n.383 for each edge-up configuration in function of VA.

In Figure 5.8, the CCR intensity is shown in function of the VA. The intensity is an intrinsic characteristic of CCR; this value describes the maximum amount of flux reflected back to the source, or in other words, the distribution of photons, and its unit of measure is million square meter. This quantity is conventionally called Optical Cross Section (OCS).

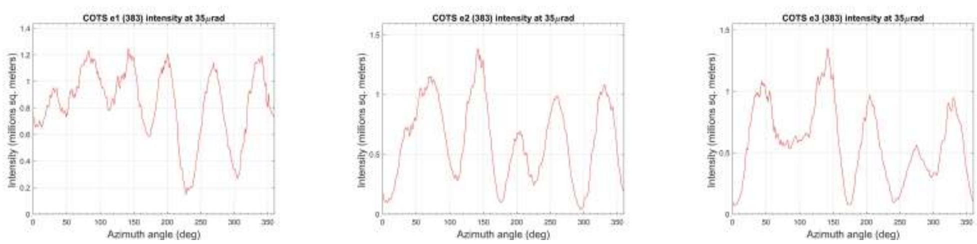

(a) Edge 1 of CCR n.383. (b) Edge 2 of CCR n.383. (c) Edge 3 of CCR n.383.

Figure 5.9: Intensity of the CCR n.383 for each edge-up configuration in function of the Azimuth Angle at a VA of $35\mu rad$ proper of LARES-2.

In Figure 5.9, the CCR intensity is plotted in function of the Azimuth Angle at a Velocity Aberration (VA) equal to that LARES-2, i.e. $(35 \pm 2)\mu rad$.

Due to the great amount of data, the optics analysis has been divided into Batches to be analyzed. For each edge up configuration, the distribution of the CCR average intensity at $(35 \pm 2)\mu rad$ is plotted and, from these, the arithmetic average value over the three edge is computed. In the Table 5.1, the values are listed in comparison with the theoretical value simulated. In the Figure 5.10, there is the distribution of the OCS at LARES-2 VA of the whole sample of 640 CCRs. The mean value of the distribution is $0.59 \cdot 10^6 m^2$ and the standard deviation is $0.07 \cdot 10^6 m^2$.

Number of CCR	OCS $[10^6 m^2]$
Batch1 (1-100)	(0.59 ± 0.06)
Batch2 (101-200)	(0.62 ± 0.05)
Batch3 (201-320)	(0.56 ± 0.05)
Batch4 (321-420)	(0.61 ± 0.14)
Batch5 (421-520)	(0.57 ± 0.07)
Batch6 (521-640)	(0.57 ± 0.08)
Theoretical value	0.75

Table 5.1: The arithmetic average Intensity value for each Batch and theoretical value simulated.

Nevertheless the values are smaller than the simulated value. These results confirm the expected lower optical quality of the hardware, being component-off-the-shelf with respect to custom CCRs.

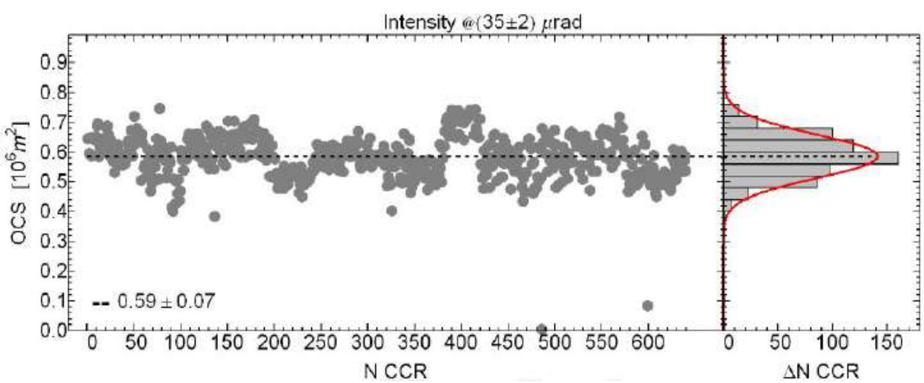

Figure 5.10: The OCS at LARES-2 VA (averaged on the three edge-up configurations) of the whole sample of 640 CCRs. The mean value of the distribution is $0.59 \cdot 10^6 m^2$ *and the standard deviation is* $0.07 \cdot 10^6 m^2$.

5.3 Interferograms

Interferograms were acquired and then analysed by using the proprietary interferometric software distributed by 4D Techs Inc. For each CCR, three interferograms were acquired, one for each of its three edge-up configurations (Fig. 5.11).

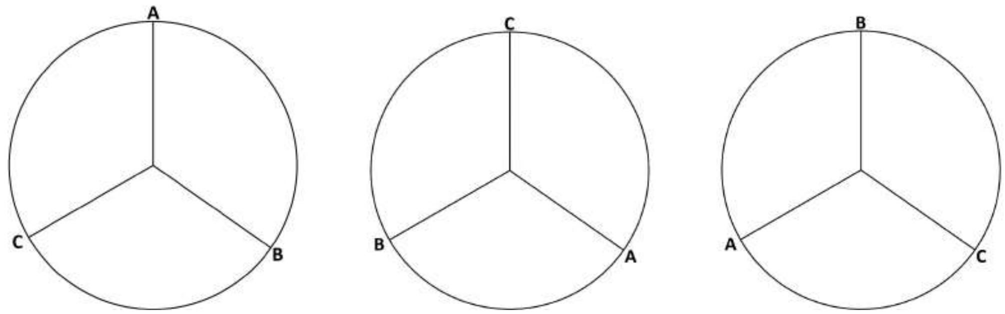

(a) Edge 1 of CCR. (b) Edge 2 of CCR. (c) Edge 3 of CCR.

Figure 5.11: Three edge-up configurations during the optical and interferometric measurement of a given CCR.

In the interferogram measurements, if the cube corner angles are exactly 90° without any error, they reflect an incident plane wavefront as a single emerging plane wavefront. Instead in the case of errors in the manufacturing of the CCRs, the reflected wavefront is the sum of several plane wavefronts with different tilts: in this way it is possible to measure the error.

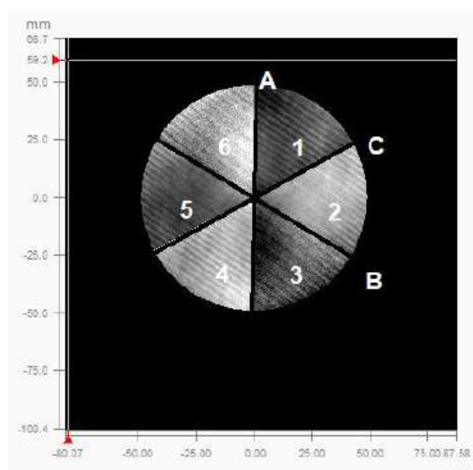

Figure 5.12: Software view of one interferogram: it is easy to notice the islands of measurements.

In order to perform the cube corner analysis, measurements must first be separated into six islands (Fig. 5.12). The islands are practically a mask, which defines the regions from which data should be kept and analyzed. It is possible to analyze and extract for each interferograms the following features of the CCR with the WFI software (4Sight):

- Dihedral Angle Offset (DAO): physical deviation of the retroreflector from a perfect angle (90°) between faces. DAO measurements are in arcseconds.
- Peak to Valley (PV): The peak-to-valley height difference within each individual island.
- Root Mean Square (RMS): The root-mean-square roughness for each island.

The fundamental feature for our tests is DAOs. This measurement is given by [52]:

$$\epsilon = \frac{\alpha}{4mn\sin(\theta)} \tag{5.3}$$

where:

- α is the beam deviation;
- θ is the angle between the roof edge and the incident beam;
- m is the number of passes, depending on the interferometer configuration: it can be single pass or double pass (the single pass is the configuration of our interferometer);
- n is the index of refraction.

The sign of DAO could be positive, if it is larger than 90°, or negative, if it is smaller than 90°. The manufacturer information estimates the angle error as: 0.0 ± 0.64 *arcseconds*.

After acquiring interferometer data, software extracts the following data (Table 5.2, 5.3, 5.4) for each CCR:

Edge	DAO	Sum
1	0.12	
2	-0.07	0.05
3	0.00	

Table 5.2: Example of CCR num. 1 data derived after interferometer analysis: DAO for each edge.

Peak-to-Valley			
Edge 1	Edge 2	Edge 3	Mean
0.32	0.17	0.16	
0.37	0.36	0.39	
0.63	0.62	0.35	0.36
0.43	0.18	0.15	
0.31	0.29	0.26	
0.61	0.52	0.36	

Table 5.3: Example of CCR num. 1 data derived after interferometer analysis: PV for each edge. Each line shows the measurements corresponding to each island.

After the analysis of each interferograms, the DAOs are plotted in six different histograms for each CCRs batch (Figures 5.13). The Batch 1 is referred to CCRs number 001 to 100. The Batch 2 is referred to CCRs number 101 to 200. The Batch 3 is referred to CCRs number 201 to 320. The Batch 4 is referred to CCRs number 321 to 420. The Batch 5 is referred to CCRs number 421 to 520. The Batch 6 is referred to CCRs number 521 to 640.

The measured DAOs have been fitted with a Gaussian distribution. The best-fit value for each Batch is reported in the table 5.5.

The best values are within the declared one by the manufacturer. Each DAOs data is plotted in a new histogram (Fig. 5.14), as measured from the whole sample of 640 CCRs. The best-fit value is (0.01 ± 0.10) arcsec.

RMS

Edge 1	Edge 2	Edge 3	Mean
0.02	0.02	0.03	
0.03	0.03	0.03	
0.04	0.04	0.03	0.03
0.02	0.02	0.03	
0.03	0.03	0.03	
0.05	0.04	0.04	

Table 5.4: Example of CCR num. 1 data derived after interferometer analysis: RMS for each edge. Each line shows the measurements corresponding to each island.

Batch 1	(-0.01 ± 0.11) arcsec
Batch 2	(-0.02 ± 0.13) arcsec
Batch 3	(0.01 ± 0.09) arcsec
Batch 4	(0.01 ± 0.08) arcsec
Batch 5	(0.01 ± 0.09) arcsec
Batch 6	(0.01 ± 0.08) arcsec

Table 5.5: Best fit of Gaussian distributions of DAOs for each Batch.

5.4 SCF-Test on BreadBoard

In order to do tests, two equal BreadBoards (BBs) have been produced. The first one has been used for the vibration and shock tests, and the second one to perform a space environment laser return test.

Each BB consists of a cylinder of Inconel 718, with a mass of about $1700g$ and reproduces four cavities of the satellite (Fig. 5.15).

The SCF-Test aims to characterize the optical response and thermal behaviour of each CCR of the BB in simulated space conditions. The optical responses are tested by measuring FFDPs; thermal behaviour by thermal relaxation constant τ_{CCR}.

The SCF-Test should verify that the average intensity remains constant during the test with respect to the initial condition (air condition). To perform tests and collect data, the BB is assembled on the SCF-G facility and is equipped with three PT100 sensors to measure the temperature of the CCRs housing in different positions. In this way, the payload could be exposed to

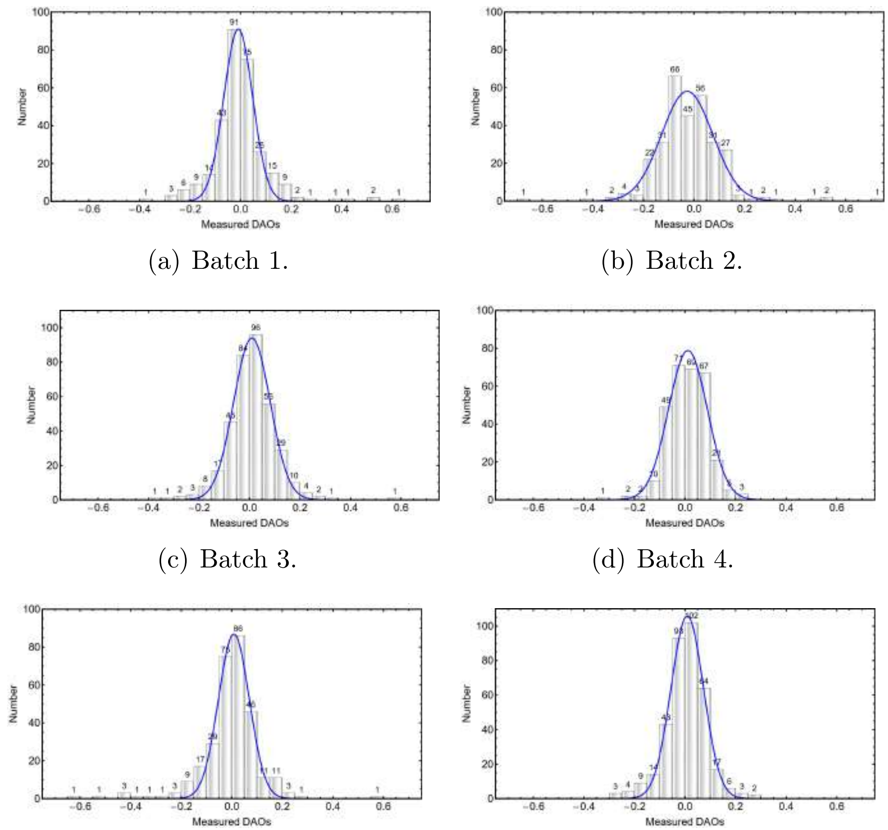

(a) Batch 1. (b) Batch 2.

(c) Batch 3. (d) Batch 4.

(e) Batch 5. (f) Batch 6.

Figure 5.13: The distribution of all DAOs for each Batch. The blue line is the Gaussian fit of the data.

the Solar Simulator (SS), to simulate the solar radiation on the BB, and to the SCF-G optical window for laser interrogation.

The SCF-Test has been performed twice: first of all, maintaining the SS beam orthogonal to BB, thus with an incidence angle of 0°; and with SS incidence angle equal to 31°. The latter case derives from the breakthrough, i.e. TIR is broken and light rays pass through the CCR, heating the surface of the housing.

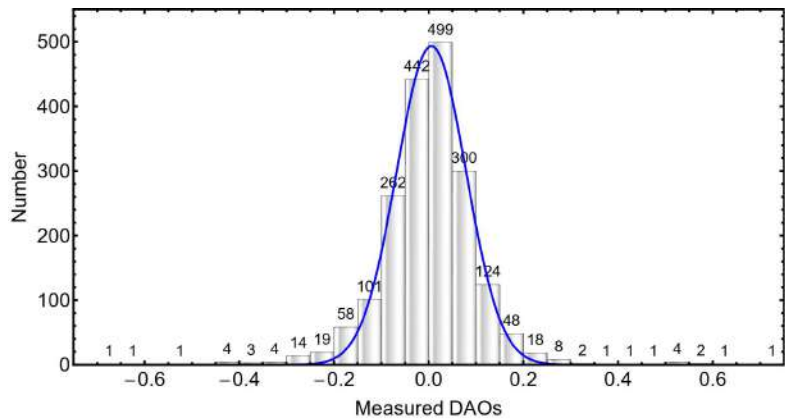

Figure 5.14: The distribution of all DAOs values of the whole sample of 640 CCRs. The blue line is the Gaussian fit of the data.

The SCF-Test follows the steps below:

1. Records FFDP for each CCR, one by one, in air conditions;
2. Records FFDP for each CCR, one by one, in vacuum conditions (temperature $= 110 \pm 10K$ and pressure $= 10^{-5}mbar$);
3. Records FFDP for each CCR, one by one, at reference temperature equal to $300K$;
4. SS on: BB illuminated at incidence equal to 0°;
5. SS off after 1.5 hour;
6. Records FFDP for each CCR, one by one; during the first half-hour records every 2 minutes, then during the second half-hour records every 5 minutes, and finally the third half-hour every 10 minutes (Total duration of acquisition: 1.5 hour).
7. Records thermograms acquisition every 10s (total duration: 3 hours);
8. Records FFDP for each CCR, one by one, at reference temperature equal to $280K$; steps repetition from point 4 to 7.
9. Records FFDP for each CCR, one by one, at reference temperature equal to $320K$; steps repetition from point 4 to 7.

(a) (b)

Figure 5.15: One of two equal BB useful to perform vibration test and SCF-Test.

10. Records FFDP for each CCR, one by one, at reference temperature equal to $300K$;

11. SS on: BB illuminated at incidence equal to 31°;

12. SS off after 1.5 hour;

13. Records FFDP for each CCR, one by one; during the first half-hour records every 2 minutes, then during the second half-hour records every 5 minutes, and finally the third half-hour every 10 minutes (Total duration of acquisition: 1.5 hour).

14. Records thermograms acquisition every 10s (total duration: 3 hours);

15. Records FFDP for each CCR, one by one, at reference temperature equal to $280K$; steps repetition from point 11 to 14.

16. Records FFDP for each CCR, one by one, at reference temperature equal to $320K$; steps repetition from point 11 to 14.

17. Increase temperature to ambient one and break the vacuum by air entry;

18. Temperature stabilization;

19. End of the test.

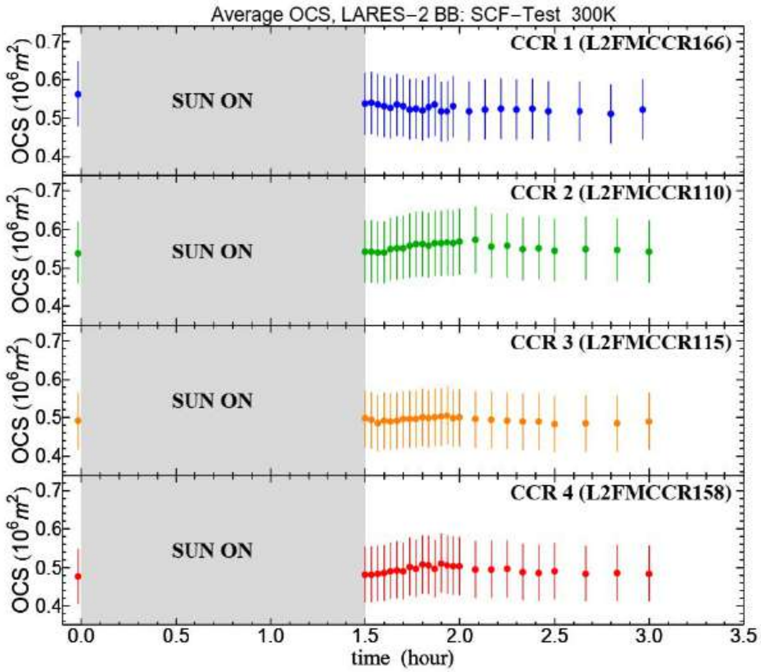

Figure 5.16: OCS at $35\mu rad$ of each CCR during the test at $Tc = 300K$ and SS incidence at $0°$. The shades gray area indicates the duration of the SS on, when the BB is rotated toward the SS and no pattern can be acquired.

The results of the SCF-Test include the evolution of the average intensity, or OCS, at VA equal to $35\mu rad$ of each CCR of BB at different temperatures. The Figure 5.16 shows the evolution of the OCS with SS incidence angle of $0°$ at $T = 300K$. In the Appendix A, the Figures A.1 and A.2 show the evolution at temperatures $T = 280K$,and $T = 320K$.

The Figure 5.17 shows the evolution of the average intensity with SS incidence angle of $31°$ $T = 300K$. In the Appendix A, the Figures A.3 and A.4 show the evolution at temperatures $T = 280K$,and $T = 320K$.

From the optical performances point of view, all the SCF-Tests, at $0°$ and $31°$, and $T = 280K$, $T = 300K$ and $T = 320K$, have shown that the average intensity of the CCRs at the LARES-2 VA remains constant in all conditions.

During the SCF-Test, the thermal analysis has also been performed. The temperature of each CCR varies depending on the degree of thermal insulation of the retroreflector with respect to the BB frame and on the amount

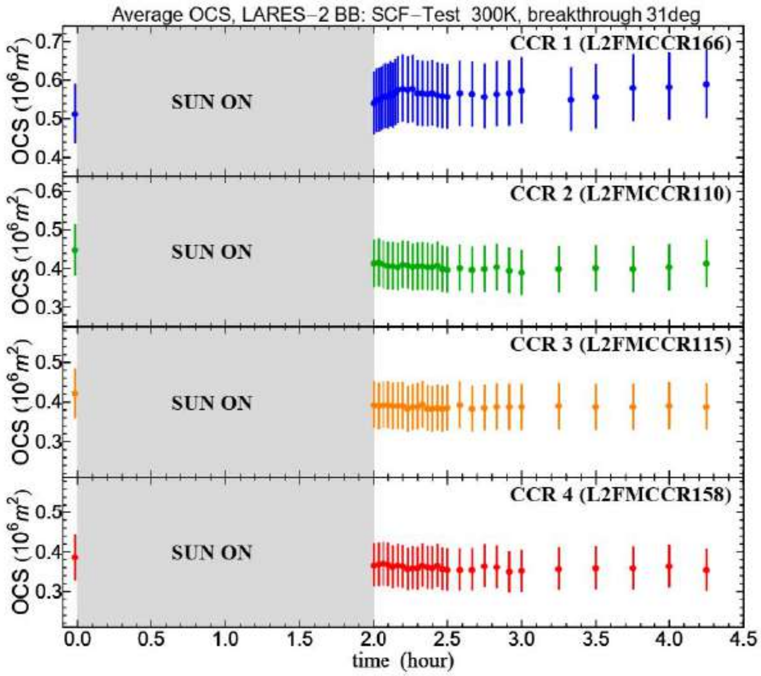

Figure 5.17: OCS at $35\mu rad$ of each CCR during the test at $Tc = 300K$ and SS incidence at $31°$. The shades gray area indicates the duration of the SS on, when the BB is rotated toward the SS and no pattern can be acquired.

of radiative heat transfer. Non-invasive temperature measurements of each CCR have been obtained by means of IR thermography. With this information, it is possible to study the thermal behaviour of one retroreflector, described by the thermal relaxation time (τ_{CCR}). The τ_{CCR} is the characteristic heating or cooling time, defined by the Newton's law of heating/cooling:

$$T_1 = T_0 \pm \Delta T(1 - e^{-t/\tau_{CCR}}) \tag{5.4}$$

where T_0 is the initial temperature at first thermogram, ΔT is the difference between the final (assuming a plateau) and initial temperature. Positive sign is used for the heating phase and the negative one for the cooling. Data taken with the IR camera can be fitted exponentially, in order to extract τ_{CCR}.

Heating and cooling curves for each CCR at $T = 300K$ is shown in Figure 5.18. During the SS on phase, CCRs show an increase in temperature of about $4.9K$. During the SS off phase, the temperature decrease is of the

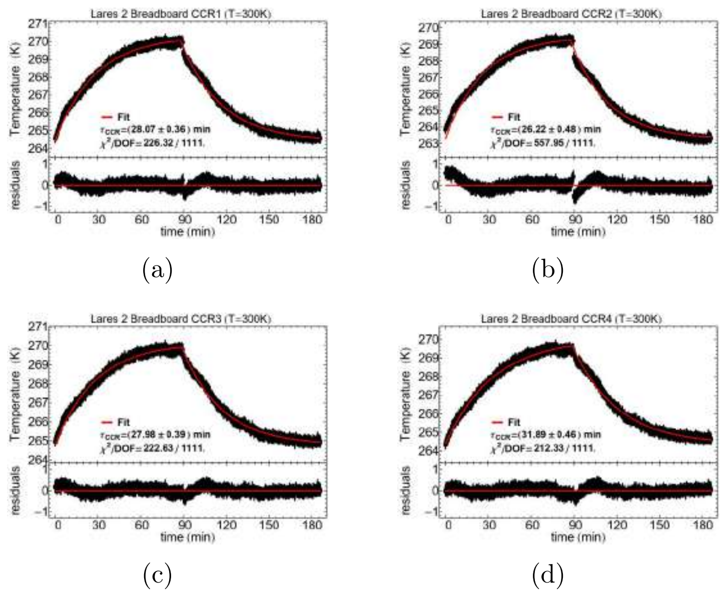

Figure 5.18: Thermal analysis for each CCR, with SS incidence angle of $0°$ *at* $T = 300K$.

same order. In Appendix A, Figures A.5 and A.6 show the same curves at $t = 280K$ and $T = 320K$ respectively.

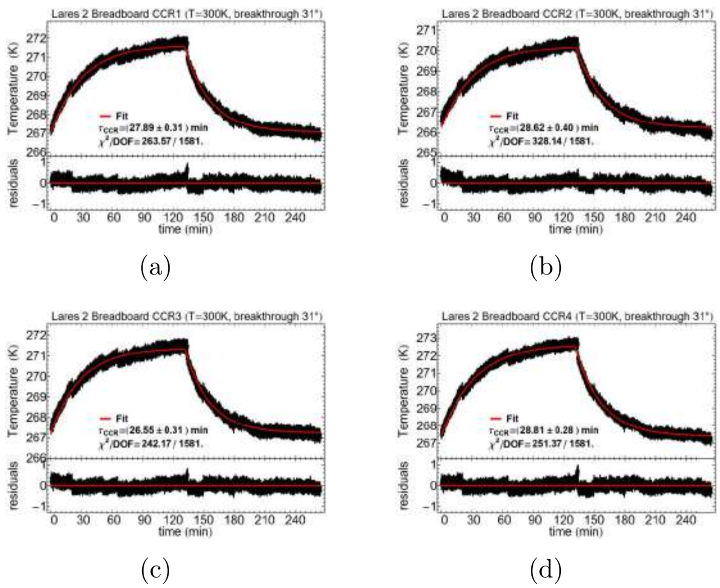

Figure 5.19: Thermal analysis for each CCR, with SS incidence angle of $31°$ *at* $T = 300K$.

The thermal relaxation time with SS incidence angle of 0° for each temperature is listed in Table 5.6.

τ_{CCR}	Value [min] at 280K	Value [min] at 300K	Value [min] at 320K
CCR 1	31.56 ± 0.64	28.07 ± 0.36	30.55 ± 0.38
CCR 2	29.25 ± 0.62	26.22 ± 0.48	28.18 ± 0.31
CCR 3	32.36 ± 0.69	27.98 ± 0.39	28.66 ± 0.36
CCR 4	35.39 ± 0.63	31.89 ± 0.46	35.29 ± 0.73

Table 5.6: Values of τ_{CCR} *with SS incidence angle of* $0°$*, for each temperature.*

In the same way, the Figure 5.19 shows the heating and cooling curves for each CCR with the SS incidence angle at 31°, i.e. the breakthrough condition. During the SS on phase, CCRs show an increase in temperature of about $4.1K$; and during the SS off phase, the temperature decrease is of the same order. In the Appendix A, Figures A.7 and A.8 show the same curves at $t = 280K$ and $T = 320K$ respectively.

The thermal relaxation time with SS incidence angle of 31° for each temperature is listed in Table 5.7.

τ_{CCR}	Value [min] at 280K	Value [min] at 300K	Value [min] at 320K
CCR 1	36.63 ± 1.09	27.89 ± 0.31	28.22 ± 0.42
CCR 2	34.91 ± 1.14	28.62 ± 0.40	28.16 ± 0.46
CCR 3	33.09 ± 0.87	26.55 ± 0.31	24.22 ± 0.36
CCR 4	37.58 ± 0.69	28.81 ± 0.28	29.21 ± 0.34

Table 5.7: Values of τ_{CCR} with SS incidence angle of 31°, i.e. breakthrough condition, for each temperature.

The relaxation constant in all the SCF-Tests is about $30min$, indicating that all CCRs respond quickly to the changes of the thermal conditions.

5.5 Integration onto satellite

The last step of this experiment was the real integration of the retroreflectors onto satellite. While the manufacturing of the Proto Flight Model (PFM) has been performed in the INFN of Padova (Fig. 5.20), the cleaning of the sphere and the consequently integration of CCRs have been performed in the INFN of Frascati, and in particular in the SCF_Lab.

(a) Sphere before milling at INFN-PD.

(b) Sphere on the milling facility in INFN-PD.

Figure 5.20: PFM of LARES-2 during manufacturing in INFN-PD.

As already described, LARES-2 is a satellite covered by 303 retroreflectors. Thus, 303 CCRs have been selected to be integrate on the PFM. The selection is a consequence of the optical, mass and dimensional measurements.

First of all, from the whole sample of 640 CCRs, 13 of these are excluded, and in particular: 4 CCRs used for vibration tests on BB, 8 CCRs already integrated on the demonstration model, and 1 cracked.

From the 627 retroreflectors available, retroreflectors with an OCS too low, and in particular $< 0.4 \cdot 10^6 m^2$ were excluded (Fig 5.21).

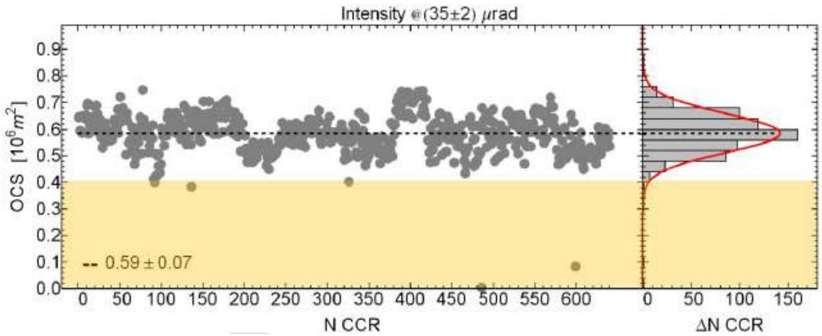

Figure 5.21: The OCS, averaged on the three edge-up configurations, at VA of LARES-2 of the whole sample of 640 CCRs. The yellow area shows the CCRs excluded based on the OCS value.

The integration on the satellite occurs with a determinate CCR packs, shown in Figure 5.22. Here, there is a schematic representation of one typical CCR pack: from bottom to the top, the CCR cavity, lower plastic ring, CCR, middle metallic ring, upper plastic ring, retainer metallic ring and three screws. In particular, middle metallic ring has three different possible thickness: small, nominal and large, based on the size of the retroreflector. Moreover CCRs with OoT tip-to-face heights were excluded.

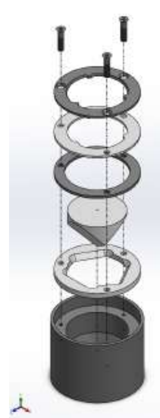

Figure 5.22: The CCR pack: from bottom to the top, the CCR cavity, lower plastic ring, CCR, middle metallic ring, upper plastic ring, retainer metallic ring and three screws.

In the Table 5.8, there are the limit to distinguish the OoT, small, nominal and large size. In the Figure 5.23 there is the distribution of the CCRs, based on the tip-to-face measurements.

CCR tip-to-face [mm]	Middle ring type
<18.9225	Low OoT
18.925-19.007	Small
19.008-19.091	Middle
19.092-19.171	Large
>19.171	High OoT

Table 5.8: The range of CCR tip-to-face heights in mm and the associated middle ring type.

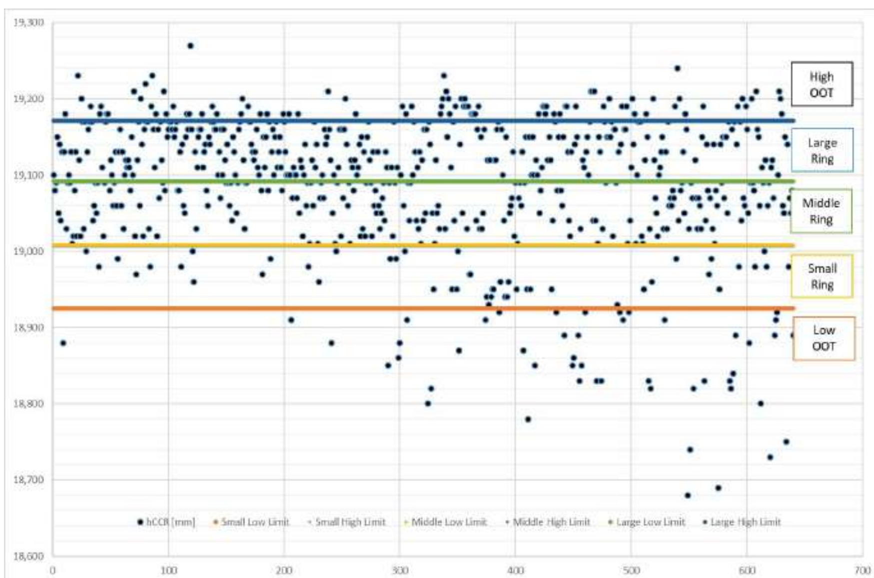

Figure 5.23: Tip-to-face height distribution of the whole sample of 640 CCRs. The objects in the OoT ranges are excluded.

Finally, after the selection derived from the low OCS and the size of the CCR, the final sample of available CCRs drops to 489 retroreflectors.

The last step was to choose 303 CCRs to integrate onto satellite, from the 489 CCRs available. The coverage of the entire sphere must follow a scheme, that is the result of the compromise between an OCS and mass distributed evenly.

To analyze the laser return properties of LARES-2, it has been performed a simulation of the laser return from different, partially-overlapping angular views, interrogated by an expanded laser beam of the same size of that of the SCF-G optical bench. In order to coverage the entire surface, it is necessary to set two different ranges of rotation: $0° \le \theta \le 360°$ and $0° \le \phi \le 180°$, where the two angles θ and ϕ are orthogonal to laser beam. Considering a laser beam coverage of about 30°, the number of views to cover the satellite is: $360°/30° \cdot 180°/30° = 72$ views, which are obviously partially-overlapping.

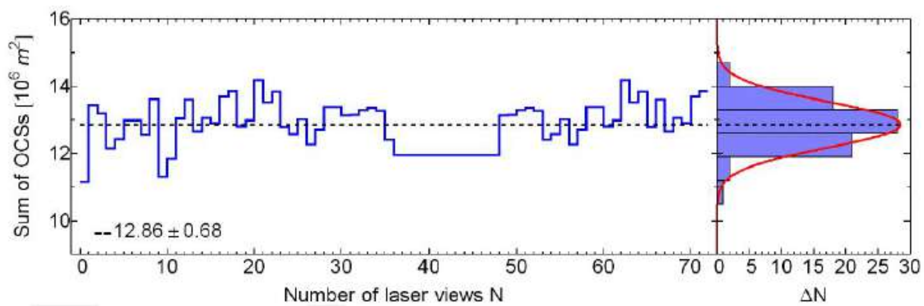

(a) The sum of OCS of each CCR falling inside the laser beam for each 72 views. The mean value is $12.86 \cdot 10^6 m^2$ and the standard deviation is $0.68 \cdot 10^6 m^2$.

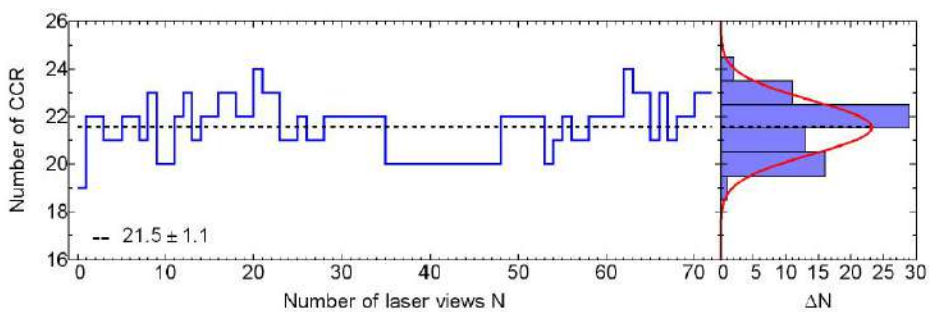

(b) The number of CCRs illuminated by the laser beam for each 72 views. The mean value inside the laser beam is 21.5 and the standard deviation is 1.1.

Figure 5.24: The sum of OCS and number of CCRs in function of the number of laser views.

Various options of 303 retroreflectors are elaborated by a specific software; then each option is analyzed. Here only the final configuration is reported. In particular, in the Figure 5.24(a), it is easy to notice that the sum of OCS of each CCR falling inside the laser beam is roughly constant at every orientation with a range of values $(11 \le OCS \le 13)10^6 m^2$. These values represent rough estimates obtained by assuming that the CCRs are assembled on a flat surface, whereas a more refined computation has to take into account the spherical symmetry of LARES-2. However, this simplification is made just to prove the uniformity of the OCS within each of the 72 simulated views. On the other hand, the Figure 5.24(b) show the number of CCRs illuminated by the laser beam for each of the 72 views. This number is in the range between 19 and 24.

Therefore, with this features the final configuration can be accepted and the integration has been carried out for a couple of months. The final result is in Figure 5.25.

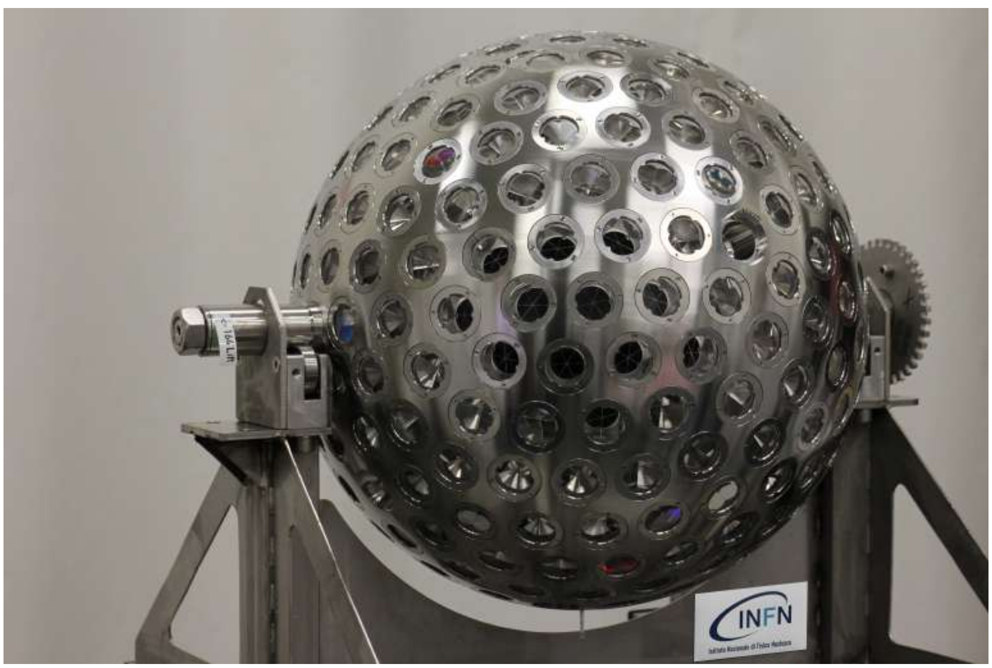

Figure 5.25: The final satellite LARES-2 with the CCRs integrated on it.

CHAPTER 6

MoonLIGHT Pointing Actuators

MoonLIGHT Pointing Actuators (MPAc) was designed for the alignment of a retroreflector in Azimuth and Elevation with respect to the Earth in the lunar environment. Unlike the Apollo CCR arrays, that were manually arranged by the astronauts, MPAc has been developed for the lunar environment to perform unmanned pointing operation of MoonLIGHT.

MPAc is a by-product of a space research activity started in 2006 at the National Institute of Nuclear Physics (INFN). In 2018, the INFN proposed to ESA MPAc project, which was evaluated among 135 eligible scientific projects proposals. In 2019, ESA chose MPAc, together with another instrument, ProSPA-lite by UK, for its future delivery to the Moon. Two years later, in 2021, ESA agreed with NASA to launch MPAc with Commercial Lunar Payload Services (CLPS) initiative, to the Reiner Gamma region, chosing Intuitive Machines (IM) as commercial lunar lander company.

6.1 Landing Site

The Reiner Gamma region on the lunar nearside has the coordinates 7.5°N and 59.0°W (Figure 6.1).

The particularity of this region lies in an unusual surface feature called "lunar swirl". Lunar swirls have a higher albedo than the surrounding lunar surface: in the Figure 6.2 it is easy to note the Reiner Gamma region on the

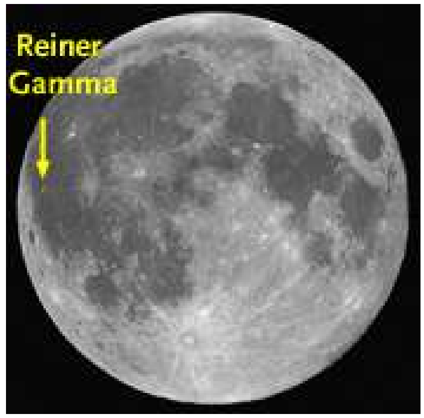

Figure 6.1: Reiner Gamma region on the Moon.

Figure 6.2: Reiner Gamma region (on the left) in comparison to Reiner impact crater (on the right). The latter has a diameter of 30 km and a depth of 2.6 km [9].

left.

After mapped the Lunar magnetic field from orbit, it was observed that lunar swirls are generally associated with a magnetic anomaly. But not all the magnetic anomalies can be associated with lunar swirls and albedo markings. The formation of the lunar swirls is still a mistery.

There are a large number of explanations for the lunar swirls: one of the most accredited theories is the mini-magnetosphere of the Moon which impedes space weathering by the solar wind. Mini-magnetospheres exhibit features that are characteristic of normal planetary magnetospheres, namely a collisionless shock. The electric field associated with the collisionless shock is responsible for deflecting the solar wind particles. These ions impacts on the lunar surface causing the albedo. The swirls patterns can be related to the shape of the collisionless shock [9].

Another theory consists in magnetically controlled dust transport. Swirls show distinctive spectral properties at both highland and mare locations that can be explained by fine-grained dust sorting. The sorting may result from two processes: the vertical electrostatic lofting of charged fine dust and the development of electrostatic potentials at magnetic anomalies that can attract or repel charged fine-grained dust that has been lofted. Since the finest fraction of the lunar soil is bright, the accumulation or removal of fine dust can change a surface's spectral properties [31].

Further theory explains the lunar swirls as a result of the cometary impact. In particular, cometary impacts produce combined effects: dragging of the finest fraction of lunar soil grains, production of large masses of vaporized material, and likely generation transient magnetic fields that could exceed the Earth's surface field strength by a factor of 104. This combination of processes is consistent with a mechanism to generate lunar swirls [14].

Finally, the last possibility regards the transport of secondary ions produced by micrometeorite or solar wind ion impacts. These ions may then be responsible for chemical alteration of the lunar surface from which derives the albedo or a interruption of space weathering processes [35].

6.2 The environment

In order to design a payload for a space mission, it is necessary to consider the effects of the space environment on an instrument. The following environment should be included:

- Magnetic field;
- Solar and Planetary Electromagnetic Radiation;
- Neutral Atmosphere;
- Plasmas;
- Energetic Particle Radiation;
- Particulates;
- Contamination.

Magnetic field

The magnetic field of the Earth influences the environment, deflecting low-energy cosmic ray and trapping the charged particles. The field is basically a dipole field, with the magnetic axis not coincident with the rotation axis. The strength of the magnetic field changes significantly on a scale of 5 to 10 years. Moreover, geomagnetic storms caused by solar activity can change the Earth magnetic field.

Solar and Planetary Electromagnetic Radiation

Regarding the electromagnetic radiation, in general each spacecraft receive this radiation from several external sources. The main source is the solar flux: the mean value of this flux is called "solar constant", even if this is no a real constant. Indeed the solar constant varies by about $3-4\%$ during each year due to the slightly elliptical orbit of the Earth around the sun: the maximum value occurs at the winter solstice, when the Earth-Sun distance is a minimum; vice versa, the minimum value occurs at the summer solstice because of the maximum Earth-Sun distance. Moreover, the energy emitted by the Sun varies according to the 11 year solar cycle. The values for the Earth distance shall also be used for the Moon. Typical values are listed in the table 6.1 [55].

Solar Flux $[W/m^2]$			
	Average	Minimum (summer solstice)	Maximum (winter solstice)
At the Earth	1366	1321	1413

Table 6.1: Typical values for solar flux.

The second source of radiation is the albedo, that is the incident sunlight reflected off a planet. This parameter measures the solar energy reflected back to space. For this reason, the albedo measure can be considered only when a portion of Earth seen by the spacecraft is sunlit. Albedo radiation has approximately the same spectral distribution as the sun, which approximates a blackbody with a temperature of $5780K$. It has a highly variability depending on surface properties and cloud cover: it is generally highest over the cloudy regions, deserts and snow and ice-covered areas, while is lowest over oceans if the sky is clear. Albedo also depends on the solar zenith angle: albedo increases as the solar zenith angle increases.

Another fraction of radiation is the planet infrared radiation. The Earth-emitted thermal radiation, also called Earth infrared or Outgoing Long-wave Radiation, has a spectrum of a blackbody with a temperature of $288K$. The Earth infrared radiation shows some variations: based on the temperature, a warmer region emits more radiation than a colder area; increasing the cloud cover, the radiation is lower; because of the seasonal variations. Also a diurnal variation can be detected, however it is small over the ocean but can amount to 20 % for desert areas.

Further sources of radiation are due to the Moon: the lunar albedo and lunar infrared. The average albedo of the Moon is about 0.12; however, the albedo varies from about 0.06 up to about 0.30. The lunar infrared radiation emitted occurs some variations, such as the low albedo, the lack of atmosphere and the low effective conduction of the regolith. The flux varies from the maximum value of $1330W/m^2$ to $5W/m^2$ [56].

Neutral Atmosphere

The neutral atmosphere extends from the surface to 2500 km altitude or more, but an outer limit is not rigorously defined. The neutral atmosphere is significant for space vehicle operations: it produces torques and drags on the vehicle, even at its low density; the flux of trapped radiation and the orbital debris is modulated by the density height profile of the atmosphere; and the atomic oxygen changes and erodes the surfaces exposed to it.

Plasmas

A spacecraft in Earth orbit encounters some distinct plasma regimes: the ionosphere, the plasmasphere, the outer magnetosphere and the solar wind.

The ionosphere is the upper part of the atmosphere, made of ionised plasma due to the dissociation of the atmospheric atoms because of the sunlight. Important features of the ionosphere is the reflection of radio beams below a critical frequency; indeed it is like a barrier to satellite and ground communication.

The plasmasphere is a cold dense plasma region; it is originated in the ionosphere. This region contributes to the radio propagation problems; however the minor densities produce a not large effect.

The magnetosphere is characterized by high temperatures and low densities plasma. It drifts sunwards from the tail to the near-Earth region, thanks to the cross-tail electric field. The electrons of this region can accumulate on exposed spacecraft surfaces producing a current. Knowing this problem, opposite currents exist preventing significant charging levels; but if these are not sufficient, the spacecraft surface may charge to hundreds or thousands of volts.

The solar wind is the outer atmosphere of the Sun. It starts at the Sun as a hot dense and slowly moving plasma but accelerates outwards becoming cool, rare and supersonic near Mercury and beyond. The solar wind is composed mostly by protons (95%), alpha particles (4%) and minor ions (1%), like carbon, nitrogen etc. Because of the solar wind, the energy putted in the magnetosphere increases and causes the surface charging and radiation effects.

Energetic Particle Radiation

The most dangerous aspect of the space environment is the energetic particle radiation, composed of magnetically trapped charged particles, solar protons and galactic cosmic rays. The problems caused by these charged particles include damage of electronic components or solar cells, payload interference, dielectric charging.

The main components of the radiation environment for a lunar lander spacecraft are:

- Radiation belts or Van Allen belts: the radiation belts consists of electrons and protons, magnetically trapped around the Earth.

- Solar Particle Events: the events of this type occur mainly during the solar maximum period. The events are strongly enhanced flux of protons originated from the Sun; these particles are usually accompanied by flux of heavy ions.

- Galactic Cosmic Rays: consist of heavy ions capable of causing intense ionization passing through the matter. Even if the particles of galactic cosmic rays have very high energy, the flux is low.

- Secondary radiation: this radiation derived by the interaction of the above components with the materials of the spacecraft.

Particulates

Each spacecraft in Earth orbit can be exposed to a flux of micrometeoroids. Any collisions occur at hypervelocity. Meteoroids are generated by comets or asteroids, thus they are particles of natural origin. In addition to these natural particles, there are the space debris, man-made particles.

The collision with micrometeoroids and space debris can cause damage to the spacecraft. The level of damage depends on the density, speed, size and direction of the impacting particles, and obviously on the shielding of the spacecraft.

Contamination

The definition of the contamination environment regards the induced molecular and particulate (liquid or solid) created by the presence of the spacecraft.

Molecular contamination can be generated by the outgassing of the spacecraft surface, unburned propellant vapours, gases of pyrotechnic mechanism and so on.

Particulate contamination can be inherent to materials, for example particles originated by manufacturing or handling, or external to materials like dust during assembly or integration, or human sources (hair or skin flakes).

The effects due to a contamination are related to the degradation of the spacecraft surface and its sub-systems performances.

6.2.1 Moon environment

MPAc and all other payloads on board of the lander are designed for operations only during the lunar day. MPAc must operate in Ultra High Vacuum (UHV) space conditions and within a temperature ranges appropriate for the lunar day. Typical temperature, pressure and humidity conditions are reported in [8]:

Mission phase	Temperature range
Pre-Launch	$0°C$ to $27°C$
Launch	$0°C$ to $27°C$
Cruise	$-60°C$ to $100°C$
Lunar Orbit	$-120°C$ to $100°C$
Surface	$-30°C$ to $80°C$

The thermal environment is colder for objects in shadow and hotter for objects in direct sunlight. These temperatures are typical for the lunar day.

Mission phase	Pressure
Pre-Launch	101.3 kPa
Launch	-6.2 kPa/s
Remaining Mission	$6.7 \cdot 10^{-5}$ kPa

The pre-launch pressure value is the average atmospheric pressure at sea level. The launch value is based on the Atlas V. The value $6.7 \cdot 10^{-5}$ kPa represents the vacuum of the space environment.

Mission phase	Humidity
Pre-Launch	35% to 90%
Remaining Mission	0%

The 0% of humidity represents the vacuum of the space environment.

Lunar dust

Important feature of the lunar environment is the regolith, the lunar surface material. The outer surface layer of the Moon is made of debris blanket continually agitated by the impacts of meteorites. Lunar regolith was found to be similar to terrestrial volcanic ash (Fig. 6.3).

The regolith particles with a size $< 100\mu m$ are called dust. The average grain size is $\sim 70\mu m$, not visible to the human eye; the grain shape is highly variable, from spherical to extremely angular. The regolith has low electrical conductivity; this allows dust grain to hold electrostatic charge. However conductivity can increase with surface temperature [58].

The lunar dust can cause many problems, especially during the manned missions. In fact testimonies of astronauts state that dust reduces visibility and makes breathing difficult. Moreover, another problem regards the spacesuits: the dust adhesion mechanically, due to the shapes of dust grain, and electrically, due to charging of objects by the solar wind, and the consequent abrasive effect reduce its useful lifetime drastically.

Figure 6.3: The nature of the lunar surface is illustrated in this figure: small pebbles collected by a rake near the Apollo 16 landing site. (Courtesy of NASA, AS16-116-18690.)

However, the lunar dust can create problems even in non-manned missions. The electrostatic adhesion of regolith onto solar arrays and optical objects leads to a reduction of solar power generation and a degradation of optical measurements. In addition the dust contributes to increased friction and more rapid wearing of mechanical joints, and to the contamination of optical observation, due to the scattered light from dust.

6.3 Mechanical, electrical and optical features

MPAc is a double pointing actuator, equipped with MoonLIGHT 100 (ML100). ML100 is a CCR, with 100 mm of front face diameter. In order to point MoonLIGHT to the Earth direction, MPAc must be able to perform two continuos rotations. The current design is shown in the Figure 6.4.

In order to analyze better the MPAc design, it is possible to divide ideally the entire structure into three parts.

- **Azimuth block**: the lower part of MPAc represents the interface with

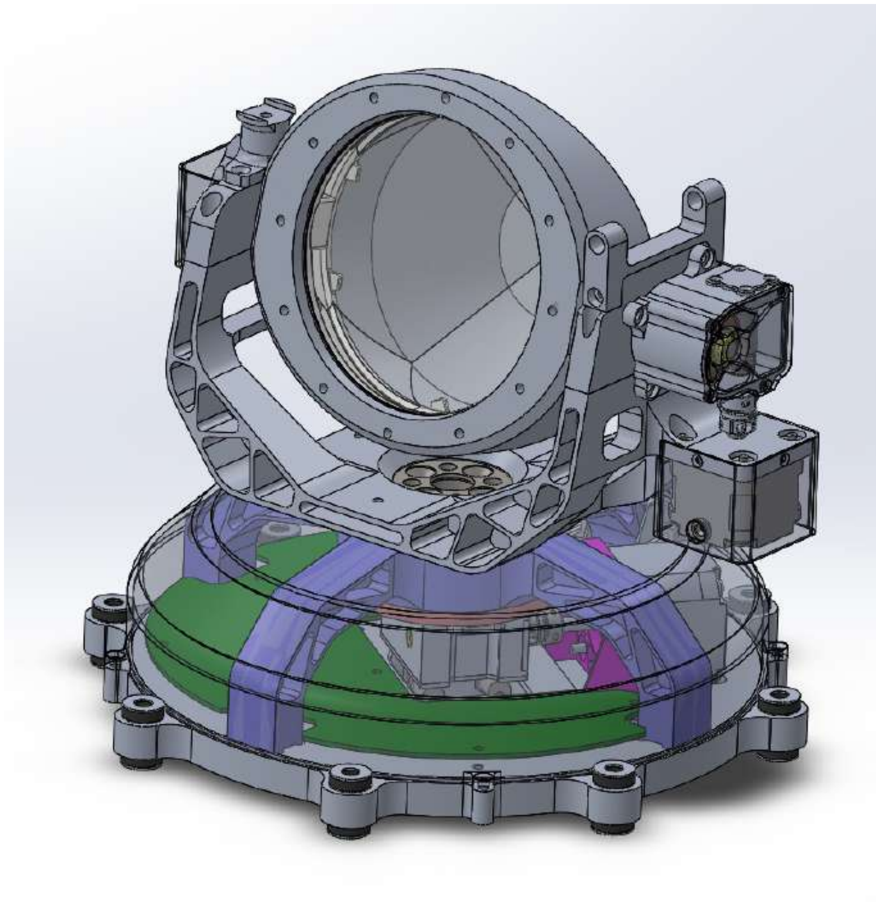

Figure 6.4: The current design of MPAc.

the lander and it is fixed with respect to it. This block contains most of the electronics and the motor responsible of generating the Azimuth movement. The Azimuth rotation is around the normal to the (horizontal) lander deck surface with an ideal range of ±180°; for safety reasons, the real range of movements is limited by two Limit Switches. It holds the rest of the structure.

- **Elevation block**: this block generates the Elevation rotation around an axis parallel to the lander deck. Its ideal range is ±90°; as in the Azimuth block, for safety reasons, the real range of movements is limited by two Limit Switches. The Elevation block contains the motor responsible of generating the Elevation movement and is responsible of holding the last block, the CCR Housing.

- **CCR Housing**: the last block contains MoonLIGHT 100 retroreflector, with its integration structure. It is a completely passive block; its function is to hold and protect the CCR.

In the Table 6.2, dimension, mass and general features are listed. Since the project is still under development, some features may be subject to variations.

Mass	4000 g
Dimensions [h x w x d]	$250x250x250mm^3$
Mechanical interface	4 x M5 screws
Materials (parts)	Aluminum (Al 6082 T6) PCTFE (KEL-F, reflector mounting rings) Suprasil 311 (Uncoated retroreflector, MoonLIGHT100) Steel (AISI 304, reflector front housing) Silver Plated Ni alloy (reflector back housing) CRES Steel (parts for adjustable elevation)
Electronic Interface	Power lower than 20W per 1h poiting attempt Operating Voltage: $28V \pm 4V$ Communication Bus: RS422
Coatings	MIL A8625 Anodization Alodine 1200 (gold color surfaces) Silver coating (interior back housing) AZ93 white inorganic coating (exterior back housing) MLP-300-AZ-Primer (exterior back housing)
Temperature range	From 120 K to 390K or $-153°C$ to $+117°C$ (tested)
Accuracy	Azimuth: $< 2°$; Elevation: $< 2°$
Lifetime	Several decades
Vacuum	UHV to 10^{-11} mbar
Output torque	from about 2 Nm to about 5 Nm
FoV	$> 17°$ semi-aperture cone

Table 6.2: Current features of MPAc.

6.3.1 Optical characterization of MoonLIGHT

In order to verify the thermo-optical features, a SCF-Test of MoonLIGHT was previously performed. As the LARES-2 tests, the SCF-Test can be summarized in a SS ON phase, during which the CCR is heating up, and a SS OFF phase, in which the retroreflector is interrogated by the laser.

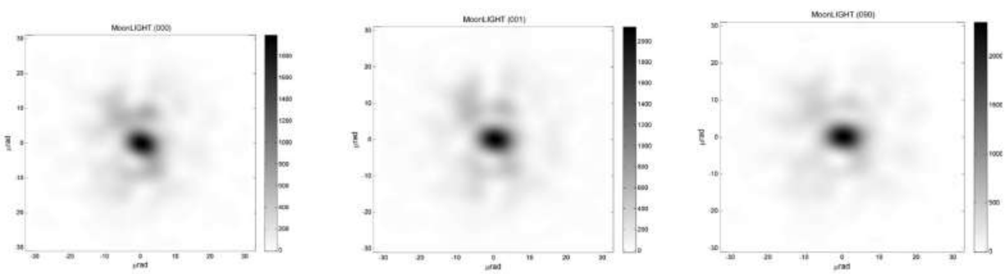

(a) FFDP 000. (b) FFDP 001. (c) FFDP 090

Figure 6.5: FFDP of MoonLIGHT at the beginning of the test, at the end of the SUN ON phase and at the end of the SCF-Test [17].

MoonLIGHT is an uncoated retroreflector, and thus, the components of FFDP was recorded separately. The first FFDP was acquired before starting the SUN ON phase. Then during the heating phase, the CCR face was irradiated by the solar simulator beam for 14 hours, with two incidence angle with respect to the beam, i.e. $0°$ and $30°$. During the SUN OFF phase, there were four sessions of FFDP acquisition: the first two were 1 hour long, during which the acquisition of the pattern was every 2 minutes and 4 minutes respectively, the second two were 120 minutes long, with acquisitions every 10 minutes and 30 minutes respectively.

At the end of these acquisitions, there was several FFDPs: Figures 6.5 shown the FFDP at the beginning of the test (Fig. 6.5(a)), the FFDP at the end of the SUN ON phase (Fig. 6.5(b)) and the final FFDP (Fig. 6.5(c)). The final output was the average OCS at VA related to MoonLIGHT (Fig. 6.6).

It is easy to notice that the pattern at different phases of the test are quite similar; moreover, the intensity approximately returns to initial value without degradation.

At the same time, also the thermal analysis was done with the IR camera. The data shows a very long thermal constant: $\tau_{CCR} = 13.0 \pm 1.2 \cdot 10^3 s$ for

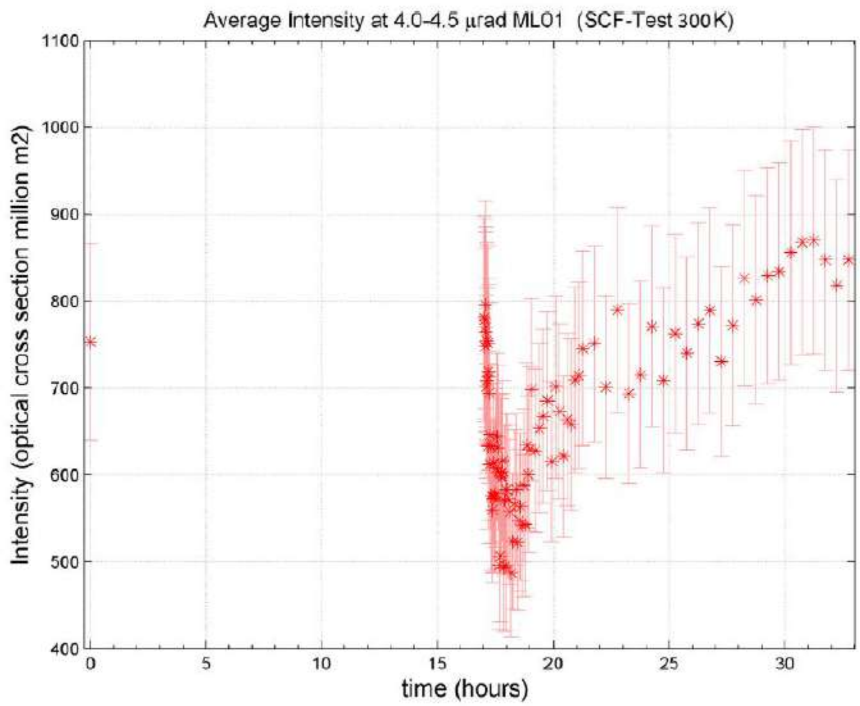

Figure 6.6: Average OCS in function of the time, at range VA of $4.0 \mu rad$ *and* $4.5 \mu rad$ *during the SCF-Test [17].*

the 0° of SS incidence angle and $\tau_{CCR} = 12.1 \pm 1.1 \cdot 10^3 s$ for the 30° of SS incidence angle. These results are expected due to the large dimensions of MoonLIGHT and are helpful to the thermal insulation and to have a good optical performance. These results are consistent with the optical one [17].

6.3.2 Removable Cover

Another important part of MPAc is the protection against the lunar dust, or in other words a removable cover.

To understand the necessity of protecting the retroreflector, it is enough to check the environmental impact in other optical devices that are placed on the lunar surface. In particular, it is shown that after less than a decade, the light return of the retroreflectors of the Apollo arrays showed a clear reduction or, in other words, a degradation of its optical performances (Fig. 6.7).

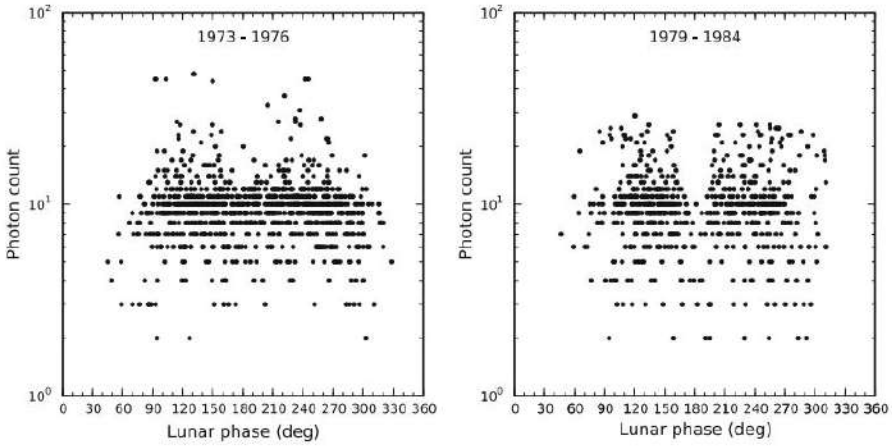

Figure 6.7: Apollo 15 photons counts of two different periods: during the second period there was a drop in the signal rate, more evident around the full Moon phase [46].

In the earliest year of Lunar Laser Ranging data this deficit didn't exist: thus, the degradation is evident over the decades. Indeed, analyses of existent retroreflectors arrays reveals a decrease by a factor of 10 with respect to the first LLR operations. Moreover, Lunokhod arrays shows a higher degradation, probably due to the greater exposure. The reasons of the optical degradation may lie in lunar dust deposition.

In order to avoid the deposition of the dust that is raised during the lunar landing, it was decided to add a removable cover to protect MoonLIGHT.

The cover was added after the design of MPAc: because of this, it must be limited in weight and dimensions, respecting the pre-established space limits within the lander of $250x250x250mm^3$; it must be simple, also in the activation, and it must not cause disturbance if the field of view of the retroreflector.

Downwards models

There are two options for the dust cover: the downwards model and the upwards model. Both will be analyzed, but currently the second model was chosen.

In the first model, the CCR front face should point downwards in its nominal position, before to the aperture (Fig. 6.8). There are binaries used as guide for the plate and the final position not represents disturbance in any sense.

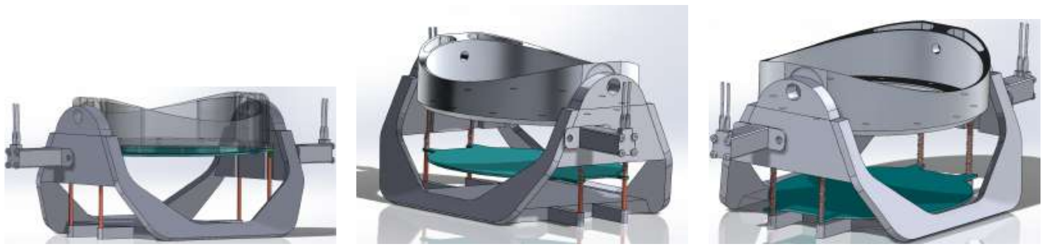

Figure 6.8: The downwards model designed for the dust cover of MPAc.

The activation of this mechanism requests two pin pullers, one of each side. During the activation, the Pin Pullers (details in 6.4.4) retract their pins, that are blocking the plate, so the gravity and the springs push it downwards.

Upwards models

Another options of the cover utilizes a torsion spring and an actuator (Mini Frangibolt, details in 6.4.4).

Figure 6.9: The upwards model designed for the dust cover of MPAc.

This model was chosen to examine in depth, because only one actuators is needed and especially it is not invasive with the MPAc existing structure.

The plate rotates about a joint on a vertical supports of the elevation main frame that contains a torsion spring, whose natural position corresponds to the open configuration. The plate is fixed to the other vertical support by the Frangibolt Actuator screw. The activation of the Frangibolt releases the blocking screw, pushing upwards the plate that spins until it reaches the limit. Once opened, the plate is placed in the opposite side of the Elevation motor (Fig. 6.9) and does not disturb MPAc in its azimuth spin.

Figure 6.10: The upgraded upwards model designed for the dust cover of MPAc.

The final position of the cover could be an obstacle for the Azimuth block rotation; for this reason, the cover was redesigned to better fit the CCR housing and better cover the surface, but above all to solve the problem of space in the final position. The upgraded model is shown in the Figure 6.10, it is easy to notice the less space occupied, both laterally and vertically. The plate is divided into two parts, i.e. a smaller one, about a third of the total plate size, which is place in the hinge side, and a larger one, that should be attached to the Frangibolt during the close position. The two parts are linked by a continuous hinge that allow them to fold on themselves during the aperture.

Both models ensure a good shielding of the CCR front face. Considering the current designs, the upwards opening option better fits the surface of the housing, while the downwards model is more limited by the available space inside the two vertical arms.

6.4 Components

6.4.1 Microcontroller

Microcontrollers could be found in vehicles, robots, office machines, medical devices, mobile radio transceivers, vending machines and home appliances. They are essentially simple miniature personal computers on a single integrated circuit chip: they contain one or more processor cores, a memory and input/output programmable peripherals.

A microcontroller is inside of a system to control a singular function in a device. To do this, it interprets data that receives from its Input/Output (I/O) peripherals using its central processor. The temporary information that the microcontroller receives is stored in its data memory. The processor accesses it and uses instructions stored in its program memory to decipher the incoming data. It then uses its I/O peripherals to communicate and enact the appropriate action.

The microcontroller chosen for our project is SAMV71Q21 by Microchip [33]. It contains all features needed to our system and it has radiation resistant version.

6.4.2 Stepper Motors

In order to move the structure to point the retroreflector, it is necessary to consider the motors. The motors chosen are stepper motors: this typology of motors is one of the simplest to use, but at the same time, is one of the most accurate in repeatability and positioning. Moreover, stepper motors provide a large amount of torque at low speeds. The main reason that led us to choose the stepper motor typology is the necessity of a security in the positioning. In particular, MPAc is not designed to be a closed-loop system, i.e. with a feedback, because this forces to use an Encoder[1], that means higher costs and weight, at the expense of the positioning certainty. Thus, to be sure of the positioning accuracy without a feedback, the idea is to use a motor with a higher than necessary torque. In this way, a stepper motor with a very high torque has a negligible, or however very low, risk of lose steps.

[1]The Encoder is an electro-mechanical device that converts the angular position of its rotating axis into a digital electrical signal.

To obtain the rotation it is necessary to drive the motor with a suitable sequence of activation of the windings of the motor: therefore advancing by successive steps the angular position of equilibrium of its rotating part (rotor). Thus, it is possible to know a priori the position reached by the rotor simply counting the number of pulses sent.

There are stepper motors with several angular resolutions: from the lowest resolution of 90° to the motors with a resolution of 1.8° (200 steps resolution each revolution) or 0.72° (500 steps resolution each revolution).

Each stepper motor has a rotor (moving part) and the stator windings (stationary part).

When the current flows through the stator winding, a magnetic field is produced. The magnetic field implies the rotor rotates by an angle; in other words, the rotor aligns with this field. By supplying different phases in sequence, the rotor can be rotated by a specific amount to reach the desired final position. Stepper motor rotates following a sequence of electrical impulses; at each pulse, the rotor moves by a precise portion of the round angle. This precise movement of the rotor is called "step", from which derives its name.

Class of stepper motors

There are three classes of stepper motors; the difference among these consists in the rotor structure:

- Permanent-Magnet;
- Variable-Reluctance;
- Hybrid.

The first typology of motors consists of a rotor, made of permanent magnets, that generates a magnetic field directed perpendicular to the rotor axis. The stator is formed by the windings that come piloted in sequence to drag the rotor. The concentrating windings on diametrically opposite poles are connected in series to form a two (or more) phase winding on the stator (Fig. 6.11).

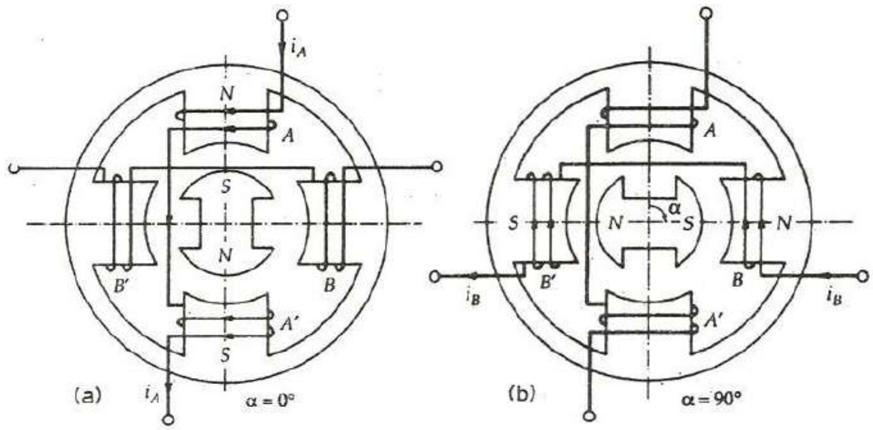

Figure 6.11: Diagram of permanent magnet stepper motor: in the figure (a) the current flows the start to the end of phase A. The south pole of the rotor is attracted by the stator phase A. In the figure (b) the current flows from the start to the end at phase B. The stator pole attracts the rotor pole and the rotor moves by 90° *in the clockwise direction.*

The variable reluctance stepper motors have a rotor of low reluctance material with numerous teeth, fewer than the stator poles, to prevent these from being in exact correspondence with the stator teeth. To understand better the working principle of this stepper motors typology, in the Figure 6.12 there are the phases to make move the rotor. At the beginning, phase A is energized and the rotor is aligned with the magnetic field it produces. When phase B is energized, the rotor rotates to align with the new magnetic field and so on.

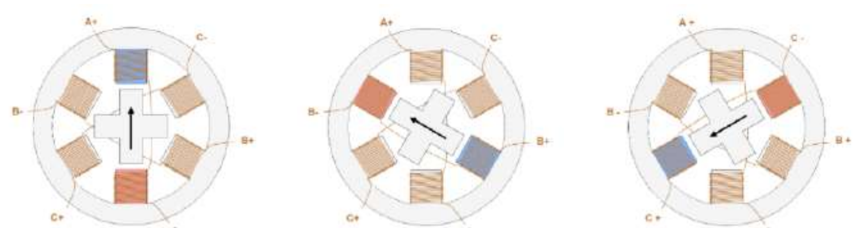

Figure 6.12: Diagram of variable reluctance stepper motor: phase A is energized and the rotor is aligned with the magnetic field it produces. Then, phase B is energized and the rotor is aligned with the magnetic field it produces. In the same way, phase C is energized and the rotor rotates to align to it.

To try to combine the positive aspects of permanent magnet steppers and a variable reluctance the defined versions were born hybrid typology.

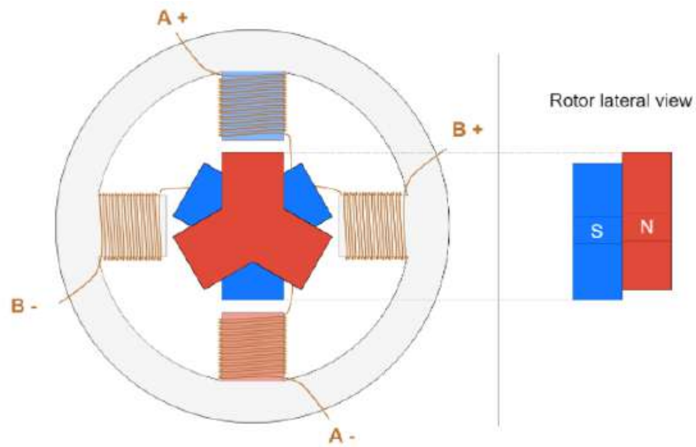

Figure 6.13: Diagram of hybrid stepper motor: if the phase A is energized, the rotor teeth are perfectly aligned with the stator teeth of the phase A. When the phase A is de-energized and the phase B is energized, the rotor will rotate.

The rotor has two caps with alternating teeth, and is magnetized axially. This configuration allows the motor to have the advantages of both the previous versions, specifically high resolution, speed, and torque. The Figure 6.13 shows the simplified version of a hybrid stepper motor. When the phase A is energized, the rotor teeth are perfectly aligned with the stator teeth of the phase A. If the phase A is de-energized and the phase B is energized, the rotor will rotate. One of the main advantages of the hybrid stepper motor is the detent torque produced by the permanent magnet. Indeed if the excitation of the motor is removed the rotor continues to remain locked in the same position as before the removal of the excitation.

Another features of the stepper motors is the arrangement of the stator coil: in fact, to make the rotor move, it is necessary not only to energize the phases of the stator, but also to control the direction of the current, which determines the direction of the magnetic field generated.

In stepper motors, there are two different approaches to control the current direction: unipolar and bipolar stepper motors, based on the ability to send the current in one direction or both directions.

The Figure 6.14(a) shows the 4-wires configuration, defined Bipolar: in this typology of stepper motor, it is necessary to invert the polarity, in order

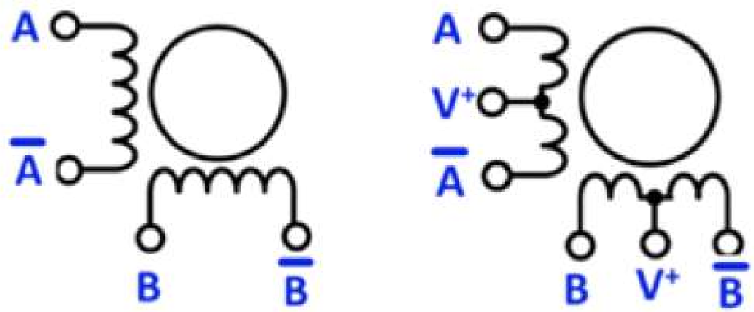

(a) Bipolar (b) Unipolar

Figure 6.14: Bipolar and unipolar version of the stepper motors.

to invert the direction of the magnetic field. In the Figure 6.14(b) it is shown the 6-wires configuration, or Unipolar: the current can be sent only in one direction. Indeed there is the connection point between the winding: to invert the polarity, it is necessary to connect to ground one or the other end of the winding.

In order to drive a stepper motor, there are four different methods:

- Wave drive (Full step);
- 2 phases ON (Full step);
- Half-step;
- Microstep.

Wave drive

In Wave Drive method, only one phase is turned on at a time. If the Phase A is energized, it attracts the north pole of the rotor. Then, if the phase A is turned off and the phase B is energized, the rotor rotates 90° and so on. Each time only one phase is energized, as described in Tab 6.3. Therefore, to complete a revolution it is necessary to do 4 steps (Fig. 6.15). This revolution is equivalent to 1.8° in the case of a motor with an resolution of 200 steps/revolution.

Step	A	B	$\bar{A}$	$\bar{B}$
1	ON	Off	Off	Off
2	Off	ON	Off	Off
3	Off	Off	ON	Off
4	Off	Off	Off	ON
1	ON	Off	Off	Off

Table 6.3: Wave drive scheme.

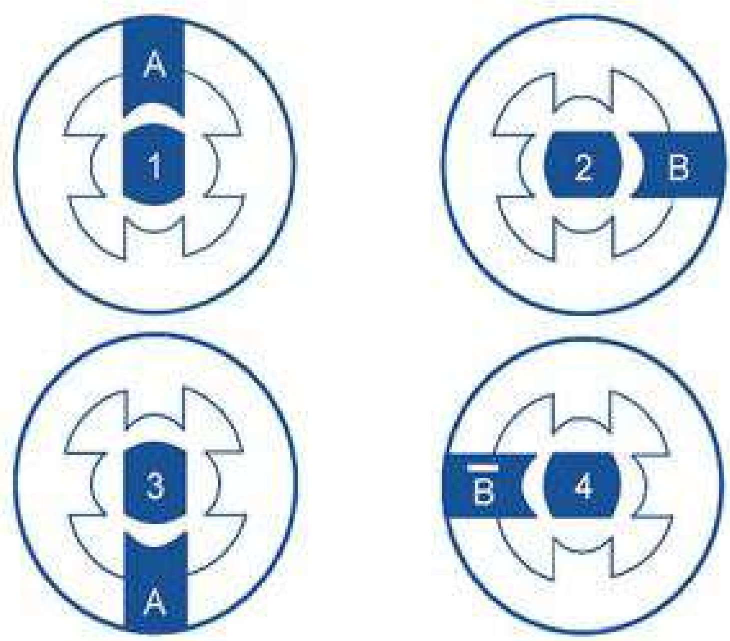

Figure 6.15: Diagram of wave drive method.

2 phases ON

In this method, two phases are always energized (Tab 6.4. If both phases A and B is energized, the rotor will be equally attracted to both and will be aligned to the middle of two phases. The second step occurs when the phases A is turned off and the phase $\bar{A}$ is energized: in this way the rotor rotates 90°, and so on (Fig. 6.16).

Step	A	B	$\bar{A}$	$\bar{B}$
1	ON	ON	Off	Off
2	Off	ON	ON	Off
3	Off	Off	ON	ON
4	ON	Off	Off	ON
1	ON	ON	Off	Off

Table 6.4: 2 phases ON scheme.

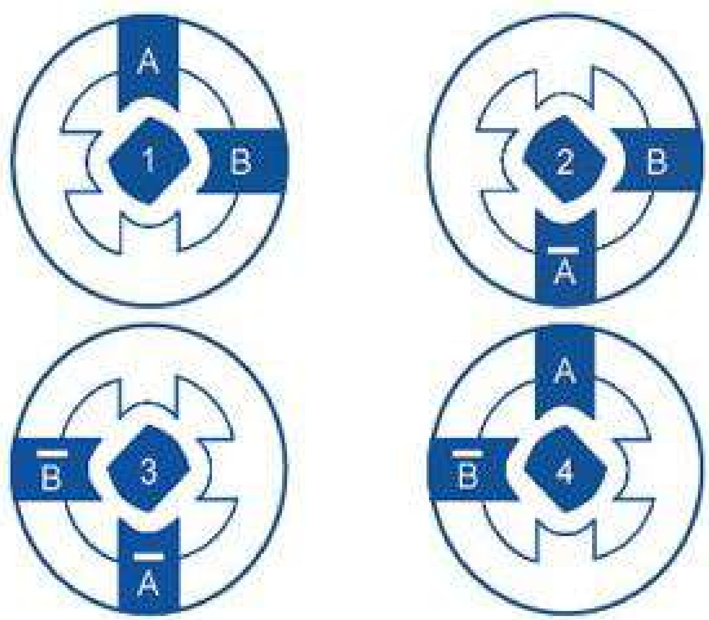

Figure 6.16: Diagram of 2 phases ON method.

Thus, for both methods, to complete a revolution it is necessary to do 4 steps; but the difference is torque. In the first method only one phase is energized and the torque acting on the rotor is one unit. In the second method, there are two units of torque acting on the rotor: at the 12 o' clock position and at the 3 o' clock position; thus, the resultant vector is at 45° with a value of $\sqrt{2}$. While the step is 90° in both methods, the torque is greater of 41% in the two phases ON methods. However, this also leads a double dissipated power, because of activation simultaneous of the two windings. This can cause overheating of the motors.

Half-step

The Half-step methods combines the two previous methods. Indeed, in this method, first one phase is activated individually and then two phases are activated at the same time, as described in Tab. 6.5. In the first step the phase A is energized; the rotor lines up. Then, the phases A remains activated and the phase B is energized; so, the rotor is equally attracted to both and lines up in the middle (Fig. 6.17).Then, this methods continues alternating between one phase on and two phases on. In this way, the rotor rotates 45°, from which the method name "Half-step". In order to complete a revolution, it is necessary to do 8 steps, instead of 4 steps needed for the two previous methods.

Step	A	B	$\bar{A}$	$\bar{B}$
1	ON	Off	Off	Off
2	ON	ON	Off	Off
3	Off	ON	Off	Off
4	Off	ON	ON	Off
5	Off	Off	ON	Off
6	Off	Off	ON	ON
7	Off	Off	Off	ON
8	ON	Off	Off	ON
1	ON	Off	Off	Off

Table 6.5: Half-step scheme.

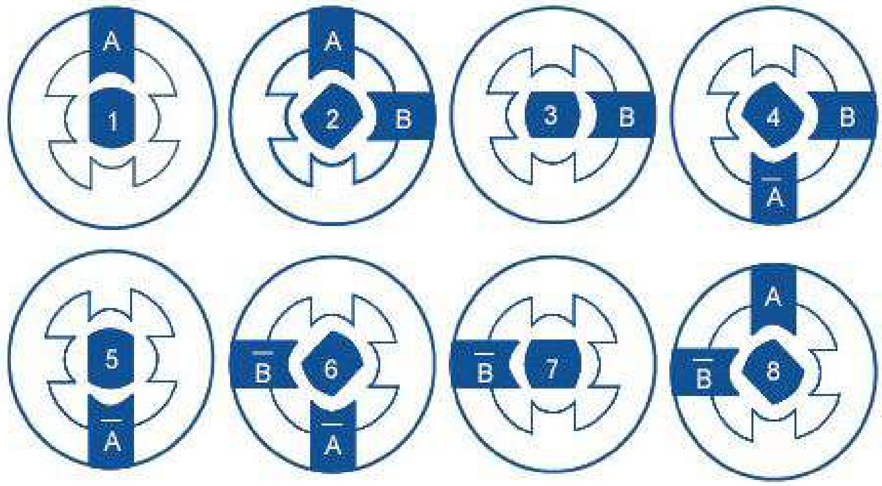

Figure 6.17: Diagram of half-step method.

Microstep

From the half-step method, it's clear to realize a driver with a greater angular resolution. In microstepping, a phase is not fully on or fully off; it is partially on. Sine waves are applied to both phase A and phase B. When the phase A is totally energized, the rotor will line up with phase A. But, if the current to phase A decreases and to phase B increases, the rotor will line up toward phase B. When the phase B is totally energized and phase A is at zero, the rotor will line up with phase B. To have microstepping, the process continues around the other phases.

The advantages offered by microstepping are basically two: increasing the resolution, and therefore the precision of placement, and reducing engine noise by having a smoother rotation speed. However, the torque derived by a magnetic field of one μstep is significantly lower then of one full step.

6.4.3 Limit Switch

In order to be sure the structure is safe, it is necessary to have four Limit Switch, two for Azimuth and two for Elevation.

Limit switches are electro-mechanical devices consisting of an actuator mechanically linked to an electrical switch. In other words, a limit switch is a device operated by a physical force applied to it by an object (mechanical part), and in the same moment can disconnect or connect the conducting path in an electrical circuit, interrupting the current (electronical part). Limit switches are used to detect the presence or absence of an object. These switches were used to define the limit of travel of the stepper motors.

Moreover, MPAc needs a reference point: for this reason, the limit switches are used as reference point in an absolute reference system. In this way it is possible to do the "home-position" procedure (details in Section 6.5), and to start from the zero position in both Azimuth and Elevation.

6.4.4 Actuators for cover

For both models of cover, there is a specific actuator characterized by the Hold Down Release Mechanism (HDRM), found during the cover design phase.

Figure 6.18: Model 1120 NEA Pin Puller [3].

The downwards model requires the Non-Explosive Actuators (NEA) Pin Puller (Fig. 6.18) from EBAD company. It is the thinner model available of this kind and is able to support the estimated loads that would be required. The size of the device is reasonable considering the dimensions of the MPAc and easily attachable. The working principle of the Pin Puller is the following:

Pin Pullers consist of a spring loaded plunger using the fuse wire technology; when sufficient electrical current is passed through the terminals and the fuse wire, the fuse wire heats up and breaks under the applied tension load. This allows releasing the spring preloaded plunger.

The second option of dust cover, the upwards cover, needs another actuator, the TiNi Mini Frangibolt by EBAD company (Fig. 6.19). The principle of this actuator is different from the Pin Puller since it holds a fastener that is released when the device is activated through a current.

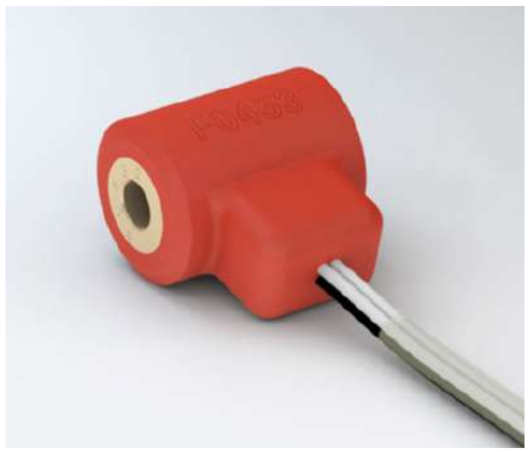

Figure 6.19: TiNi™ Mini Frangibolt® Actuator [4].

6.4.5 Radiation resistant components

Fundamental step of design of a space mission is the selection of components. MPAc encounters the typical environments during the flight to the Moon, described in 6.2.

The most dangerous environment is the energetic particles radiation. Mission orbital specifications with radiation environment models can predict the total absorbed dose of radiation. The parameter to be taken into consideration is the Total Ionizing Dose (TID): the latter increases when electrons and protons create excess charge in the devices. TID is a measure of the energy absorbed by matter; this measurements can be expressed in terms of the absorbed dose. This quantity is measured using either a unit called the *rad* (an acronym for **r**adiation **a**bsorbed **d**ose) or the SI unit which is the *gray* (Gy); $1Gy = 100rads = 1J/kg$.

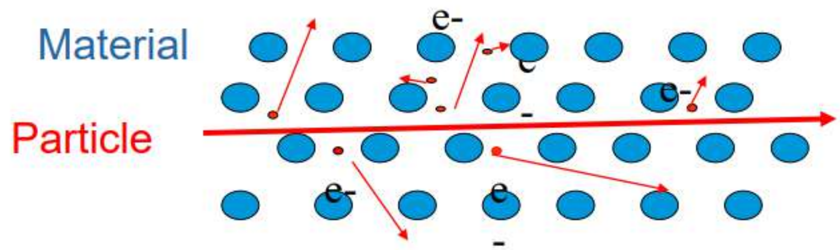

Figure 6.20: The ionization phenomenon.

The degradation of the device becomes obvious after a chronic exposure to numerous radiations events. Device degradation consists of threshold shifts, increased device leakage and power consumption, timing changes, decreased functionality, etc. The particles of the radiation environment traverse the device: their charge present an electrostatic force to the electrons of surrounding material. Ionization produces electron-hole pairs (Fig. 6.20): excited electrons are freed from their bound state, and some of them have sufficient energy to generate further electrons-hole pairs. The electrons produced have high mobility, unlike created holes which have less. Trapped charge could modify the characteristics of the materials like the threshold voltage changes; instead, trapped holes could increase with time, and the consequent on the device could be a threshold shift. This phenomenon occurs mainly in semiconductors, one of the most used material in electronics.

The use of shielding was employed to reduce TID. However, this is not enough: indeed specialized semiconductor manufacturing processes were developed to fabricate radiation resistant integrated circuits.

For space missions, components must be designed with robust and durable electronics able to withstand high-radiation environments for long periods of time without breaking down or malfunctioning. In general there are two types of radiation resistant components: Radiation Tolerant (RT) and Radiation Hardened (RH). The main difference between two is the TID resistance. In order to select the components consistent with our mission, a simple calculation of radiation environment is done. The amount of radiation can be calculated only knowing the exact trajectory of the spacecraft. Actually this information is unknown. To have an idea of this, it is possible to base the radiation count on a typical reference mission direct to the Moon, described in [8].

The entire trajectory to the Moon can be divided in three typical environments: the near-Earth environment, interplanetary environment and lunar environment (Fig. 6.21).

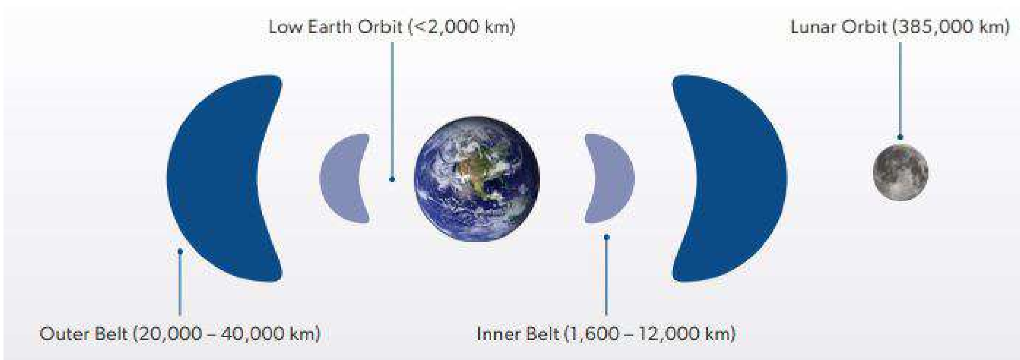

Figure 6.21: A simplified schematization of the typical enviroments encountered by a typical lunar mission [8].

The near-Earth environment is the first environment encountered during the mission: it is defined by the trapped radiation belts. These belts, called Van Allen radiation belts, represent a zone of energetic charged particles, originated by the solar wind and cosmic rays, trapped around the Earth because of the magnetic field due to the Lorentz force. It is possible to distinguish two different belts: the inner belt and the outer belt. While the inner belt contains energetic protons and electrons, the outer belt contains mainly high-energy electrons. The latter is more variable than the inner belt, as it is more easily influenced by solar activity. MPAc may experience 3 to 15 days in the near-Earth environment, during the launch and the cruise phase. TID is expected to be 20 rad/day.

After that, MPAc deals with the interplanetary environment for a period of 14 to 38 days, from the cruise phase onwards. TID is expected to be 1 rad/day.

The lunar environment could be considered as interplanetary environment, because of the lack of the atmosphere and the very weak magnetic field with respect to the Earth. The mission on which will be MPAc is designed to be active only during the lunar day. One lunar day represents the time during which the Moon is in sunlight; it lasts about 14 Earth-days.

To have an estimate of the maximum radiation for MPAc, upper limits of time were used (Tab 6.6).

Near-Earth environment	20 rads/day for 15 days	300 rads
Interplanetary environment	1 rad/day for 38 days	$\sim$ 40 rads
Lunar environment	1 rad/day for 14 days	$\sim$ 15 rads
Total mission		$\sim$ 355 rads

Table 6.6: Estimation of TID for each environment and for entire mission.

The key reason why this estimate was made was the choice of the microcontroller, heart of the electronic board. This choice was fundamental, due to several differences between Radiation Tolerant or Radiation Hardened.

The choice of the microcontroller was between SAMV71Q21RT (Radiation Tolerant) with TID of $30krad$ and SAMRH71 (Radiation Hardened) with a TID$>$ $100krad$. With our information, it was possible to choose the RT microcontroller [32].

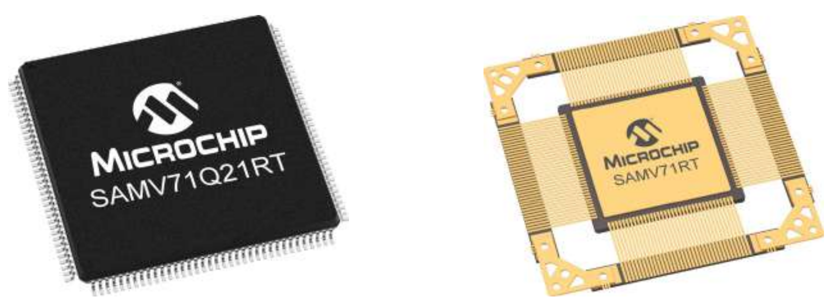

Figure 6.22: The Radiation Tolerant version of the SAMV71Q21 microcontroller.

The SAMV71Q21RT (Fig. 6.22) is the Radiation Tolerant version of the Microchip SAMV71Q21.

As well as for the microcontroller, the motors also need a version resistant to the space environment. Stepper motors chosen are the D35.1 (Fig. 6.23 and the D42.1 by AML (Arun Microelectronics Ltd) [6].

These models of motors are two phase hybrid stepper motors. The resolution is 1.8° which is equivalent to 200 full steps for revolution. The motors

Figure 6.23: Stepper motor by AML, D35.1 model.

are suitable for use in Ultra High Vacuum (UHV), $1 \cdot 10^{-10} mbar$. The standard temperature of operation is extandable up to cryogenic range $-196°C$ to $+175°C$. It is possible to require the radiation resistant version with a TID equal to $1 \cdot 10^6 Gy$ or $10^5 krad$. These stepper motors have also a PT100 temperature sensor, very useful to control the temperature during the lunar operation. Other details about these motors are listed in the Tab 6.7.

	D35.1	D42.1
Mass [g]	190	350
Holding Torque [mNm]	70	180
Detent Torque [mNm]	8	8
Current per Phase [A]	1.0	1.0

Table 6.7: Stepper motors features.

As all components, also the switches have to be radiation resistant. The switches selected are the RUAG Space MSwitch SG: this model is a space grade miniature switch. Further datails in [57].

The cover actuators, already described in 6.4.4, are space-qualified, produced by EBAD company.

Figure 6.24: Space Grade Micro Switch by RUAG space [57].

6.5 Software

In order to allow movement of the structure, it was developed a software, written in C/C++. The movement occurs after a serial commands: thus, the software is able to receive and analyze the command, make the motors move and send a reply.

Before proceeding, it is necessary to give some definition. Motors are named Motor 0 (M0) and Motor 1 (M1) respectively for Azimuth and Elevation. For each motors, there are two limit switches (SW) named Forward, at the end of the clockwise movement, in particular SWM0F and SWM1F for M0 and M1 respectively, and Rewind, at the end of the counterclockwise movement, SWM0R and SWM1R.

The MPAc structure is aimed to an improvement on the pointing of the retroreflector in Azimuth and Elevation. The motion command is related to an absolute reference system, where the zero has been chosen corresponding to the two Rewind limit switches. It is possible to send some types of commands; the common feature is the length of 9 characters.

Motors movements

To drive stepper motors, it is necessary to choose the drive method. As already described in 6.4.2, there are different methods to drive a stepper motors based on the step size. In this software the chosen method is the half-step. In this way, the resolution of the stepper motors is doubled: indeed, the resolution of the stepper motors is 200 steps for revolution; using the half-step method, it is necessary to do 400 steps to do a complete revolution.

In order to make motors move, the following command must be sent:

0000 - 1111

where:

- *0000*: represents the Azimuth coordinates in degrees decimal. Each character can be only number, otherwise there is an error.
- -: can be any character. It has no real function, it is only a sort of separation.
- *1111*: represents the Elevation coordinates in degrees decimal. Each character can be only number, otherwise there is an error.

The software automatically converts the degrees to perform in steps number. For each step, it analyzes the switches. In this way, if the limit switch is touched, the current turns off and the structure stops.

Stop motors: inner command

For each step, the software also analyzes some input serial: indeed, if during the movement the *s* (stands for "Stop") is typed, the motors stop.

Home-position

When starting the software, the motors automatically move to zero position, or *home position*. There is a serial command that allows the structure to position itself again in the home position, without necessarily resetting the board. The command is the following:

homeposit

With this command, both the motors return to the zero position.

"Calibration" commands

By default, the home position makes the motors move in the clockwise direction until the switches SWM0R and SWM1R are activated. For any reason, such as a switch failure, it is possible to change the direction, and consequently, the switch used for the home position thanks to the following command:

cal-swmxN

where

- *cal*: stands for "calibration command";
- -: can be any character. It has no real function, it is only a sort of separation.
- *sw*: stands for "switch";
- *m*: stands for "motor";
- *x*: can be *0* for motor 0 or *1* for motor 1;
- *N*: can be *F* for Forward and *R* for Rewind.

However, with this change the reference system turns upside down and it is necessary to be very careful when sending the movement commands.

Thanks to a calibration procedure, the software is automatically able to convert degrees into steps. In the event that this calibration is wrong, it is possible to change the conversion from degrees to steps, through the following command:

calsd0000

where

- *cal*: stands for "calibration command";
- *s*: stands for "steps";
- *d*: stands for "degrees";

- *0000* is the conversion number, assuming that it is a decimal number; therefore it is not necessary to insert semicolons because the number is automatically divided by thousand. These four characters can be only number, otherwise there is an error.

Formatted reply

At the end of each movement, a formatted reply is printed on the serial monitor. In each bit there is one information fundamental for the status check of MPAc. In the Table 6.8 a detailed list of a typical formatted reply.

Number of bit	Possible content	Description
1	0	NOT performed Home position for Motor 0
	1	Performed Home position for Motor 0
2	0	NOT performed Home position for Motor 1
	1	Performed Home position for Motor 1
3	0	SWM0F NOT activated
	1	SWM0F activated
4	0	SWM0R NOT activated
	1	SWM0R activated
5	0	SWM1F NOT activated
	1	SWM1F activated
6	0	SWM1R NOT activated
	1	SWM1R activated
7	+	Temperature sign for Motor 0
	-	Temperature sign for Motor 0
8-9-10	000	Temperature value for Motor 0
11	+	Temperature sign for Motor 1
	-	Temperature sign for Motor 1
12-13-14	000	Temperature value for Motor 1
15-16-17	000	Performed degrees of Motor 0
18-19-20	000	Performed degrees of Motor 1

Table 6.8: Formatted reply of the software: each bit corresponds to one information about the status of the system.

6.6 Prototypes

In order to test the entire mechanical model, the electronics and software, some prototypes are built.

6.6.1 First prototype

Figure 6.25: First prototype made of plastic.

The first prototype (Fig. 6.25) was entirely made with 3D printed. It is possible to notice the two blocks: the Azimuth block, in which there is the Azimuth motor, and the Elevation block, in which there is the Elevation motor and the basic structure for the retroreflector. The motors used are the d35.1 model of stepper motor by AML (described in 6.4.2). The first prototype allows us to discover many problems related to mechanics, electronics and software.

First of all, this prototype doesn't work well because of the gear ratio. This parameter is used in mechanics to characterize how motion transfers from one gear wheel to another. The gear ratio is the ratio of the number of teeth on the output gear (the one connected to the wheel) to the number of teeth on the input gear (connected to the motor).

$$GearRatio = \frac{OutputGear}{InputGear} \tag{6.1}$$

Based on the value, the gear ratio could be:

- reduction coefficient: if the ratio is greater than 1, the torque will be greater but the speed will be lower;
- multiplication coefficient: if the ratio is lower than 1, the torque will be lower but the speed will be greater;
- impartial coefficient: if the ratio is equal to 1, the torque and the speed will be the same.

The problems noticed thanks to the first prototype is the following: the motors not braked, steps loss, failure to rotate. In the first prototype the gear ratio is 4:1. Nevertheless, the torque is still too low for the structure. Moreover, the gears used are made of plastic, as the entire structure. To improve the performance of this structure, the idea is to made a new prototype increasing the gear ratio and replacing the plastic gears with metallic gears.

6.6.2 Second prototype

Also the second prototype (Fig. 6.26) is made of 3D plastic. Unlike the first prototype, a very simplified base was printed in the second. All the mechanics is changed to increase the gear ratio: indeed, as can been seen from the Figure 6.26, the motor position is different compared to the first prototype. The gear ratio is 50:1; doing this change means increasing the torque but decreasing the speed. However, for MPAc aims, the decrease in speed is not a problem: MPAc doesn't need fast movements. Moreover, the

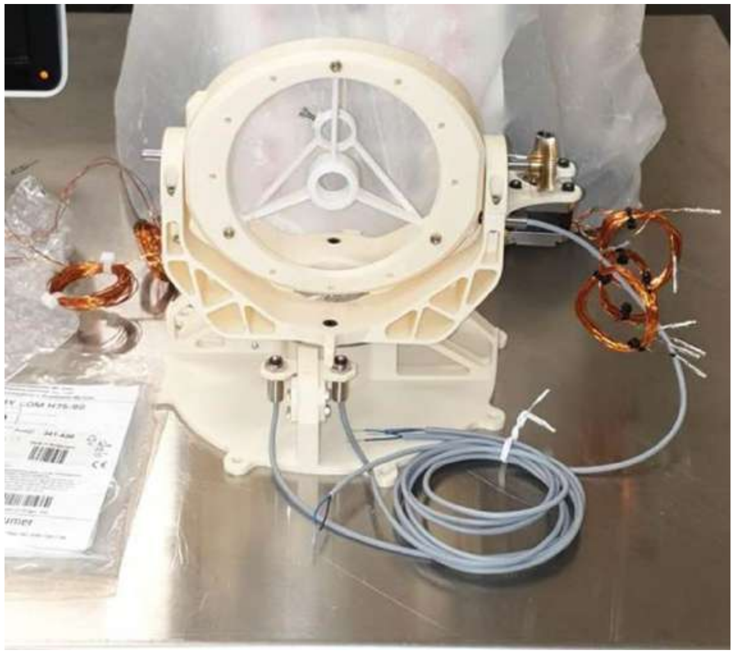

Figure 6.26: Second prototype made of plastic.

gears used are made of metallic material instead of plastic. Using the metallic gears drastically reduces problems such as friction, in addition to being more realistic. These changes were very useful, in fact most of the problems have been solved.

In order to test the positioning accuracy, both of prototype were equipped with an extra structure capable of fixing a small pointer. It is visible in the Figure 6.26: the retroreflector block was used to fix the structure. The positioning accuracy is very low in the first prototype because of all problems already listed. The accuracy is improved with the second prototype, but it is still inaccurate probably due to the low stiffness of the structure material.

In order to test electronics and software, it was necessary to learn to program the microcontroller chosen. The simplest way to use the ATSAMV71Q21 microcontroller was the SAMV71 XPLAINED ULTRA (Fig. 6.27), a commercial electronic board that provides an easy access to the features of the microcontroller.

This board is supported by the Atmel Studio platform, for developing and debugging the microcontroller applications written in C/C++. Together with the board, other commercial parts have been used. For example, L298

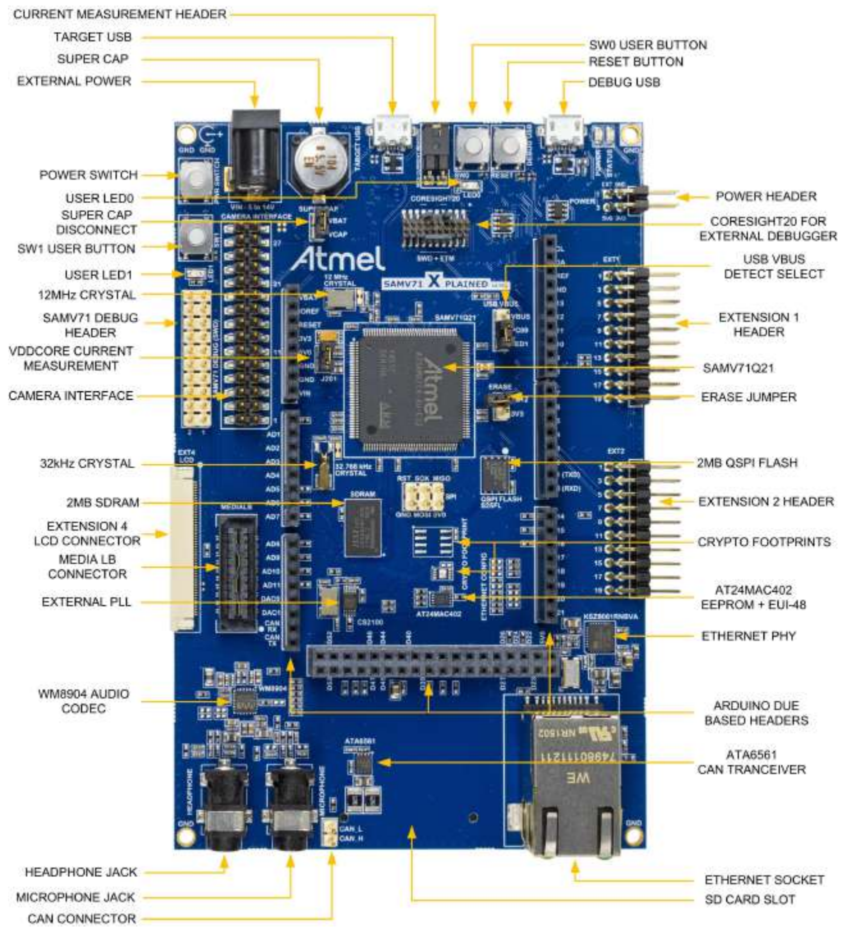

Figure 6.27: The SAMV71 Xplained Ultra board.

Dual H-Bridge is used to drive the stepper motors and MAX31865 Adafruit amplifier is used to read the PT100 sensors of the motors.

6.6.3 Third prototype

The third prototype is entirely made of aluminum. The importance of this prototype is related precisely to its material: all problems related to the stiffness of the structure are solved.

The structure has been very simplified: the base is not important to our aims, therefore it has been streamlined. The Elevation block consists of the moving part moved by the Azimuth motor and the moving part moved

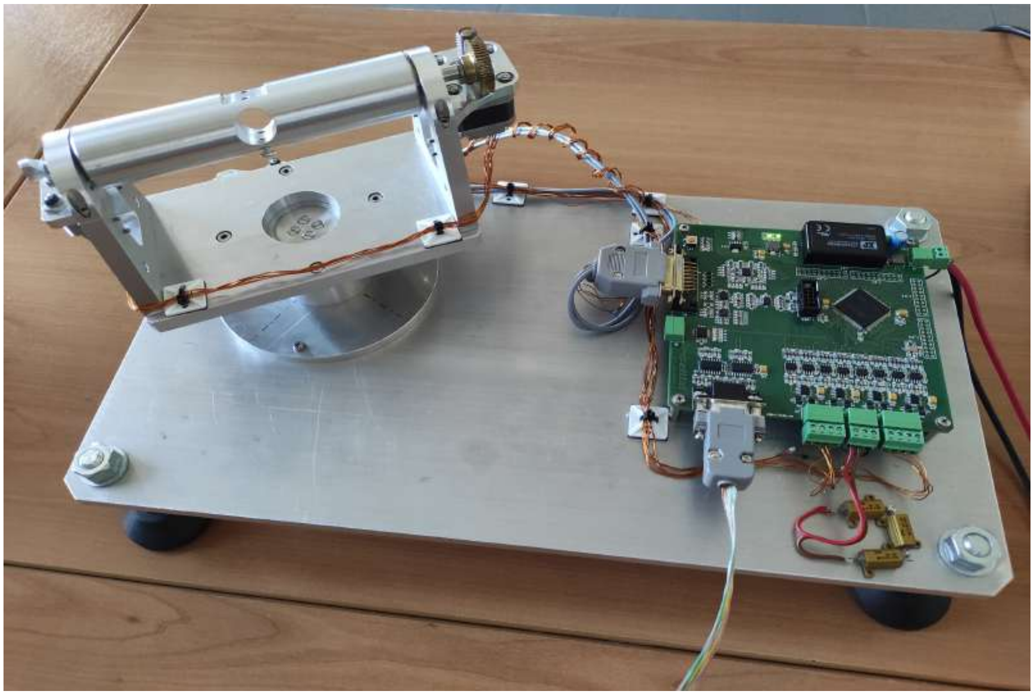

Figure 6.28: The third prototype entirely made of aluminum and the electronic Breadboard.

by Elevation motor. The latter should consists of the retroreflector and its housing; in the prototype this part has been replaced by a support for a small pointer. In this way, it was possible to do some tests on the accuracy in the position.

The first rough tests carry out in the following way: after positioning the pointer in its support, the prototype points towards a certain point of our target, on which it is possible to mark the positions. After the homeposition, movement commands are sent to MPAc prototype. As described in 6.5, these commands are in terms of degrees decimal. Knowing the distance between the pointer and the target, it is possible to calculate the conversion number from steps to degrees. To do this, in the software, the conversion number has to fix to 1: in this way, the movement command is in terms of steps. Sending a certain number of steps, for example 100, it is sufficient to use this formula to know radian of the change of position:

$$\beta = \frac{L}{r} \tag{6.2}$$

where L is the movement and r is the distance between the structure to the target. The degree calculated after the conversion from radian is equivalent to the number of steps sent; in this way it is possible to find the conversion number.

After this procedure, tests need to verify if the structure returns in the initial position after one command and its opposite. These tests have allowed to correct different problems in the software and also detect an issue with the fit between a gears couple, that leaded to an error of a few degrees when changing the direction of the movement, a phenomena known as "backlash". The calculations pointed out the necessity of a reduction of the backlash through a finest design of the gears, or the use of anti-backlash gears that directly remove it after each movement.

6.6.4 Electronic BreadBoard

The third prototype is shown in the Figure 6.28 with a different electronic board, the electronic BreadBoard (BB) (Fig. 6.29). This board has been realized by an Italian external company, Elital. The microcontroller selected for this board is ATSAMV71Q21B, formed by 144 pins, the same for the commercial board. The main resources to be assigned concern the phases for the stepper motor, PT100 sensors, serial communication, limit switches.

The clock signal of the microcontroller is generated by an integrated square wave oscillator with a frequency of 16 MHz. Since the lander provides $28 \pm 4Vdc$, on the BB there is a DCDC converter, an electronic circuit that converts a source of direct current (DC) from one voltage level to another. In this way, it is possible to set to $5V$ the output voltage, needed to stepper motors.

On the breadboard there are 4 digital inputs to be used for the limit switches of the two axes.

Two RS-422 serial interfaces are provided to allow operation in NOMINAL/REDUNDANT.

The internal temperature sensor of the motors will be acquired through Wheatstone bridge interfaces and amplification and filtering section. The overall transfer function can be approximated by the relation:

$$V_0 = 25.314 \cdot 10^{-3} \cdot R_{PT100} \tag{6.3}$$

An external debugging tool is required for the development of the firmware,

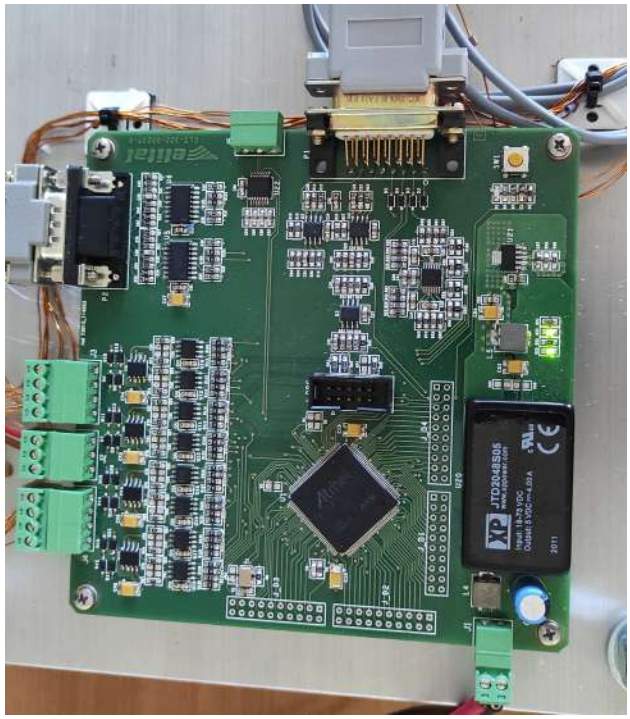

Figure 6.29: The electronic Breadboard .

for debugging and for programming the internal flash of the microcontroller. The connections have been defined considering the Atmel-ICE tool and SAM JTAG 10 pin target connector.

6.6.5 Cover prototype

As for the prototypes of the structure, also for the cover, one prototype was built. The scope of this model and its testing is to check the feasibility of the mechanism and detect inconveniences that may motivate changes to the model, adjustments or directly determine that the model does not comply the requirements.

The operations is recorded from a fixed camera in slow motion, in order to appreciate the details of the mechanism movement.

In order to check the aperture of the cover, without the Frangibolt actuator, the first step is a simple horizontal opening with no extra loads. The aperture is performed correctly from the initial to the desired final position with no apparent blockage or rare behaviour, as it is expected from the digital simulations. The time of aperture is estimated from the images in about 0.43 seconds, from the initial position to its final position. However there is no requirement about time of aperture.

6.7 What next and conclusions

The work on the MPAc project will continue for more than two years, until the launch date fixed in April 2024.

The first phases of the project are described in this chapter: design of mechanical structure, selection of electronic components and motors, development of the software and tests on each one of these through three prototypes. This part of the project will culminate with the Manufacturing Readiness Review (MRR), set for the middle of February 2022.

Once passed the MRR, the manufacturing of the flight payload will start. The plan agreed with ESA and NASA is to build two MPAc models, and in particular an Engineering Model (EM) and a Flight Model (FM). The two models will be very similar, in a such way as to perform representative tests. The mechanical design of EM is equal to FM, except for some electronics components and cables, the absence of external carters and the absence of external structure treatment (white painting).

After that, it will be possible to assemble the EM and to perform subsequent tests on it. If the performed tests will be not passed with success, it will be necessary to change some features in order to solve the problem. Otherwise, the next step will be the assembling of the FM and the performing of tests on it. In this way, the FM can be considered qualified: the delivery of MPAc is set for August 2023.

NASA has selected Intuitive Machines (IM) [1] to build the lunar lander in the framework of the CLPS program. IM will be one of the first commercial lander on the Moon.

The state-of-the-art of the LLR measurements are summarised in the Table 6.9. Tests of General Relativity performed with Apollo and Lunokhod arrays has reached the accuracy of few centimeters.

With MPAc, and in particular with MoonLIGHT on the Moon, test of GR will be improved. Thanks to the data derived from MoonLIGHT, the parameters of fundamental physics shall improve by one order of magnitude, and after several years of measurements, till to two orders of magnitude.

Test of General Relativity	Apollo/Lunokhod few cm accuracy
Parametrized Post-Newtonian (PPN)	$\|\beta - 1\| < 7.2 \cdot 10^{-5}$
Weak Equivalence Principle (WEP)	$\|\Delta a/a\| < 2.4 \cdot 10^{-14}$
Strong Equivalence Principle (SEP)	$\|\eta\| < 3.4 \cdot 10^{-4}$
Time Variation Gravitational Constant	$\|\dot{G}/G\| < 9.5 \cdot 10^{-15} yr^{-1}$
Inverse-Square Law	$\alpha < 3 \cdot 10^{-11}$
Geodetic Precession	$\|K_{GP}\| < 6.4 \cdot 10^{-3}$

Table 6.9: Current limits on precision tests of General Relativity [30].

Test of General Relativity	mm accuracy	0.1 mm accuracy
Parametrized Post-Newtonian (PPN)	10^{-5}	10^{-6}
Weak Equivalence Principle (WEP)	10^{-14}	10^{-15}
Strong Equivalence Principle (SEP)	$3 \cdot 10^{-5}$	$3 \cdot 10^{-6}$
Time Variation of Gravitational Constant	$5 \cdot 10^{-14}$	$5 \cdot 10^{-15}$
Inverse-Square Law	10^{-12}	10^{-13}
Geodetic Precession	$6.5 \cdot 10^{-4}$	$6.5 \cdot 10^{-5}$

Table 6.10: Future improvements achievable of GR tests with MoonLIGHT [30].

The work done so far has been fundamental for the success of the project: the development of the design, tests on efficiency of the motors and structure, tests on software and electronics. The MPAc space mission will be a turning point for the LLR measurements.

Appendices

APPENDIX A

SCF-Test of BreadBoard of LARES-2

The results of the SCF-Test include the evolution of the average intensity, or OCS, at VA equal to $35 \mu rad$ of each CCR of BB at different temperatures. The Figures A.1 and A.2 shows the evolution of the OCS with SS incidence angle of $0°$ at temperatures $T = 280K$,and $T = 320K$.

The Figures A.3 and A.4 show the evolution of the average intensity with SS incidence angle of $31°$ at temperatures $T = 280K$ and $T = 320K$.

Heating and cooling curves for each CCR are shown in Figures A.5 and A.6. During the SS on phase with SS incidence angle of $0°$, CCRs show an increase in temperature of about $4.9K$. During the SS off phase, the temperature decrease is of the same order.

Heating and cooling curves for each CCR are shown in Figures A.5 and A.6. During the SS on phase with SS incidence angle of $0°$, CCRs show an increase in temperature of about $4.9K$. During the SS off phase, the temperature decrease is of the same order.

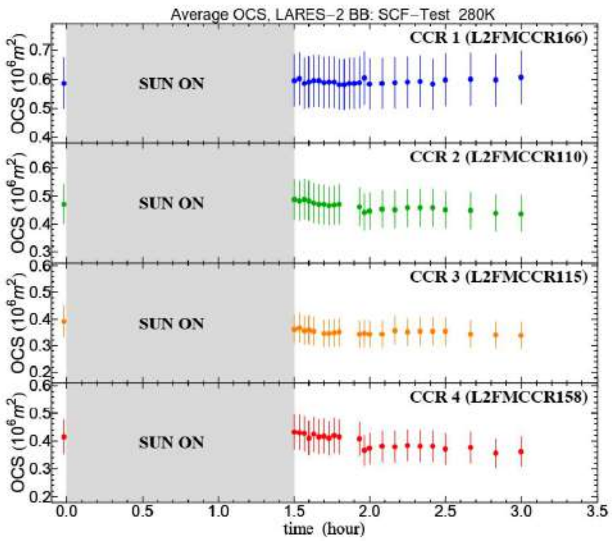

Figure A.1: OCS at $35\mu rad$ of each CCR during the test at $Tc = 280K$ and SS incidence at $0°$. The shades gray area indicates the duration of the SS on, when the BB is rotated toward the SS and no pattern can be acquired.

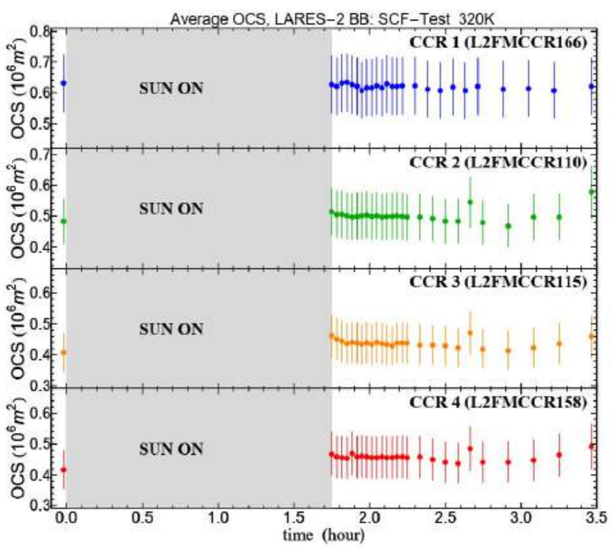

Figure A.2: OCS at $35\mu rad$ of each CCR during the test at $Tc = 320K$ and SS incidence at $0°$. The shades gray area indicates the duration of the SS on, when the BB is rotated toward the SS and no pattern can be acquired.

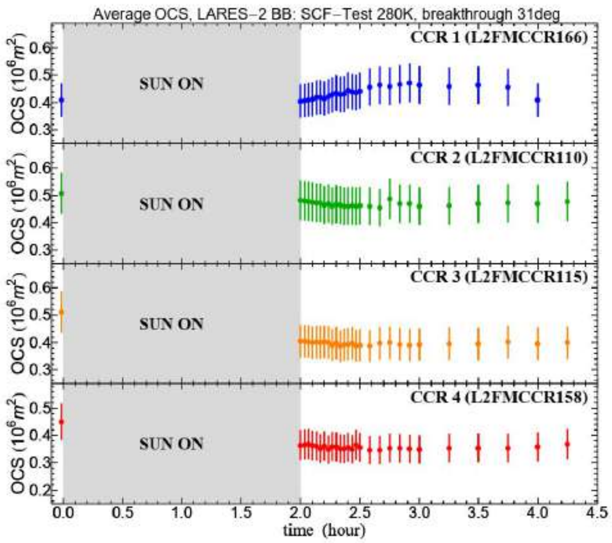

Figure A.3: OCS at $35\mu rad$ of each CCR during the test at $Tc = 280K$ and SS incidence at $31°$. The shades gray area indicates the duration of the SS on, when the BB is rotated toward the SS and no pattern can be acquired.

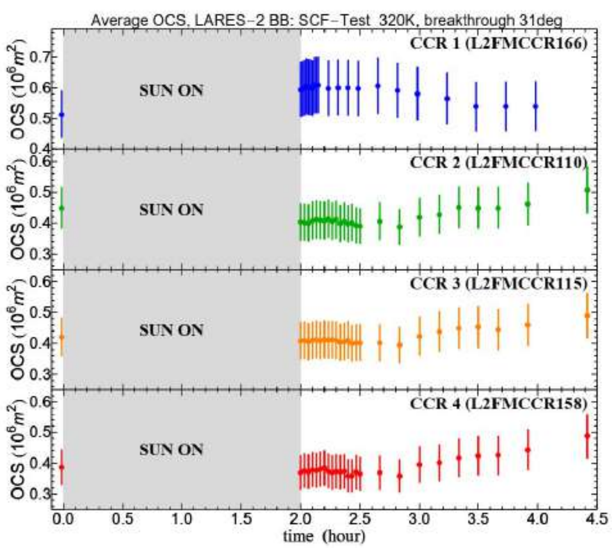

Figure A.4: OCS at $35\mu rad$ of each CCR during the test at $Tc = 320K$ and SS incidence at $31°$. The shades gray area indicates the duration of the SS on, when the BB is rotated toward the SS and no pattern can be acquired.

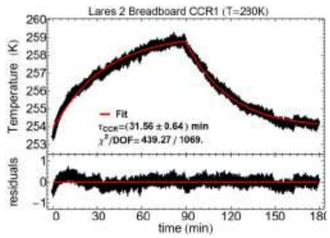

(a)

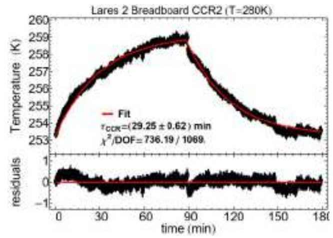

(b)

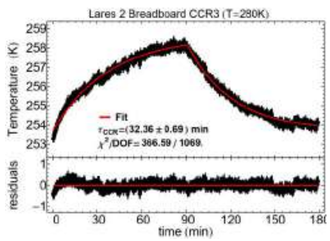

(c)

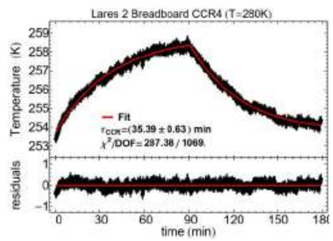

(d)

Figure A.5: Thermal analysis for each CCR, with SS incidence angle of $0°$ *at* $T = 280K$.

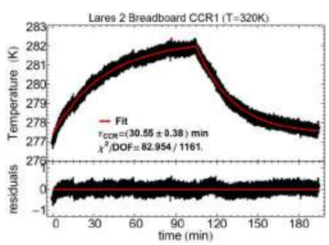

(a)

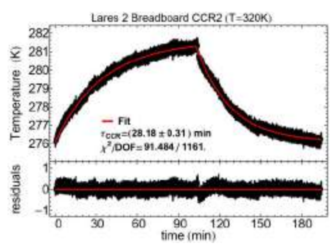

(b)

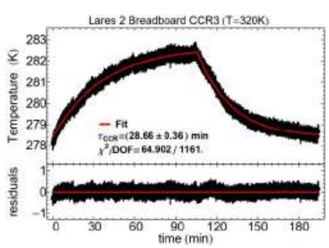

(c)

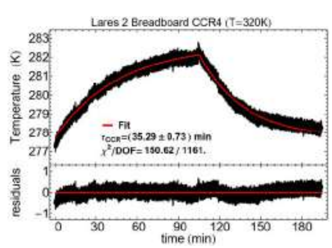

(d)

Figure A.6: Thermal analysis for each CCR, with SS incidence angle of $0°$ *at* $T = 320K$.

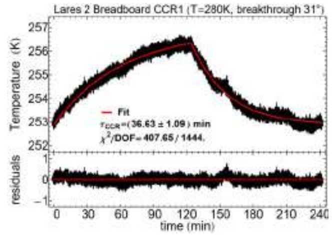

(a)

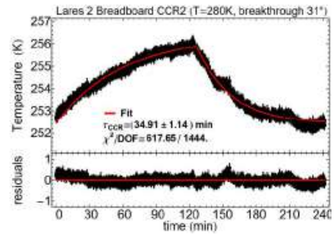

(b)

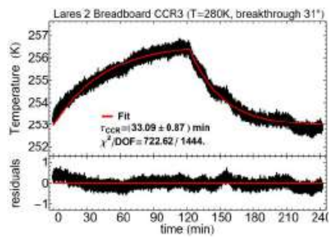

(c)

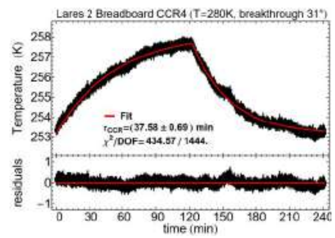

(d)

Figure A.7: Thermal analysis for each CCR, with SS incidence angle of 31° *at* $T = 280K$.

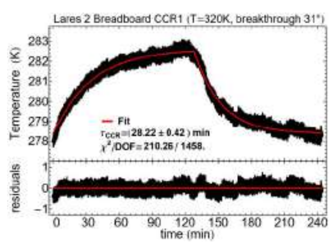

(a)

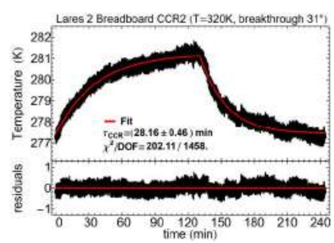

(b)

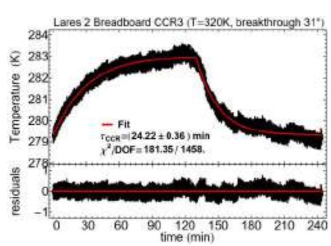

(c)

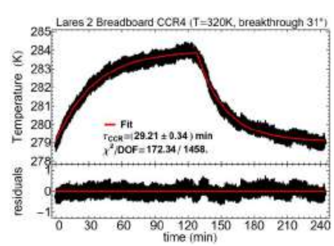

(d)

Figure A.8: Thermal analysis for each CCR, with SS incidence angle of 31° *at* $T = 320K$.

Bibliography

[1] Intuitive machines. `https://www.intuitivemachines.com/`.

[2] E.G. Adelberger, B.R. Heckel, and A.E. Nelson. Tests of the gravitational inverse-square law. *Annual Review of Nuclear and Particle Science*, 53(1):77–121, Dec 2003.

[3] Ensign-Bickford Aerospace and Defense Company (EBAD). Nea model 1120-04 pin puller.

[4] Ensign-Bickford Aerospace and Defense Company (EBAD). Tini™ mini frangibolt® actuator.

[5] S. Agnello, G. Monache, R. Vittori, A. Boni, C. Cantone, E. Ciocci, M. Martini, G. Patrizi, M. Tibuzzi, G. Bianco, D. Currie, N. Intaglietta, L. Salvatori, C. Lops, S. Contessa, L. Porcelli, C. Mondaini, P. Tuscano, and M. Maiello. Advanced laser retroreflectors for astrophysics and space science. 3:218–227, February 2015.

[6] Arun Microelectronics LTD AML. Ultra high vacuum stepper motors.

[7] D. A. Arnold. Optical and infrared transfer function of the Lageos retroreflector array. Unknown, May 1978.

[8] Astrobotic. Peregrine lunar lander, payload user's guide. 2020.

[9] R. A. Bamford, B. Kellett, W. J. Bradford, C. Norberg, A. Thornton, K. J. Gibson, I. A. Crawford, L. Silva, L. Gargaté, and R. Bingham. Minimagnetospheres above the lunar surface and the formation of lunar swirls. *Physical Review Letters*, 109(8), Aug 2012.

[10] James Battat, Christopher Stubbs, and John Chandler. Solar system constraints on the dvali-gabadadze-porrati braneworld theory of gravity. *Physical Review D*, 78, 06 2008.

[11] S. Berardi, S. Dell'Agnello, G. Delle Monache, A. Boni, C. Cantone, M. Garattini, C. Lops, M. Martini, G. Patrizi, M. Tibuzzi, R. Vittori, G. Bianco, S. Zerbini, N. Intaglietta, and E. Ciocci. Galileo, the european gnss program, and lageos. *Il nuovo Cimento*, pages 417–424, 2012.

[12] B. Bertotti, L. Iess, and P. Tortora. A test of general relativity using radio links with the Cassini spacecraft. *nat*, 425(6956):374–376, September 2003.

[13] Liliane Biskupek, Jürgen Müller, and Jean-Marie Torre. Benefit of new high-precision llr data for the determination of relativistic parameters. *Universe*, 7(2), 2021.

[14] Megan Bruck Syal and Peter H. Schultz. Cometary impact effects at the moon: Implications for lunar swirl formation. *Icarus*, 257(Complete):194–206, 2015.

[15] John Chandler, James Battat, Jr Murphy, Daniel Reardon, Robert Reasenberg, and Irwin Shapiro. The planetary ephemeris program: Capability, comparison, and open source availability, 03 2021.

[16] J. Chapront and G. Francou. Lunar Laser Ranging: measurements, analysis, and contribution to the reference systems. *IERS Technical Note*, 34:97–116, January 2006.

[17] Emanuele Ciocci, Manuele Martini, Stefania Contessa, Luca Porcelli, Marco Mastrofini, Douglas Currie, Giovanni Delle Monache, and Simone Dell'Agnello. Performance analysis of next-generation lunar laser retroreflectors. *Advances in Space Research*, 60(6):1300–1306, September 2017.

[18] Ignazio Ciufolini, Richard Matzner, Antonio Paolozzi, Erricos C. Pavlis, Giampiero Sindoni, John Ries, Vahe Gurzadyan, and Rolf Koenig. Satellite laser-ranging as a probe of fundamental physics, 2019.

[19] Ignazio Ciufolini and Richard A. Matzner, editors. *General relativity and John Archibald Wheeler*. 2010.

[20] Ignazio Ciufolini, A. Paolozzi, Erricos Pavlis, R. Koenig, J.C. Ries, Reinhart Neubert, D. Rubincam, D. Arnold, V. Slabinski, Giampiero Sindoni, Claudio Paris, M. Ramiconi, D. Spano, Cristian Vendittozzi, and H. Neumayer. Lares laser relativity satellite. pages 1–, 01 2011.

[21] Ignazio Ciufolini, Antonio Paolozzi, Erricos C. Pavlis, Alessandro Gabrielli, Claudio Paris, and Giampiero Sindoni. Improvement in the measurement of frame-dragging with a future lares 2 mission, 2015.

[22] Ignazio Ciufolini, Antonio Paolozzi, Erricos C. Pavlis, Rolf Koenig, John Ries, Vahe Gurzadyan, Richard Matzner, Roger Penrose, Giampiero Sindoni, Claudio Paris, and et al. A test of general relativity using the lares and lageos satellites and a grace earth gravity model. *The European Physical Journal C*, 76(3), Mar 2016.

[23] Ignazio Ciufolini, Antonio Paolozzi, Erricos C. Pavlis, Giampiero Sindoni, Rolf Koenig, John C. Ries, Richard Matzner, Vahe Gurzadyan, Roger Penrose, David Rubincam, and et al. A new laser-ranged satellite for general relativity and space geodesy: I. an introduction to the lares2 space experiment. *The European Physical Journal Plus*, 132(8), Aug 2017.

[24] Ignazio Ciufolini and Erricos Pavlis. A confirmation of the general relativistic prediction of the lens-thirring effect. *Nature*, 431:958–60, 11 2004.

[25] C. Courde, J. M. Torre, E. Samain, G. Martinot-Lagarde, M. Aimar, D. Albanese, P. Exertier, A. Fienga, H. Mariey, G. Metris, and et al. Lunar laser ranging in infrared at the grasse laser station. *Astronomy & Astrophysics*, 602:A90, Jun 2017.

[26] Douglas Currie, Simone Dell'Agnello, and Giovanni Delle Monache. A lunar laser ranging retroreflector array for the 21st century. *Acta Astronautica*, 68(7):667–680, 2011.

[27] Thibault Damour. Testing the equivalence principle: why and how? *Classical and Quantum Gravity*, 13(11A):A33–A41, Nov 1996.

[28] S. Dell'Agnello, G.O. Delle Monache, D.G. Currie, R. Vittori, C. Cantone, M. Garattini, A. Boni, M. Martini, C. Lops, N. Intaglietta, R. Tauraso, D.A. Arnold, M.R. Pearlman, G. Bianco, S. Zerbini, M. Maiello, S. Berardi, L. Porcelli, C.O. Alley, J.F. McGarry, C. Sciarretta, V. Luceri, and T.W. Zagwodzki. Creation of the new industry-standard space test of laser retroreflectors for the gnss and lageos. *Advances in Space Research*, 47(5):822–842, 2011. Scientific applications of Galileo and other Global Navigation Satellite Systems - II.

[29] J. O. Dickey, P. L. Bender, J. E. Faller, X X Newhall, R. L. Ricklefs, J. G. Ries, P. J. Shelus, C. Veillet, A. L. Whipple, J. R. Wiant, J. G. Williams, and C. F. Yoder. Lunar laser ranging: A continuing legacy of the apollo program. *Science*, 265(5171):482–490, 1994.

[30] Porcelli L. et al. Next generation lunar laser retroreflectors for fundamental physics and lunar science. *Committee on the Biological and Physical Sciences Research in Space 2023-2032 of The National Academies of Sciences of the USA*, 2021.

[31] Ian Garrick-Bethell, James W. Head, and Carle M. Pieters. Spectral properties, magnetic fields, and dust transport at lunar swirls. *Icarus*, 212(2):480–492, 2011.

[32] Microchip Technology Inc. Samv71q21rt, radiation-tolerant 32-bit arm® cortex®-m7 mcu. 2019.

[33] Microchip Technology Inc. Sam e70/s70/v70/v71 family, 32-bit arm cortex-m7 mcus with fpu, audio and graphics interfaces, high-speed usb, ethernet, and advanced analog. 2020.

[34] William M. Kaula. Tidal dissipation in the moon. *Journal of Geophysical Research (1896-1977)*, 68(17):4959–4965, 1963.

[35] J. W. Keller, R. M. Killen, T. J. Stubbs, W. M. Farrell, and J. S. Halekas. Lunar Ion Transport Near Magnetic Anomalies: Possible Implications for Swirl Formation. In *Lunar and Planetary Science Conference*, Lunar and Planetary Science Conference, page 1817, March 2011.

[36] David Lindley. The weight of light, 2005.

[37] Malcolm Longair. Bending space–time: a commentary on dyson, eddington and davidson (1920) ‘a determination of the deflection of light by the sun's gravitational field’. *Philosophical Transactions of the Royal Society A: Mathematical, Physical and Engineering Sciences*, 373(2039):20140287, 2015.

[38] Christian Magnan. Complete calculations of the perihelion precession of mercury and the deflection of light by the sun in general relativity, 2007.

[39] M. Martini, S. Dell'Agnello, D. Currie, G. Delle Monache, R. Vittori, J.F. Chandler, C. Cantone, A. Boni, S. Berardi, G. Patrizi, M. Maiello, M. Garattini, C. Lops, R. March, G. Bellettini, R. Tauraso, N. Intaglietta, M. Tibuzzi, T.W. Murphy, G. Bianco, and E. Ciocci. Moonlight: A usa–italy lunar laser ranging retroreflector array for the 21st century. *Planetary and Space Science*, 74(1):276–282, 2012. Scientific Preparations For Lunar Exploration.

[40] Stephen Merkowitz. Tests of gravity using lunar laser ranging. *Living Reviews in Relativity*, 13, 11 2010.

[41] P. Minott, T. Zagwodzki, T. Varghese, and M. Seldon. Prelaunch optical characterization of the laser geodynamic satellite (lageos 2). NASA Technical Paper 3400, 1993.

[42] Cilence Munghemezulu, Ludwig Combrinck, and Joel O. Botai. A review of the lunar laser ranging technique and contribution of timing systems. *South African Journal of Science*, 112:1 – 9, 04 2016.

[43] T W Murphy. Lunar laser ranging: the millimeter challenge. *Reports on Progress in Physics*, 76(7):076901, Jun 2013.

[44] T. W. Murphy, E. G. Adelberger, J. B. R. Battat, L. N. Carey, C. D. Hoyle, P. LeBlanc, E. L. Michelsen, K. Nordtvedt, A. E. Orin, J. D. Strasburg, and et al. The apache point observatory lunar laser-ranging operation: Instrument description and first detections. *Publications of the Astronomical Society of the Pacific*, 120(863):20–37, Jan 2008.

[45] T W Murphy, E G Adelberger, J B R Battat, C D Hoyle, N H Johnson, R J McMillan, C W Stubbs, and H E Swanson. APOLLO: millimeter lunar laser ranging. 29(18):184005, aug 2012.

[46] T.W. Murphy, E.G. Adelberger, J.B.R. Battat, C.D. Hoyle, R.J. McMillan, E.L. Michelsen, R.L. Samad, C.W. Stubbs, and H.E. Swanson. Long-term degradation of optical devices on the moon. *Icarus*, 208(1):31–35, Jul 2010.

[47] T.W. Murphy Jr., E.G. Adelberger, J.B.R. Battat, C.D. Hoyle, N.H. Johnson, R.J. McMillan, E.L. Michelsen, C.W. Stubbs, and H.E. Swanson. Laser ranging to the lost lunokhod 1 reflector. *Icarus*, 211(2):1103–1108, Feb 2011.

[48] J. Müller, M. Soffel, and S.A. Klioner. Geodesy and relativity. *Journal of Geodesy*, 82:133–145, 2008.

[49] Jürgen Müller, James Williams, and Slava Turyshev. Lunar laser ranging contributions to relativity and geodesy. 349, 10 2005.

[50] Dmitry Pavlov. Role of lunar laser ranging in realization of terrestrial, lunar, and ephemeris reference frames. *Journal of Geodesy*, 94(1), Dec 2019.

[51] Luca Porcelli, Mattia Tibuzzi, Chiara Mondaini, Lorenzo Salvatori, Marco Muccino, Matteo Petrassi, Luca Ioppi, Simone Dell'Agnello, Orlando Luongo, Giovanni Delle Monache, Giuseppe Bianco, Roberto Vittori, and R. Mugnuolo. Optical-performance testing of the laser retroreflector for insight. *Space Science Reviews*, 215, 12 2018.

[52] D. Roberts and M. Zecchino. 4d technology. measuring a corner cube with the accufiz. the accufiz with 4sight software makes it easy to fully characterize the errors in corner cubes. 1 2013.

[53] Samain, E., Mangin, J. F., Veillet, C., Torre, J. M., Fridelance, P., Chabaudie, J. E., Féraudy, D., Glentzlin, M., Pham Van, J., Furia, M., Journet, A., and Vigouroux, G. Millimetric lunar laser ranging at oca (observatoire de la côte d'azur). *Astron. Astrophys. Suppl. Ser.*, 130(2):235–244, 1998.

[54] Shapiro, Reasenberg, Chandler, and Babcock. Measurement of the de sitter precession of the moon: A relativistic three-body effect. *Physical review letters*, 61 23:2643–2646, 1988.

[55] R. Smith and B. J. Anderson. Natural orbital environment guidelines for use in aerospace vehicle development. 1994.

[56] J. Sorensen and D. Rodgers. Lunar lander environmental specification, 2011.

[57] RUAG Space. Ruag space mswitch sg, space grade micro switch. January 2019.

[58] T. Stubbs, R. Vondrak, and W. Farrell. Impact of dust on lunar exploration. 2007.

[59] Slava G. Turyshev, James G. Williams, William M. Folkner, Gary M. Gutt, Richard T. Baran, Randall C. Hein, Ruwan P. Somawardhana, John A. Lipa, and Suwen Wang. Corner-cube retro-reflector instrument for advanced lunar laser ranging. *Experimental Astronomy*, 36(1-2):105–135, Dec 2012.

[60] Vishnu Viswanathan, Erwan Mazarico, Stephen Merkowitz, James G. Williams, Slava G. Turyshev, Douglas G. Currie, Anton I. Ermakov, Nicolas Rambaux, Agnès Fienga, Clément Courde, Julien Chabé, Jean-Marie Torre, Adrien Bourgoin, Ulrich Schreiber, Thomas M. Eubanks, Chensheng Wu, Daniele Dequal, Simone Dell'Agnello, Liliane Biskupek, Jürgen Müller, and Sergei Kopeikin. Extending science from lunar laser ranging, 2020.

[61] J. G. Williams, X. X. Newhall, C. F. Yoder, and J. O. Dickey. Lunar Free Libration. In *Lunar and Planetary Science Conference*, volume 27 of *Lunar and Planetary Science Conference*, page 1439, March 1996.

[62] James Williams, Dale Boggs, Charles Yoder, James Ratcliff, and J. Dickey. Lunar rotational dissipation in solid body and molten core. *Journal of Geophysical Research*, 106:27933–27968, 11 2001.

[63] James G. Williams, Dale H. Boggs, Slava G. Turyshev, and J. Todd Ratcliff. Lunar laser ranging science. *In proceedings of "14th International Laser Ranging Workshop", June 7-11, 2004, San Fernando, Spain, eds. J. Garate, J. M. Davila, C. Noll, and M. Pearlman, 155-161 (2005).*

[64] James G. Williams, Slava G. Turyshev, and Dale H. Boggs. Progress in lunar laser ranging tests of relativistic gravity. *Phys. Rev. Lett.*, 93:261101, Dec 2004.

[65] James G Williams, Slava G Turyshev, and Dale H Boggs. Lunar laser ranging tests of the equivalence principle. *Classical and Quantum Gravity*, 29(18):184004, Aug 2012.

[66] Maria T. Zuber, David E. Smith, Michael M. Watkins, Sami W. Asmar, Alexander S. Konopliv, Frank G. Lemoine, H. Jay Melosh, Gregory A. Neumann, Roger J. Phillips, Sean C. Solomon, Mark A. Wieczorek, James G. Williams, Sander J. Goossens, Gerhard Kruizinga, Erwan Mazarico, Ryan S. Park, and Dah-Ning Yuan. Gravity field of the moon from the gravity recovery and interior laboratory (grail) mission. *Science*, 339(6120):668–671, 2013.